

The SHMS 11GeV/c Spectrometer in Hall C at Jefferson Lab

S. Ali^a, G.R. Ambrose^b, A. Asaturyan^c, P. Brindza^d, R. Carlini¹, M. Carmignotto^a, A. Dittmann^e, D. Dutta^e, R. Ent^d, H. Fenker^{d,*}, M. Fowler^d, N. Hlavin^a, T. Horn^{a,d}, G.M. Huber^{b,1}, Y. Illieva^f, S.J.D. Kay^b, V. Kumar^b, S. Lassiter^d, W.B. Li^b, A. Mkrtchyan^a, H. Mkrtchyan^c, P. Nadel-Turonski^d, I. Pegg^a, A. Ramos^h, J. Reinhold^h, I. Sapkota^a, B. Sawatzky^d, V. Tadevosyan^c, R.L. Trotta^a, S. Zhamkochyan^c, S. A. Wood^d

^aThe Catholic University of America, Washington, DC 20064, USA

^bUniversity of Regina, Regina, Saskatchewan S4S 0A2, Canada

^cA. I. Alikhanyan National Science Laboratory, Yerevan 0036, Armenia

^dThomas Jefferson National Accelerator Facility, Newport News, Virginia 23606, USA

^eMississippi State University, Mississippi State, Mississippi 39762, USA

^fUniversity of South Carolina, Columbia, South Carolina 29208, USA

^gUniversity of Illinois, Urbana-Champaign, Illinois, USA

^hFlorida International University, University Park, Florida 33199, USA

Abstract

The *Super High Momentum Spectrometer* (SHMS) has been built for Hall C at the Thomas Jefferson National Accelerator Facility (Jefferson Laboratory). With a momentum capability reaching 11 GeV/c, the SHMS provides measurements of secondary charged particles produced in electron scattering experiments using the maximum available beam energy from the upgraded Jefferson Lab accelerator. The SHMS is an ion-optics magnetic spectrometer comprised of a series of new superconducting magnets to transport events on an array of triggering, tracking, and particle-identification detectors that measure momentum, energy, angle and position in order to allow kinematic reconstruction of the events back to their origin at the scattering target. The detector system is protected from background radiation by a sophisticated shielding enclosure. The entire spectrometer is mounted on a rotating support structure which allows measurements to be taken with a large acceptance over laboratory scattering angles from 5.5° to 40°, thus allowing a wide range of low cross-section experiments to be conducted. These will complement and extend the previous Hall C research program to higher energies.

Keywords: Magnetic spectrometer, Electron scattering, Tracking detectors, Particle identification, Electron calorimetry, Radiation shielding.

1. Introduction

Introduction section. Author Organizer: D. Gaskell

1.1. Jefferson Lab Overview

The Continuous Electron Beam Accelerator Facility at Thomas Jefferson National Accelerator Facility (Jefferson Lab) provides high energy electron beams for fundamental nuclear physics experiments. Originally planned for maximum electron beam energies of 4 GeV, the accelerator operated at energies of up to 6 GeV starting in 2000. An upgrade of the facility was recently

completed in 2017, enabling beam delivery at a maximum energy of 12 GeV to the new experimental Hall D, and 11 GeV to the existing Halls, A, B, and C.

The electron beam at Jefferson Lab operates at high duty cycle, with beam repetition rates of 249.5 or 499 MHz delivered to the experimental halls. High beam polarization (> 80%) is also routinely available.

In the 6 GeV era, Halls A, B, and C executed a large program of experiments focusing primarily on elucidating the quark-gluon structure of nucleons and nuclei. Experimental Hall B made use of a large acceptance spectrometer capable of detecting many-body final states over a large region of kinematic phase space in one setting. Halls A and C made use of magnetic focusing spectrometers. In Hall A, the two High Resolution Spectrometers (HRS) emphasized excellent mo-

*Corresponding author

¹<http://orcid.org/0000-0002-5658-1065>

27 momentum resolution. In Hall C, the Short Orbit Spec-
 28 trometer (SOS) facilitated the detection of short-lived fi-
 29 nal states (pions and kaons) at modest momentum while
 30 the High Momentum Spectrometer was capable of detect-
 31 ing particles up the maximum beam energy at Jef-
 32 ferson Lab.

33 As part of the 12 GeV Upgrade at Jefferson Lab, a
 34 new experimental hall, Hall D, was built to search for
 35 gluonic excitations in the meson spectrum using a pho-
 36 ton beam produced via coherent Bremsstrahlung. The
 37 GlueX experiment in Hall D began commissioning in
 38 2014 and has taken production-quality data since 2016.

39 The existing Halls A, B, and C were also upgraded
 40 as part of the 12 GeV Upgrade. The Hall A beam-
 41 line and beam polarimeters were upgraded to accom-
 42 modate operation at 11 GeV. Hall A has made use of
 43 the existing HRS spectrometers in its early 12 GeV era
 44 experiments (which began initial data-taking in 2014)
 45 and plans to install specialized, dedicated equipment
 46 for future measurements. Experimental Hall B replaced
 47 its large acceptance CLAS spectrometer with the new
 48 CLAS-12 spectrometer. This new spectrometer retains
 49 the key features of large acceptance and robust parti-
 50 cle identification over a large momentum range but with
 51 more emphasis on particle detection in the forward di-
 52 rection, required due to the higher beam energies. Fi-
 53 nally, Hall C replaced its Short Orbit Spectrometer with
 54 the new Super-High Momentum Spectrometer (SHMS).
 55 This new spectrometer was designed guided by experi-
 56 ence from the 6 GeV program, with the goal of serving
 57 as an optimal partner to the HMS for coincidence exper-
 58 iments.

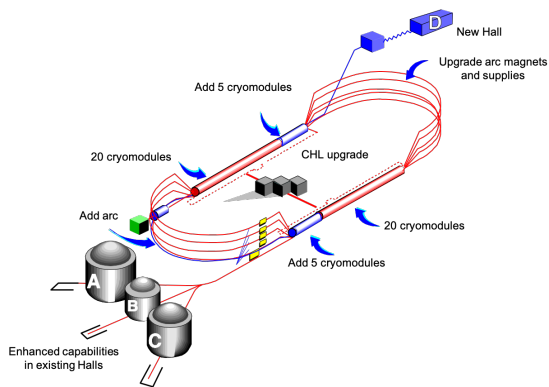


Figure 1: Schematic of hall and accelerator improvements as part of Jefferson Lab 12 GeV Upgrade.

59 1.2. Hall C Experimental Program at 6 GeV

60 The HMS and SOS spectrometers in Hall C enabled
 61 the execution of a diverse program of experiments.

62 The well-understood acceptance of both spectrometers,
 63 in tandem with excellent kinematic reproducibility al-
 64 lowed the extraction of precise cross sections. A partic-
 65 ular strength was the control of point-to-point systemat-
 66 ic uncertainties, which allowed high precision Rosen-
 67 bluth, or L-T, separations. Examples of inclusive cross
 68 section measurements, using primarily the HMS, are
 69 shown in Figs. 2 and 3.

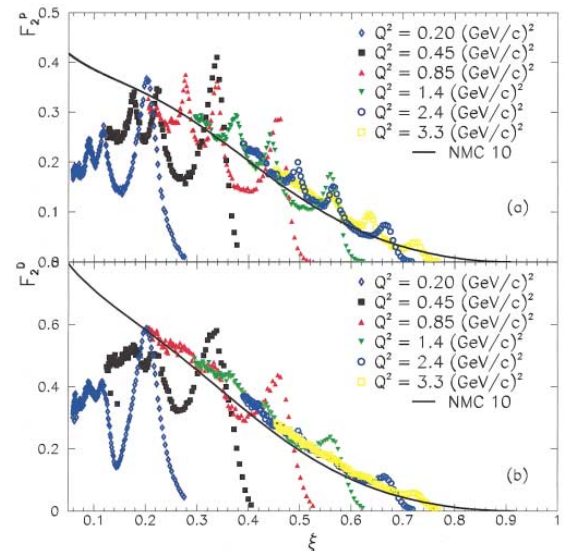


Figure 2: Inclusive F_2 structure functions measured in the resonance region compared to a DIS fit. When plotted vs. the Nachtmann variable ξ , the DIS fit agrees, on average, with the resonance region data, demonstrating quark-hadron duality [4].

70 In addition, the small minimum angle (10.5 degrees)
 71 accessible with the HMS allowed the execution of pion
 72 electroproduction experiments, where, in many cases,
 73 the pion is emitted in the forward direction. This al-
 74 lowed the successful execution of a program of mea-
 75 surements of the pion form factor [71, 72], which also
 76 incorporates precise L-T separations, as well mea-
 77 surements of charged pion production in Semi-inclusive
 78 Deep Inelastic Scattering [73] (see Figs. 4 and 5).

79 The high momentum reach of the HMS (up to the
 80 available beam energy of 6 GeV) enabled measurements
 81 of the $A(e, e'p)$ process to large Q^2 [74, 75] to look for
 82 signs of Color Transparency as well measurements of
 83 inclusive electron scattering at $x > 1$ to access con-
 84 tributions of “Superfast” Quarks to inelastic structure
 85 functions [76] and measure the relative contributions of
 86 Short Range Correlations (SRCs) in the nuclear wave
 87 function [77].

88 The experiments noted above are just a sample of the

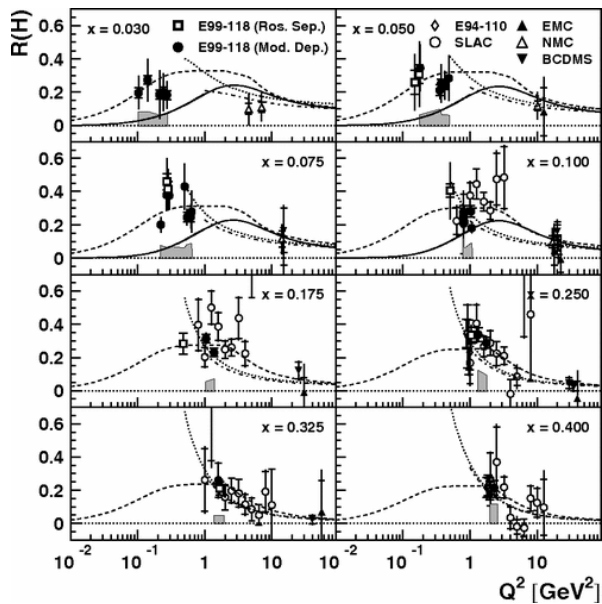


Figure 3: Measurement of $R = \frac{\sigma_L}{\sigma_T}$ at low Q^2 . The extraction of R requires precise L-T separations with excellent control of point-to-point systematic uncertainties. Figure from [70].

89 ≈ 30 “standard equipment” experiments that were executed in the 6 GeV era in Hall C. Other experiments include measurements of exclusive kaon production, resonance (Δ , S_{11}) production, color transparency via pion electroproduction, and numerous inclusive electron scattering measurements using hydrogen and deuterium, as well as heavier nuclear targets. In some cases, the HMS was paired with dedicated equipment for special measurements. Examples of this include measurement of the ratio of elastic proton form factors (G_E/G_M) to large Q^2 , as well as measurements using a dynamically polarized NH_3 .

101 1.3. Hall C 12 GeV Program

102 The new, Super-High Momentum Spectrometer was designed to build on the experimental capabilities exploited during the Hall C program at higher energies. Notably, this includes:

- 106 1. Excellent kinematic control reproducibility
- 107 2. Thorough understanding of spectrometer acceptance
- 108 3. Small angle capability (down to 5.5 degrees) for detection of forward mesons
- 109 4. Central momentum up to (nearly) the maximum beam energy accessible in Hall C
- 110 5. In-plane and out-of-plane acceptance well matched to the existing HMS to facilitate experiments detecting two particle in coincidence

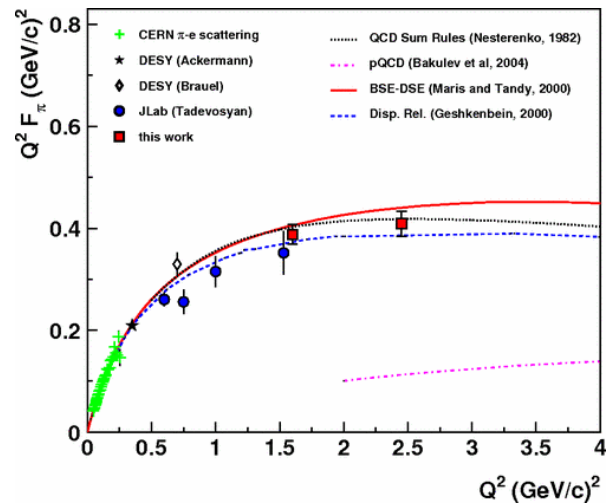


Figure 4: Measurements of the charged pion form factor in Hall C (6 GeV era). Extraction of the pion form factor requires a precise L-T separation, as well as detection of the charged pion at small forward angles. Figure from [72].

116 Several “commissioning” experiments were chosen for the first year of 12 GeV running in Hall C to exercise the above requirements as much as possible. These experiments ran in 2018 and will be discussed briefly below.

121 The first such experiment was a measurement of inclusive electron scattering cross sections from hydrogen and deuterium [56]. Such a cross section experiment is an excellent testing ground for understanding of the spectrometer acceptance, while not pushing the SHMS performance in other areas. Some settings for this experiment were chosen to allow simultaneous measurement with the well-understood HMS to provide a cross section. In addition, some time was devoted to the measurement of inclusive cross section ratios for nuclear targets relative to deuterium [57]. These ratios are well-measured for certain nuclei and serve as another straightforward verification of the spectrometer acceptance due to the need to compare yields from extended (10 cm long) targets to shorter, solid targets (few mm).

136 An extension of the 6 GeV color transparency experiments to larger Q^2 [59] served as an excellent first experiment with which to exercise the SHMS in coincidence mode. In this $A(e, e'p)$ experiment, there are few random coincidences so isolating the coincidence reaction is straightforward. This experiment, as well as a measurement of deuteron electro-disintegration [58], also tested the high momentum capabilities of the SHMS. The SHMS was used at momenta larger than 8.5 GeV/c for these experiments. Although the max-

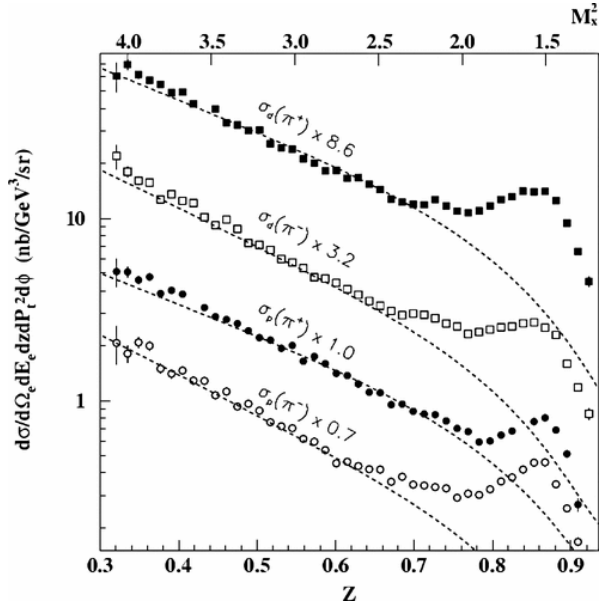


Figure 5: Cross sections for semi-inclusive π^+ and π^- production from hydrogen and deuterium. The cross sections are compared to a parameterization that uses fragmentation functions fit to high energy e^+e^- collisions. Figure from [73].

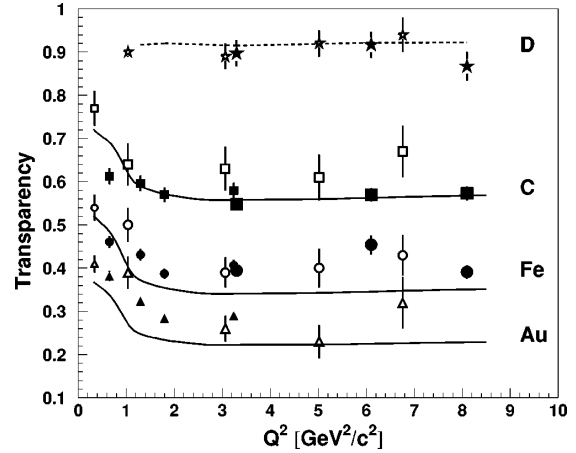


Figure 6: Measurement of transparency for $(e, e'p)$. Solid points are from Hall C measurements [74, 75]. At the largest Q^2 , the HMS momentum is > 5 GeV. Figure from [75].

imum central momentum of the SHMS is almost 11 GeV, 8.5 GeV/c was already sufficient to learn about the performance of the superconducting magnets and spectrometer optics when pushed to a significant fraction of the spectrometer's ultimate capabilities. In addition, the body of $H(e, e'p)$ data acquired for both these initial coincidence experiments served to provide constraints the experiment kinematics, allowing one to test the possible variation of, *e.g.*, the spectrometer pointing or central momentum for various settings.

A set of meson electroproduction experiments followed the initial commissioning experiments and further exercised the SHMS capabilities. Two of the experiments measured charged pion electroproduction in semi-inclusive deep inelastic scattering [60, 61]. The SHMS was used at central angles smaller than 7° for the SIDIS running. An additional challenge was the relatively high singles rates in the SHMS. Both experiments aim at making precise measurements of π^+/π^- ratios so control of rate dependent systematic effects is a key challenge. The third experiment [42] measured exclusive cross sections for K^+ production above the resonance region, in particular, extracting the longitudinal and transverse cross sections via a Rosenbluth separation. In this case, the experimental uncertainties are expected to be dominated by statistics, so this serves as an excellent candidate for an a first L-T separation since the

systematic requirements are less stringent. In common with the charged pion SIDIS experiments, the kaon experiment required use of the SHMS to small angles and had to face the challenge of high singles rates.

The “year-1” experiments described above give a sense of the SHMS capabilities important for the overall physics program. More recent experiments include measurements of J/Ψ photoproduction, Virtual Compton Scattering, measurement of the charged pion factor at very low Q^2 , and inclusive electron scattering from polarized ^3He to extract A_1^n and d_2^n . In the near future, measurements of the EMC Effect and at $x > 1$ (in both the inclusive and exclusive channels) from a variety of nuclei as well L-T separated π^+ cross sections (to extract the charged pion factor and measure the cross section scaling behavior at large Q^2) are planned. Further in the future, additional L-T separations in inclusive scattering (to measure $R = \frac{\sigma_L}{\sigma_T}$ from hydrogen, deuterium, and several nuclei) and semi-inclusive reactions (to make the first precise measurement of R for the SIDIS reaction) are also planned. With the addition of a recoil polarimeter, the SHMS will also be used in a measurement of the nuclear dependence of the ratio of proton elastic form factors, $\frac{G_E}{G_M}$. While not all future experiments will make use of the SHMS, it is a key component of the Hall C 12 GeV experimental program.

2. Specifications for the upgraded Hall-C Spectrometer complex

SHMS Specifications section. Author Organizer: H. Fenker

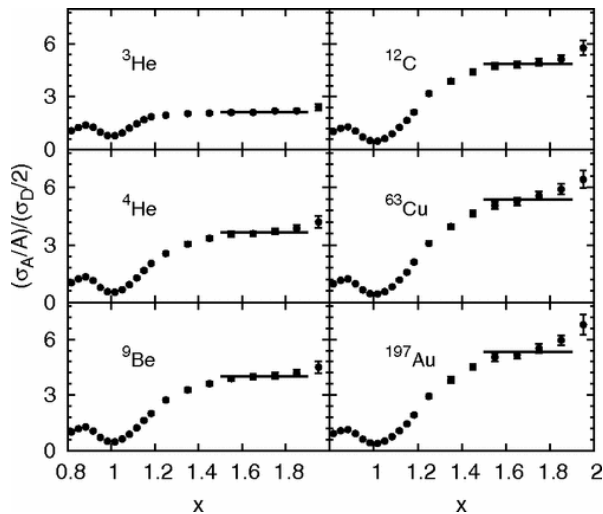


Figure 7: Measurements of cross section ratios for nuclear targets relative to deuterium at $x > 1$. The size of the ratio is proportional to the relative contributions of 2-nucleon Short Range Correlations to the nuclear wave function. These measurements required high momentum in the HMS. Figure from [77].

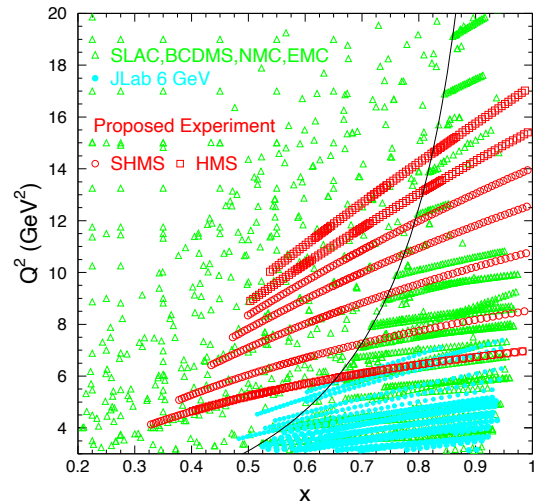


Figure 8: Kinematic coverage of F_2 measurements from experiment E12-10-002 [56], which measured inclusive electron scattering cross sections as part of Hall C's 12 GeV commissioning experiments.

203 The physics outlined in the previous section can be
 204 accessed only if the Hall C spectrometer system is capa-
 205 ble of providing the necessary measurements with
 206 precision, rate, and trigger capabilities consistent with
 207 those physics goals. Originally, Hall C offered the
 208 7.4 GeV/c High Momentum Spectrometer (HMS) and
 209 its lower-momentum (1.8 GeV/c) partner, the Short-
 210 Orbit Spectrometer (SOS). These two devices were uti-
 211 lized independently by some experiments and in coin-
 212 cidence by others. The performance specifications for
 213 the SHMS were drafted such that the SHMS-HMS pair
 214 would provide similar complimentary functions in the
 215 higher-momentum regime. That is, the SHMS was de-
 216 veloped as a general-purpose spectrometer with prop-
 217 erties similar to the existing HMS, but with a higher
 218 maximum momentum capability (11 GeV/c). The 11 GeV/c
 219 limit of the SHMS was selected because the accelera-
 220 tor constrained maximum beam energy to any of the first
 221 generation endstations (A,B,C) is 11 GeV/c. Table 1
 222 summarizes the demonstrated performance of the HMS
 223 and the design specifications for the SHMS.

224 With the higher beam energies in use at Jefferson Lab
 225 after the 12-GeV Upgrade, scattered electrons and sec-
 226 ondary particles are boosted to more forward directions.
 227 Thus the SHMS acceptance is made to extend down to
 228 a 5.5° scattering angle, and needs to cover angles
 229 no higher than 40° . Nevertheless, high energies gen-
 230 erally lead to smaller cross sections. Therefore preci-
 231 sion experiments can be performed only if a spectrom-

232 eter provides large overall acceptance, high rate capa-
 233 bility, and precise momentum measurement. As shown
 234 in Table 1, the SHMS design includes a momentum bite
 235 even larger than the HMS, and achieves an angular ac-
 236 ceptance within a factor of two of its low-energy part-
 237 ner. The combination of dispersive optics and preci-
 238 sion tracking provides excellent momentum resolution.
 239 Triggering, data-acquisition, and particle identifica-
 240 tion rates are the same or better than those of the HMS.
 241 This performance is achieved not only through the use of
 242 faster, modern electronics, but also by innovative radia-
 243 tion shielding that reduces the background flux seen by
 244 the detectors.

245 3. Design and Development of the SHMS Systems

246 In this section we present design details and data
 247 demonstrating the performance of each the SHMS sub-
 248 systems. The entire spectrometer is carried on a steel
 249 support structure which can rotate through an arc on the
 250 left side of the beam-line in Hall C. Like the HMS cari-
 251 age, it is secured to a central pivot so that it rotates
 252 around a vertical axis that intersects the electron beam-
 253 line at the experimental target. This is shown in Fig. 11.

254 Acceptance at the smallest scattering angles is en-
 255 abled by the presence of a horizontal-bending dipole as
 256 the first element in the magnetic optical system. This
 257 small deflection moves the subsequent pieces of the
 258 SHMS farther from the beamline, relaxing the size con-
 259 straints on the other magnetic elements (described in

<i>Parameter</i>	<i>HMS Performance</i>	<i>SHMS Specification</i>
Range of Central Momentum	0.4 to 7.4 GeV/c	2 to 11 GeV/c
Momentum Acceptance	$\pm 10\%$	-10% to +22%
Momentum Resolution	0.1% – 0.15%	0.03% – 0.08%
Scattering Angle Range	10.5° to 90°	5.5° to 40°
Target Length Accepted at 90°	10 cm	25 cm
Horizontal Angle Acceptance	± 32 mrad	± 18 mrad
Vertical Angle Acceptance	± 85 mrad	± 45 mrad
Solid Angle Acceptance	8.1 msr	4 msr
Horizontal Angle Resolution	0.8 mrad	0.5 – 1.2 mrad
Vertical Angle Resolution	1.0 mrad	0.3 – 1.1 mrad
Target resolution (y_{tar})	0.3 cm	0.1 - 0.3 cm
Maximum Event Rate	2000 Hz	10,000 Hz
Max. Flux within Acceptance	~ 5 MHz	~ 5 MHz
e/h Discrimination	>1000:1 at 98% efficiency	>1000:1 at 98% efficiency
π/K Discrimination	100:1 at 95% efficiency	100:1 at 95% efficiency

Table 1: Demonstrated Performance of the HMS and Design Specifications for the SHMS

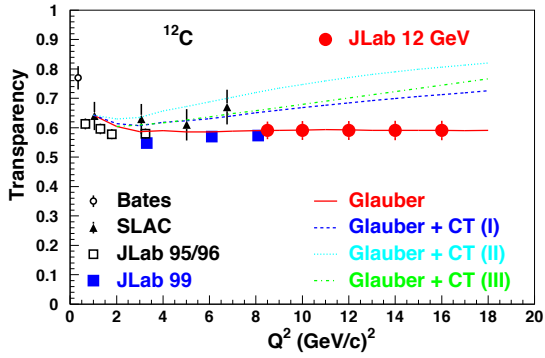


Figure 9: Projected uncertainties for the measurement of color transparency [59]. This measurement served as the first coincidence measurement in the 12 GeV era in Hall C.

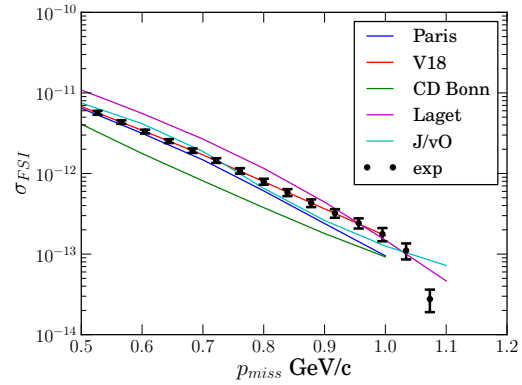


Figure 10: Projected uncertainties for the measurement of deuteron electrodisintegration at large missing momentum [58] (Hall C commissioning experiment).

260 Section 3.1) and shielding (Section 3.2). The shielded
 261 enclosure is itself a technically-optimized combination
 262 of concrete, lead, boron, and plastic. It surrounds the
 263 detectors and the electronics of the control and data-
 264 acquisition systems.

265 Basic trigger information comes from four planes
 266 of scintillator or quartz-bar hodoscopes. Tracking is
 267 provided by twelve planes of conventional drift cham-
 268 bers, and particle identification uses gas and aerogel
 269 Cherenkov counters, a preshower counter, and a total-

270 absorption shower counter. The detector system details
 271 are presented in sections 3.3 through 3.9. Details of the
 272 event-triggering schemes, the data-acquisition system,
 273 and software appear in sections 4 and 5.

274 *Editing notes.*

275 The subsections below (numbered 3.xx) are each as-
 276 signed to a technical subsystem author (or organizer), as
 277 indicated. The order of these subsections has not been

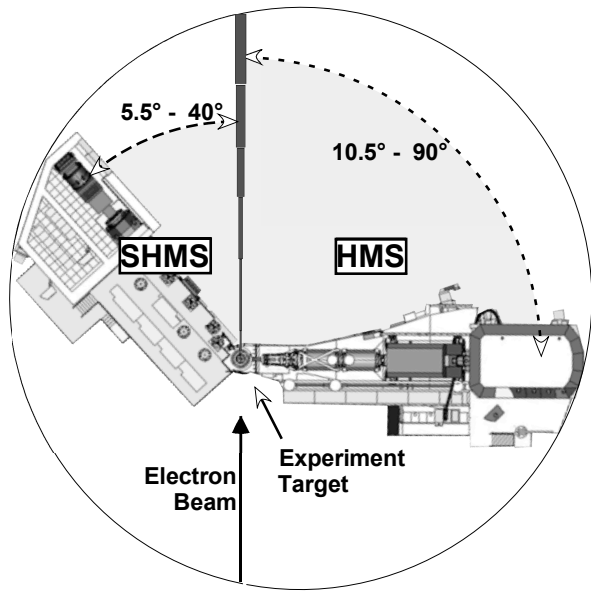


Figure 11: Simplified Plan View of Hall C showing the footprints of the SHMS and HMS. The SHMS occupies the smaller side of Hall C, where the smaller, low-momentum Short-Orbit Spectrometer (SOS) had been previously located.

278 given any thought yet. Each one should describe design
 279 and performance objectives, studies and test results that
 280 lead to the design choices, a description of the final design
 281 (here you might include pertinent drawings), and
 282 the results of bench-top or in-beam commissioning results
 283 that demonstrate how well the detector works (efficiency,
 284 photoelectron yield, pedestal width, timing resolution,
 285 or whatever is relevant for characterizing your
 286 piece of hardware).

287 3.1. Magnetic Optics

288 Magnetic Optics section. Author Organizer: M. Jones
 289

290 The SHMS consists of five magnets used to determine the
 291 momentum, angles and position of particles scattered from
 292 the target from their angle and position measurements in
 293 the SHMS detectors. The first is dipole magnet which
 294 bends the incident particles in the horizontal plane. A
 295 quadrupole triplet provides a point-to-point focus. To
 296 optimize acceptance in the vertical scattering plane, the
 297 first quadrupole focuses in the vertical while the second
 298 quadrupole defocuses and the third quadrupole focuses.
 299 A vertical-bending dipole magnet follows the last
 300 quadrupole and disperses particles with different momenta
 301 across the focal plane. In point-to-point optics, all
 302 particles with the same momentum will be displaced by
 303 the same vertical distance in the focal plane.
 304

305 3.1.1. The Magnets and Vacuum Channel

306 A specially-design horizontal-bend dipole (HB) precedes
 307 the first quadrupole. Its purpose is to provide an initial
 308 3° separation between scattered particles and the electron
 309 beam so that particles scattered at small angles can be
 accepted.

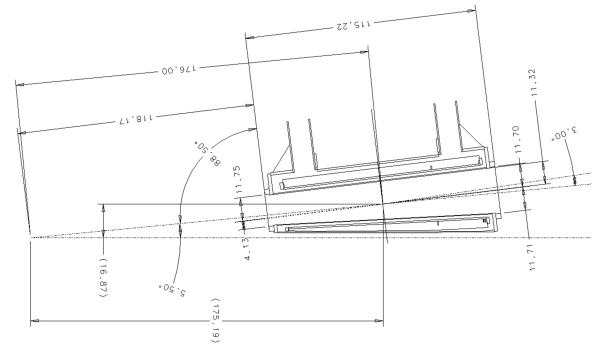


Figure 12: Top view schematic of the horizontal bender (HB) magnet. The center of the HB magnet is at 5.5° for the beam line and 176cm from the hall center.

310

311

312

313

314

315

316

317

318

319

320

321

322

323

324

325

326

327

328

329

330

331

332

333

334

335

336

337

338

339

As shown in Fig. 11, in order to fit within the space available in Hall C the SHMS must be even shorter than its lower-momentum partner, the HMS. All of the SHMS magnets are superconducting so that they can provide the necessary large bending and focusing effects in short distances. Given the small-angle acceptance requirement, the HB and the first two quadrupoles (Q1 and Q2) must have special provisions to provide clearance for the electron beam and its vacuum pipe. HB is a “C”-magnet so that all of the flux-return iron is on the side away from the beamline. The front of the HB cryostat, between the beamline and the magnet bore, is made very narrow. Both Q1 and Q2 have notches in their cryostats and iron yokes so that they, too, can clear the beamline when the spectrometer is configured at small scattering angles. Yoke steel for Q1 is inside the cryostat. The other magnets, including the final quadrupole (Q3) and the dipole (D_{SHMS}) have external, warm, yokes. Parameters of the SHMS magnets are provided in Table 2. Details about the design and construction of the SHMS magnets can be found in [3].

To minimize multiple scattering as particles pass through the SHMS, the bores of all of the magnets are evacuated. The vacuum space begins at a window on the front of HB and extends either to the exit of D_{SHMS} or, through a Vacuum Extension Tank (VET), to within 30 cm of the first drift chamber in the detector stack. The entrance window into HB is approximately 15 cm square, while the vacuum vessel bore through Q2, Q3,

340 and D_{SHMS} is 60 cm in diameter.

341 3.1.2. Optics

The relative strengths of the integral fields of the magnets are set to maximize acceptance while at the same time optimizing resolution in momentum and scattering angle. The transport of a particle with the relative momentum, $\delta = \frac{p-p_c}{p_c}$, from the target to midway between the two set drift chambers in the focal plane of the SHMS can be characterized by an optics matrix. The particle momentum is p and the central momentum of the spectrometer is p_c . The particle starts with the vertical and horizontal positions (x_{tar} and y_{tar}) and angles ($x'_{tar} = \frac{\Delta x_{tar}}{\Delta z_{tar}}$ and $y'_{tar} = \frac{\Delta y_{tar}}{\Delta z_{tar}}$) in the $z_{tar} = 0$ plane. These positions and angles are measured relative to the central ray of the spectrometer. After magnetic transport, it arrives at the focal plane with the vertical and horizontal positions (x_{fp} and y_{fp}) and angles (x'_{fp} and y'_{fp}). The first order optics matrix is

$$\begin{pmatrix} x_{fp} \\ x'_{fp} \\ y_{fp} \\ y'_{fp} \end{pmatrix} = \begin{pmatrix} -1.5 & 0.0 & 0.0 & 0.0 & 1.65 \\ -0.5 & -0.7 & 0.0 & 0.0 & 3.2 \\ 0.0 & 0.0 & -1.9 & -0.2 & -0.1 \\ 0.0 & 0.0 & -3.0 & -0.8 & 0.1 \end{pmatrix} \begin{pmatrix} x_{tar} \\ x'_{tar} \\ y_{tar} \\ y'_{tar} \\ \delta \end{pmatrix} \quad (1)$$

342 The units of the positions, angles and δ are in centimeters,
343 milliradians and %.

344 The acceptance of the spectrometer is mainly determined by the collimator that is placed between the HB
345 magnet and the first quadrupole. A remotely-operated
346 collimator box is installed on the SHMS between the
347 HB and Q1 magnets. The collimator ladder assembly
348 within this box may be positioned at three settings. The
349 top position (accessed when the assembly is at its low-
350 est position) is a stretched octagon with opening height
351 9.843" and width 6.693" on the upstream side. It is 2.5"
352 thick. The lower two positions both present sieve holes
353 in rectangular pattern with holes separated by 0.6457"
354 horizontally and 0.9843" vertically. The sieve pattern at
355 the middle ladder position has 11 columns of holes with
356 the sixth column centered horizontally. The holes on the
357 bottom sieve are in ten columns and are offset by one-
358 half a column gap from those in the middle sieve. The
359 sieve collimators are 1.25" thick. The geometry is illus-
360 trated in Fig. 13. Both sieves and octagonal collimator
361 are made of Mi-Tech™ Tungsten HD-17 (Density 17
362 g/cc, 90% W, 6% Ni, 4% Cu).

364 To determine the vertical size of the collimator stud-
365 ies were done with SNAKE (magnet transport code).
366 Without the collimator, the vertical acceptance is mainly
367 determined by the mechanical exit of the HB magnet.

368 The vertical size of ± 12.5 cm was chosen to match this
369 vertical cut-off to maximize the acceptance. Two ver-
370 tical sizes of ± 8 cm and ± 10.5 cm for the collimators
371 were studied. A plot of the acceptance each collimator
372 versus δ is shown in Figure 14. The acceptance drops
373 from an average of 4 msr for ± 12.5 cm to an average
374 of 3 msr for ± 8 cm. Another consideration minimizing
375 the loss of events in the bore of the vertical dipole after
376 they pass the entrance of the dipole. A plot in Figure 14
377 shows the fraction of events which make it to the fo-
378 cal plane. The number of events lost in the dipole bore
379 as a function of δ is reduced by decreasing the vertical
380 height of the collimator. With the ± 12.5 cm collimator
381 , the fraction of events making to the focal plane drops
382 to 75% at $\delta = 0.15$. The decision was made to use
383 the ± 12.5 cm vertical opening to maximize the solid an-
384 gle acceptance of the SHMS at the expense of increased
385 reliance on the understanding the losses in the SHMS
386 dipole bore.

387 A magnetic transport code, SNAKE, was used to
388 model the acceptance of the SHMS. The mechani-
389 cal sizes of the magnets and magnet field maps from
390 TOSCA are used to create a model of the SHMS in
391 SNAKE. The acceptance of the SHMS versus δ deter-
392 mined by SNAKE is plotted in Fig. 15. A separate cal-
393 culation is done using the Hall C Monte Carlo (SIMC)
394 which uses COSY transport matrix. The acceptance of
395 the SHMS versus δ determined by SIMC is plotted in
396 Fig. 15. The agreement between the two calculations is
397 excellent.

The reconstruction of particle's momentum, horizon-
tal target position and vertical and horizontal angles
from the focal plane positions and angles can also be
represented by an optics matrix. Each event calcu-
lates the target interaction point from the tracks recon-
structed in the focal plane using the drift chamber infor-
mation. Target offsets, beam offsets and spectrometer
mis-pointings are accounted for separately when recon-
structing events. The optics matrix elements consist of
a set of coefficients and the values of the powers for
each focal plane element. The coefficients for each fo-
cal plane variable are X' , Y , Y' , and D , and the powers
of each focal plane variable are represented by $ijklm$.
The reconstruction equations for the target quantities are
written as shown in Eq. (2).

<i>Parameter</i>	<i>HB</i>	<i>Q1</i>	<i>Q2</i>	<i>Q3</i>	<i>D_{SHMS}</i>
Max Field or Gradient	2.6 T	7.9 T/m	11.8 T/m	7.9 T/m	3.9 T
Effective Field Length	0.80 m	1.9 m	1.6 m	1.6 m	2.9 m
Current at 11 GeV/c	3923 A	2322 A	3880 A	2553 A	3510 A
Aperture	14.5x18 cm	40 cm	60 cm	60 cm	60 cm

Table 2: Parameters of the SHMS Magnets

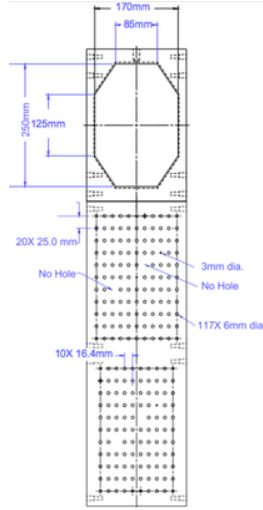


Figure 13: SHMS collimator

$$\begin{aligned}
x'_{tar} &= \sum_{ijklm} X'_{ijklm} x_{fp}^i x'_{fp}{}^j y_{fp}^k y'_{fp}{}^l x_{tar}^m \\
y_{tar} &= \sum_{ijklm} Y_{ijklm} x_{fp}^i x'_{fp}{}^j y_{fp}^k y'_{fp}{}^l x_{tar}^m \\
y'_{tar} &= \sum_{ijklm} Y'_{ijklm} x_{fp}^i x'_{fp}{}^j y_{fp}^k y'_{fp}{}^l x_{tar}^m \\
\delta_{tar} &= \sum_{ijklm} D_{ijklm} x_{fp}^i x'_{fp}{}^j y_{fp}^k y'_{fp}{}^l x_{tar}^m
\end{aligned} \quad (2)$$

413 From Eq. (2), it can be seen that the target reconstruction
414 tion is actually under-determined. For each event, there
415 are four givens (x_{fp} , y_{fp} , x'_{fp} , y'_{fp}) and five unknowns to
416 solve for (x_{tar} , y_{tar} , x'_{tar} , y'_{tar} , and δ). x_{tar} is never directly
417 measured, but it is reconstructed with the knowledge of

418 the beam position and reconstructed values of y_{tar} , x'_{tar} ,
419 y'_{tar} . The x_{tar} independent terms are optimized from data
420 while the x_{tar} dependent terms are used directly from
421 COSY. δ is optimized by using carbon elastic data.

422 The calibration of the reconstructed matrix elements
423 was done using data from specific run settings. In all
424 cases, a single or multi-foil carbon target is used with
425 a sieve installed downstream from the target. For each
426 interaction that pass through a sieve hole, all true target
427 quantities can be determined.

428 The calibration of the δ matrix elements was done us-
429 ing carbon elastic data. Using the first order optics from
430 COSY and selecting events from a carbon target inter-
431 action that pass through a single hole in the sieve, the
432 carbon elastic peak and excitation spectrum is clearly
433 seen as shown in Fig. 16.

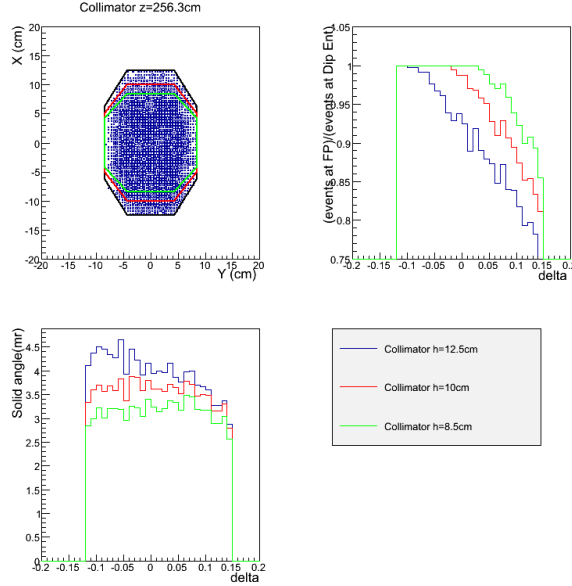


Figure 14: The upper left figure is distribution of events at the location of the collimator with three different vertical size collimators. The lower left figure is the acceptance as a function of δ for each of the collimators. The upper right figure is the fraction of events lost in the dipole bore after the dipole entrance.

434 The carbon energy spectrum shows the elastic peak 455
 435 and the 4.4 MeV carbon excited state. Additional carbon 456
 436 carbon states are observable in the smaller peaks to the 457
 437 right of the 4.4 MeV peak. The δ matrix elements were 458
 438 optimized by taking a series of runs where the carbon 459
 439 elastic peak moved across the focal plane for incremental 460
 440 settings of the spectrometer central momentum. [M. Jones](#) can elaborate here. 441

442 The optimization of the reconstructed target quanti- 463
 443 ties y_{tar} , y'_{tar} , and x'_{tar} used data from multi-foil carbon 464
 444 targets with the sieve inserted in the beam line. Each 465
 445 hole in the sieve is used to define the true physical values 466
 446 of an event and is compared to the reconstructed angles 467
 447 and positions for optimization. The reconstructed y_{tar} 468
 448 is approximately $z_{tar} \sin \theta$ where θ is the central angle 469
 449 of the spectrometer, and z_{tar} is the target foil position in 470
 450 the hall beam line coordinate system. To optimize over 471
 451 the full range of possible y_{tar} values, data must be taken 472
 452 with the spectrometer at various central angles. Two 473
 453 sieves were used to collect the data having the same hole 474
 454 patterns: one where the central hole was centered on the 475

spectrometer axis and the other where the central hole 455
 was shifted by half the distance between the holes relative 456
 to the spectrometer axis. Data was taken with each 457
 sieve separately in order optimize the full spectrometer 458
 acceptance. A reconstructed sieve pattern using a single 459
 carbon foil is shown in Fig. 17. 460

461 The general procedure for the optimization of the 462
 target quantities y_{target} , y'_{target} , and x'_{target} is as follows: 463
 the events are initially reconstructed using the original 464
 reconstruction matrix elements generated from the 465
 COSY model. These events are used to determine the 466
 true physical values by determining which target foil an 467
 event originated from and which sieve hole the event 468
 passed through. The differences between the measured 469
 events and the real true physical values are minimized 470
 by solving a Singular Value Decomposition (SVD) to 471
 calculate the optimized/improved reconstruction matrix 472
 elements.

473 [Need to mention the reconstructed angular resolu-](#)
 474 [tions. From CT, I obtained 0.9 mrad horizontal and](#)
 475 [1.1 mrad vertical.](#)

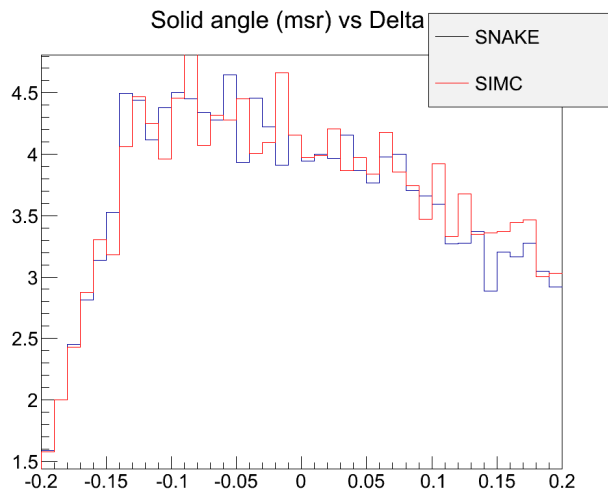


Figure 15: Comparison of predicted SHMS acceptance using the Hall C Monte Carlo (SIMC) and the magnetic transport code SNAKE.

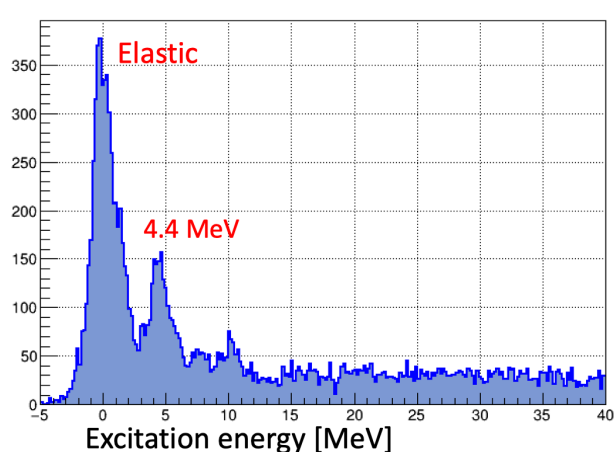


Figure 16: The carbon elastic energy spectrum for events for a single sieve hole, as calculated in terms of delta from the first order optics, clearly shows the carbon elastic peak and the 4.4 MeV excited state.

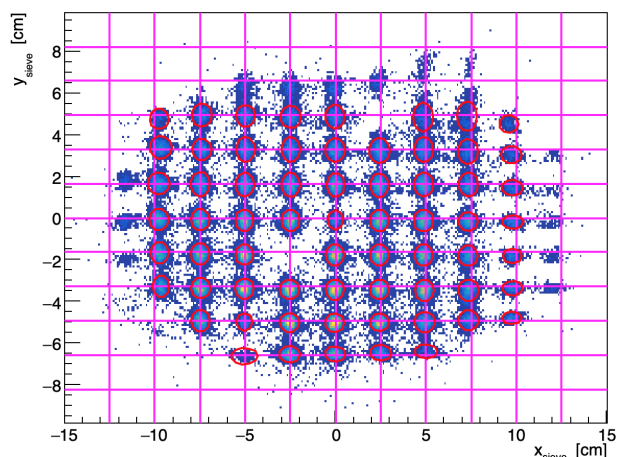


Figure 17: The sieve pattern is reconstructed here where the true sieve hole positions are indicated by the magenta cross lines and the reconstructed holes are outlined in red. The holes at the edges of the sieve are somewhat shifted from the true desired values.

476 3.2. Shield House Layout, Shielding Design

477 **Shield House layout and materials section. Author**
 478 **Organizer: T. Horn**

479 The radiation environment is an important considera- 487
 480 tion for the design of the SHMS shield house, in particu- 488
 481 lar, the effect of radiation-induced effects on the perfor- 489
 482 mance and reliability of detectors and electronics. 490
 483 It has been shown that many new commercial off the 491
 484 shelf components are more sensitive to radiation damage 492
 485 and single event upsets, requiring a careful evalu- 493

486 ation of the impact of the radiation-induced effects on
 their performance and reliability [28, 29]. A specialized
 SHMS shield house design was thus developed at Jef-
 ferson Lab. Shielding thicknesses were optimized using
 a Monte Carlo simulation and benchmarked against the
 HMS shielding house, which has proven to provide the
 necessary detector shielding over more than a decade of
 experiments at the 6 GeV JLab. A full description of the

shielding optimization can be found in Ref. [27].

The primary particle radiation is created when the CEBAF electron beam strikes the experimental target. The main components are scattered electrons, neutral particles (photons and neutrons), and charged hadrons. The energy spectrum of this radiation depends on the incident beam energy and decreases generally as $1/E$. It has been shown that the most efficient way to protect the experimental equipment from radiation damage is to build an enclosure around it using certain key materials. The type and thickness of the shield house walls depends on the energy and particle one needs to shield against. However, one may qualitatively expect that the largest amount of shielding material is needed on the side facing the primary source, which in the case of the Hall C focusing spectrometers is the front face. Additional sources of radiation are the beampipe, which extends from the experimental target to the beam dump, and the beam dump area itself. Thus, the faces of the spectrometer exposed to direct sources of radiation are the front, beam side, and the back walls.

Primary and scattered electrons lose a significant amount of energy as they traverse a material by producing a large number of lower energy photons through bremsstrahlung [30]. It is thus important to consider shielding materials that efficiently stop the latter as well.

Neutral particles have a higher penetration power than charged particles. They are attenuated in intensity as they traverse matter, but do not continuously lose energy. Photons interact in materials almost exclusively with electrons surrounding the atom or by pair production in the field of the nucleus. The probability for an interaction depends on the atomic number of the material. Neutrons interact with atomic nuclei in a more complicated way.

An additional source of radiation is due to charged hadrons (e.g. protons, pions). However, the probability for producing hadron radiation is relatively low, and thus will be neglected here. The shielding is, nevertheless, effective for charged hadrons. The front wall will, for instance, stop 1 GeV protons.

Fig. 18 shows a schematic of the SHMS shielding plan. The SHMS shield house is similar to the HMS design, but has several new features due to additional requirements. For example, the space between the beam side shield wall and the beam pipe is limited at very forward angles, and in addition, the length of the SHMS detector stack and minimum distance between the back of the detector house to the hall wall requires a reduction in thickness of the concrete shield wall.

Typical beam-target geometries were simulated using Monte Carlo techniques. Simulations were performed

using the GEANT MCWORKS distribution, which includes detailed physical and geometric descriptions of the experimental hall and simulates the physics processes using standard GEANT3 together with the DINREG nuclear fragmentation package. Hadronic interactions are treated using the DINREG package, which calculates the probability of such interactions using a database of photonuclear cross sections. For electron-nucleus interactions an “equivalent photon” representation of the electron (or positron) is used.

In this simulation, the CEBAF beam electrons start 1 m upstream of the target, strike it head-on along the cylindrical symmetry axis, and have no momentum component transverse to the beamline. The simulation also includes the beam pipe, target entrance and exit windows, and the entire geometry of Hall C, including all elements of the beam dump. The transmission of particles through the shielding materials was calculated as a function of the material thickness and the angle relative to the beam direction.

A limitation of the radiation studies is the lack of cross section data for low-energy neutrons. The accuracy of the GEANT simulations was tested by benchmark calculations using the MCNP code [31] with an isotropic neutron point source of 1 MeV located 1 m from the shield wall. The MCNP calculations suggest that 50cm of concrete thermalizes most of the fast neutrons, and after 1 m practically no epithermal neutrons remain. The thermalized neutrons can be captured by a 1cm Boron layer. In reality, however, the neutron spectrum also includes higher energy neutrons, for instance produced by electrons interacting in the concrete, and thus the actual amount of material for the walls exposed to the primary sources of radiation has to be thicker. A simple transmission calculation using GEANT4 for incident neutron beams of energies between 1 and 10 MeV suggests that a thickness 150cm of concrete is sufficient to stop the majority of low-energy neutrons [32].

The SHMS shielding model is composed of standard concrete ($\rho=2.4 \text{ g/cm}^{-3}$). The thickness of the wall in front of the detector and electronics rooms is 200 cm to shield from the primary radiation source around the target. Figure 19 shows the surviving background flux for varying front wall concrete thicknesses. The results are normalized to the background flux in the HMS at 20° . This angle was chosen as experiments in Hall C have shown that electronics problems seem to dominate at lower angles [33]. The simulation results suggest that 200 cm of concrete reduces the total flux to half of the HMS at 20° .

Figure 20 shows the energy spectra for surviving photons and neutrons with varying front wall thickness. In

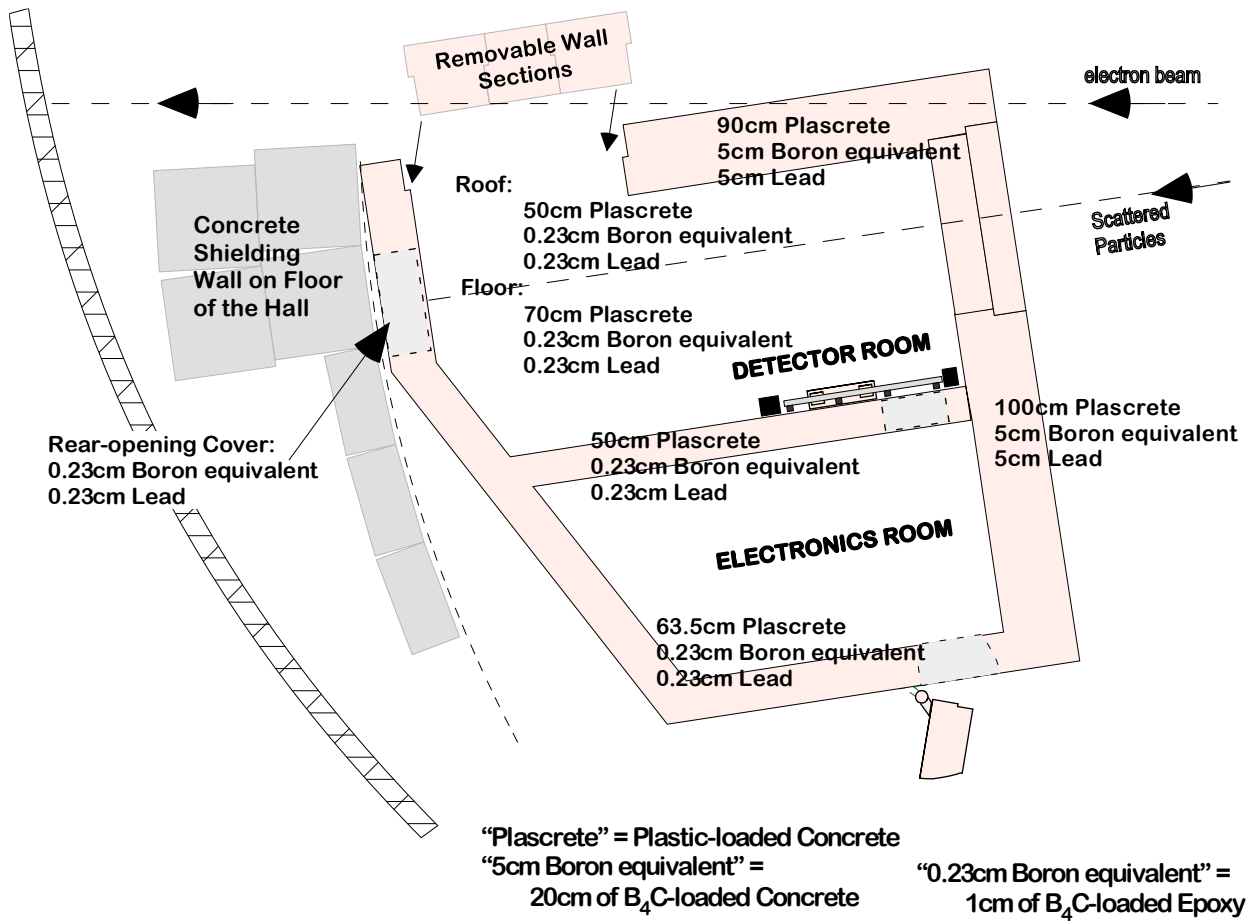


Figure 18: Plan View of the SHMS Shield House showing the layout, thickness, and composition of the walls.

598 order to optimize the shielding, these secondary particles 617
 599 have to be absorbed as well. Our assumption on radiation 618
 600 damage is that photons below 100 keV will not 619
 601 be a significant source of dislocations in the lattice of the 620
 602 electronics components, while neutrons will cause radi- 621
 603 ation damage down to thermal energies. Adding lead to 622
 604 the concrete wall reduces the photon flux significantly, 623
 605 but it does not help for neutrons. On the other hand, 624
 606 the boron reduces the flux of very low energy neutrons. 625
 607 Assuming that low energy photons and neutrons cause a 626
 608 significant fraction of the radiation damage, then adding 627
 609 the relevant material would be important. 628

610 The thickness of the beam-side wall (shielding from 629
 611 an extended source, the beamline) is constrained by the 630
 612 clearance with the detector stack inside the enclosure 631
 613 and the beamline at small angles. Conservatively as- 632
 614 suming a clearance of 5cm between detector stack and 633
 615 the shield wall, the total concrete wall thickness is lim- 634
 616 ited to 105cm. A 90cm concrete wall combined with 635

a 5cm boron and 5cm lead layer provides the optimal 617
 shielding configuration. Adding boron is not much dif- 618
 ferent from adding (or replacing) concrete, but in addi- 619
 tion it captures thermal neutrons. 620

621 The majority of charged particles is stopped by the 622
 623 outer walls of the spectrometer shield house. An addi- 624
 625 tional source of radiation may be created from particles 626
 627 entering the enclosure through the magnets. In order to 628
 629 protect the electronics further, an intermediate wall was 630
 631 installed between the detector and electronics rooms. 632
 Figure 21 shows the normalized rate as the thickness of 633
 this intermediate wall is varied. This suggests that the 634
 optimal configuration is provided by a concrete thick- 635
 ness of 80-100 cm². Further details on shielding con- 636
 figurations investigated and their optimization can be 637
 found in Ref. [27].

²Note that a minimum wall thickness of 50cm is needed to provide support for the roof of the shield house

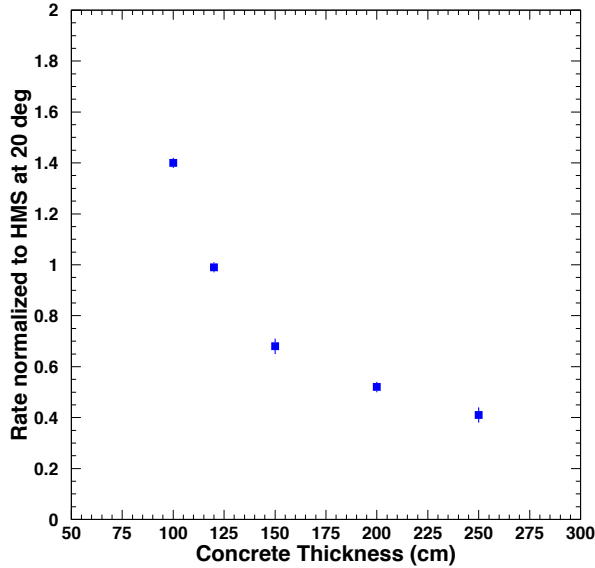


Figure 19: The normalized background rate vs. front wall thickness. The rates are normalized to those found in the HMS at 20°.

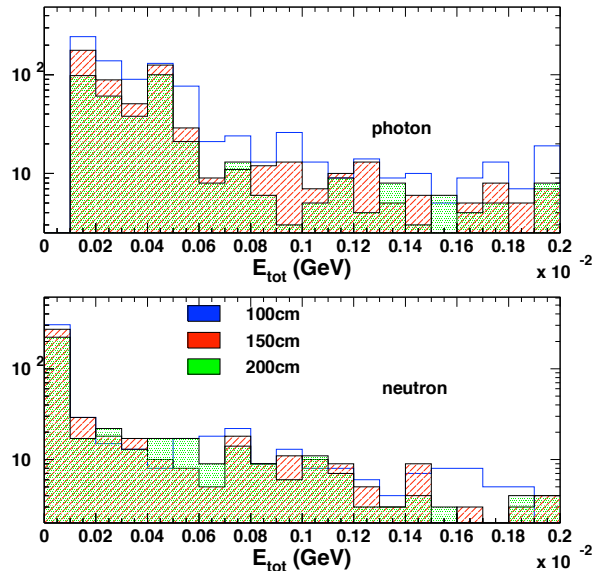


Figure 20: The outgoing particle spectrum, which is soft (< 10 MeV).

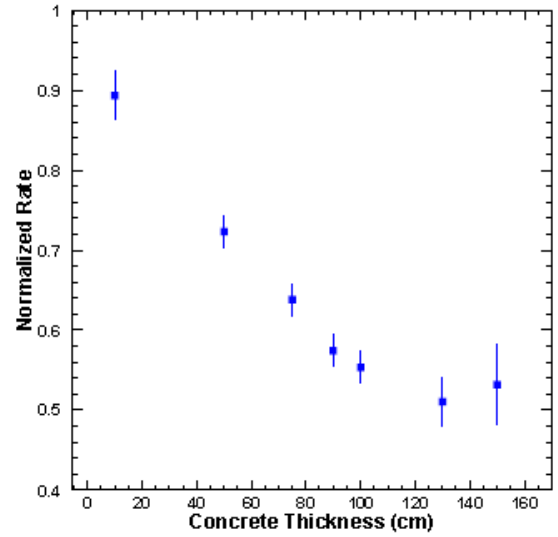


Figure 21: The normalized rate versus the intermediate concrete wall thickness.

633 The hydrogen-rich concrete walls function as a
 634 shield, an absorber, and a neutron moderator, and are
 635 thus placed on the outside of all faces of the shield
 636 house. On the other hand, the ordering of lead and boron
 637 to shield against the photon and neutron flux may, at first
 638 glance, not be obvious, and is discussed in detail below.

639 The incoming photon flux has two components: ex-
 640 ternally produced photons and bremsstrahlung photons
 641 produced by electrons in the twenty radiation lengths of
 642 concrete. The simulations have shown that the outgo-
 643 ing photon spectrum is soft (<10 MeV). Placing a lead
 644 layer after the concrete is essential to suppress this low
 645 energy photon flux. The (γ, n) reaction in lead is not a
 646 problem. The threshold for the reaction is given by the
 647 neutron binding energy (~ 8 MeV). At higher energies,
 648 the cross sections are in the mbarn range [34]. Even dis-
 649 regarding the low cross section, however, it is not clear
 650 that this reaction adds to the radiating of the electron-
 651 ics, because a high energy photon is replaced by a low
 652 energy (but not thermal) neutron.

653 The incoming neutron flux also has two components.
 654 Neutrons from excited nuclei will typically not exceed
 655 10 MeV. The other neutrons are produced through direct
 656 interactions with only one nucleon in the nucleus.
 657 These will have high energies, but the flux is low. As
 658 shown by the MCNP calculation, which has reliable low
 659 energy neutron cross sections, 0.5m of concrete almost
 660 fully thermalizes 1 MeV neutrons. Thus, 2m of con-
 661 crete should be sufficient to thermalize the first com-
 662 ponent. Some of these will be captured in the con-

663 crete, but to eliminate the surviving thermal neutrons
 664 a layer of boron is needed. There are two relevant reac-
 665 tion channels: (n, γ) and $(n, \alpha\gamma)$. The former produces
 666 high energy photons, but the cross section is relatively
 667 small. The latter produces a 0.48 MeV photon for ev-
 668 ery captured neutron. The thermal cross section is about
 669 10kbarn, and even at 1 MeV it is still in the barn range.
 670 The majority of neutrons can thus be expected to be cap-
 671 tured in a sufficiently thick boron layer. An optimal
 672 shielding configuration would also stop these photons
 673 produced in the capture. At 0.48 MeV, the photoelectric
 674 effect and Compton scattering contribute about equally
 675 to the attenuation in lead. Photons from the latter will
 676 also need to be absorbed.

677 Thus, placing the lead in front of the boron layer has
 678 limited benefit. It will not affect the neutron flux, but
 679 will create an additional source of photons. The more
 680 lead one places after the boron, the more efficiently
 681 these photons will be suppressed. From the point of
 682 view of stopping bremsstrahlung photons, the order of
 683 boron and lead layers does not matter. Thus, all lead
 684 should be placed after the boron.

685 Fig. 22 is a photograph showing the resulting multi-
 686 layered shielding in one of the SHMS shield house
 687 walls. The ceiling, floor, and other walls have simi-
 688 lar compositions but varying dimensions as shown in
 689 Fig. 18. Details about the development of custom
 690 concrete material containing boron can be found in
 691 Ref. [35].

692 In summary, the SHMS shielding consists of concrete
 693 walls to moderate and attenuate particles. Low energy
 694 (thermal) neutrons are absorbed in a boron layer inside
 695 the concrete. Low energy and 0.5 MeV capture photons
 696 are absorbed in lead. With this design, the rates at for-
 697 ward angles of 5.5° are estimated to be less than 70% of
 698 the design goal (HMS at 20°) in the detector room and
 699 below 50% in the electronics room.

700 3.3. Scintillator Trigger Hodoscopes

701 **Scintillator Hodoscopes section. Author Organizers:**
 702 **I. Niculescu, G. Niculescu**

703 The SHMS hodoscope system provides a clean trig-
 704 ger and trigger time information as well as the defi-
 705 nition of the detector package fiducial area, required
 706 for physics cross section measurements. The system is
 707 composed of four separate planes of detector paddles:
 708 S1X and S1Y located immediately after the second drift
 709 chamber and S2X and S2Y approximately 2.6 m away
 710 along the z direction. The S1X, S1Y, and S2X planes
 711 were built using thin scintillator paddles while S2Y uses
 712 quartz bars.

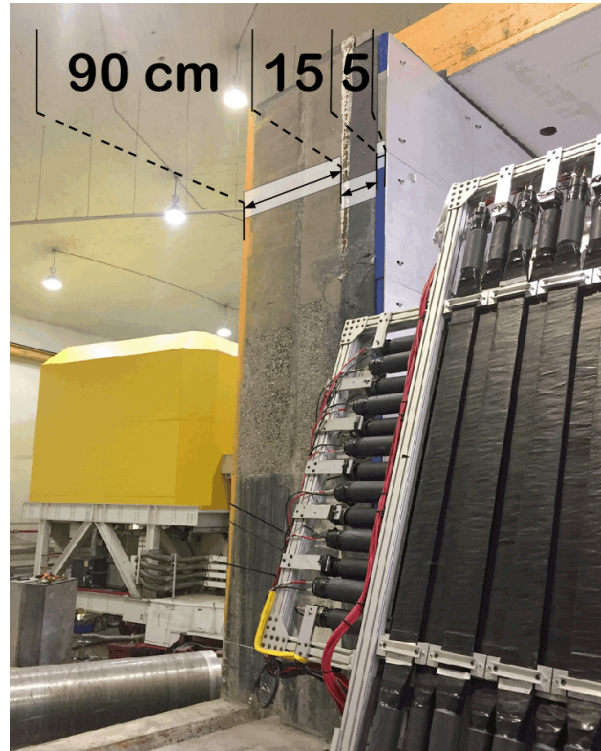


Figure 22: Photograph of the SHMS beam-side Shield Wall in cross-section view, showing the layers of different materials making up the wall.

713 3.3.1. Design and Construction

714 The overall dimensions and granularity of the three
 715 scintillator planes were driven by the Monte Carlo sim-
 716 ulations of the SHMS acceptance. The S1X and S1Y
 717 planes cover a $1000 \times 980 \text{ mm}^2$ area while the S2X plane
 718 covers $1100 \times 1335 \text{ mm}^2$. Further design constraints
 719 for this detector include high ($\geq 99\%$) detection effi-
 720 ciency, position independent along the scintillator pad-
 721 dle; good time resolution ($\sim 100 \text{ ps}$); high rate capabil-
 722 ity ($\sim 1 \text{ MHz/cm}$). As the detector's lifetime is assumed
 723 to be a decade or more stable, cost effective, and readily
 724 available materials and readout chain were used.

725 To meet the requirements listed above the SHMS Ho-
 726 doscope was built as a series of arrays (planes) of plastic
 727 scintillator paddles. The S1X and S1Y planes have 13
 728 $1000 \times 80 \text{ mm}$ paddles each, while the S2X plane has 14
 729 $1100 \times 100 \text{ mm}$ paddles. For each of the three scintillator
 730 planes the paddles were staggered by 7 mm and over-
 731 lapped by 5 mm. To minimize the impact of the scintil-
 732 lators on downstream detectors and also to ensure good
 733 timing resolution the thickness of paddles was 5 mm.

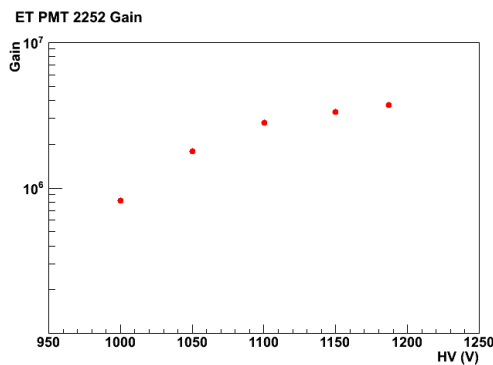
734 The scintillator material used was Rexon RP-408.
 735 The paddles were wrapped by the manufacturer with

736 millipore paper, aluminum foil, and 2" wide electrical 768
 737 tape. The transition between the thin scintillator mate- 769
 738 rial and the photomultiplier (PMT) tubes used for read- 770
 739 out was done using a Lucite fishtail-shaped light guide. 771
 740 As the glued joint between the scintillator paddle and 772
 741 the light guide is rather fragile (5x80 and 5x100 mm 773
 742 joints) aluminum "splints" were used to reinforce it. 774
 743 The PMT to fishtail joint was originally wrapped with 775
 744 2" tape as well and light-leak tested; subsequently this 776
 745 wrapping was reinforced with TEFLON tape and a 3" 777
 746 heat-shrink sleeve.

747 Each scintillator is read at both ends by PMTs glued 778
 748 to the fishtail using optical glue (BC-600) matching the 779
 749 index of refraction of the Lucite. A combination of Pho- 780
 750 tonis XP 2262 and ET 9214B 2" tubes were used. Both 781
 751 models have 12-stage amplification and their maximum 782
 752 photocathode sensitivity is in the blue-green range. The 783
 753 typical gain is 3×10^7 . Gains were measured as a 784
 754 function of high voltage during the construction and
 755 the whole hodoscope was gain matched *in situ* once in-
 756 stalled in SHMS.

757 3.3.2. Performance

758 All scintillator paddles and the PMTs used to build
 759 the S1X, S1Y, and S2X planes were extensively tested
 760 during assembly: the dark current and the gain as a
 761 function of the high voltage were measured for each
 762 tube; the finished paddles were light-leak tested and
 763 their detection efficiency as a function of position along
 764 the paddle was measured using cosmic rays on an au-
 765 tomated test stand. A typical gain versus HV graph is
 766 shown in Fig. 23.



767 Figure 23: Gain versus high voltage graph for an ET tube used for the
 768 scintillator hodoscope.

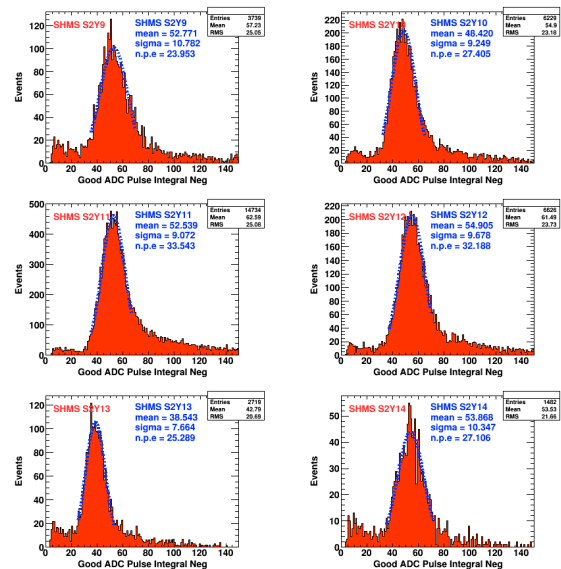
769 Once installed in the SHMS detector hut all paddles 796

were retested and gain matched. During the Hall C com-
 missioning experiments carried out during the Spring
 2018 the scintillators performed as expected with no
 major problems. [Might want to put more text/a picture
 here, maybe time resolution, efficiency, etc?](#)

773 3.4. Quartz-bar Trigger Hodoscope

774 Quartz Hodoscope section. Author Organizer: S.
 775 Malace

776 The SHMS hodoscope quartz plane was designed to
 777 help with neutral background rejection in the 12 GeV
 778 high-rate environment. It operates on the principle of
 779 Cherenkov light production by electrically charged par-
 780 ticles. It is one of the four hodoscope planes that form
 781 the basic 3 out of 4 trigger in the SHMS. In what fol-
 782 lows the design and construction of this detector will be
 783 presented as well as its performance with electron beam
 784 in Hall C.



785 Figure 24: Number of photoelectrons response from the quartz plane.

786 subsection Design and Construction

787 The design and construction of the SHMS ho-
 788 doscope quartz plane was done by the North Car-
 789 olina A&T group led by Abdellah Ahmidouch and
 790 Samuel Danagoulian. Quartz bars of x,y,z dimen-
 791 sions with an index of refraction of 1.5 were chosen. The
 792 Cherenkov light produced by electrically charged par-
 793 ticles was detected by quartz window ET9814QB pho-
 794 tomultiplier tubes optically coupled to the quartz bars
 795 through RTV615 rubber silicon of 50μ thickness. Af-
 796 ter a while in storage the quartz window photomul-
 tiplier tubes showed signs of vacuum contamination (He

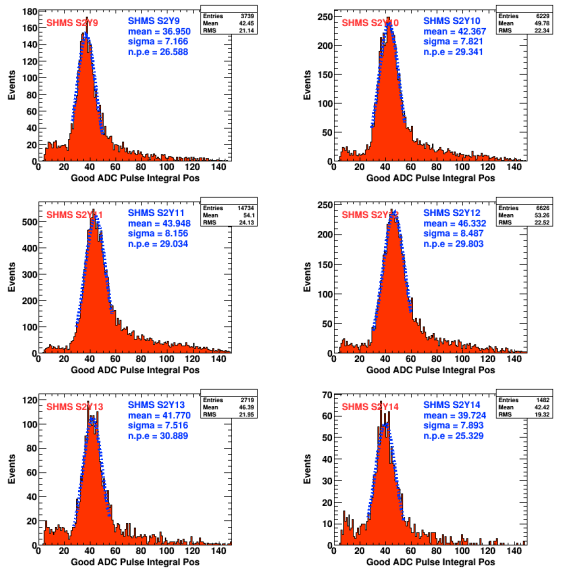


Figure 25: Number of photoelectrons response from the quartz plane.

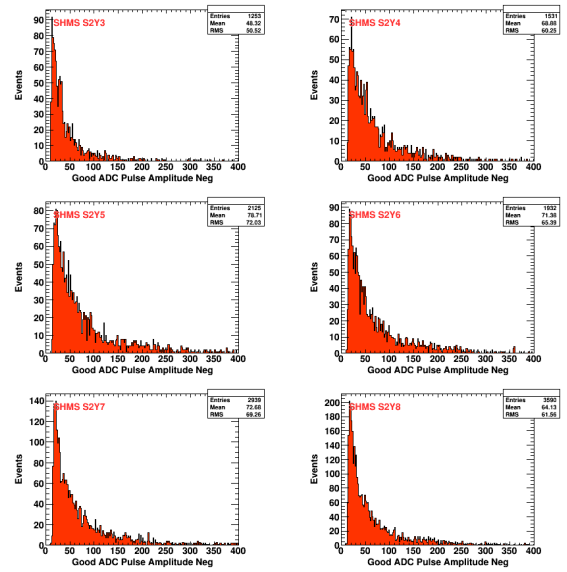


Figure 27: PMT pulse amplitude from pions with momenta of 1.96 GeV.

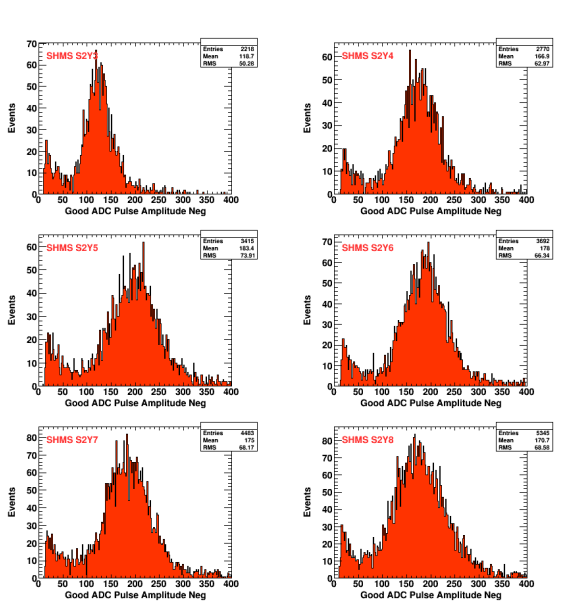


Figure 26: PMT pulse amplitude from pions with momenta of 1.96 GeV.

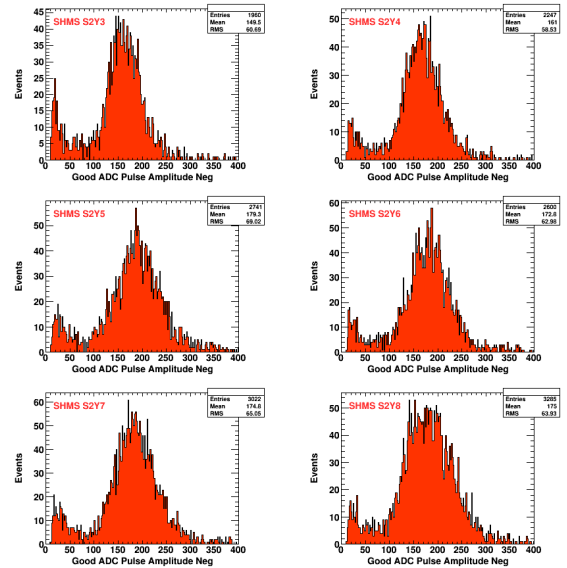


Figure 28: PMT pulse amplitude from protons with momenta of 5.05 GeV.

797 gas poisoning was suspected) and were eventually re-
 798 placed at Jefferson Lab with UV-glass window PMTs
 799 ET9814WB. There are 16 bars in use in the hodoscope
 800 quartz plane with an overlap between adjacent bars of
 801 x cm. This covers x % of the SHMS acceptance. The
 802 quartz plane frame allows for more bars to be added.

803 3.4.1. Performance

804 The performance of the detector was studied with
 805 beam during the Hall C commissioning in Fall of 2017.
 806 A plot of the photoelectron response from most bars in
 807 the quartz plane is shown in Fig. 24 and Fig. 25. Only
 808 electrons with an incident angle close to 90 deg were
 809 chosen here to eliminate the bias coming from possibly
 810 reduced photon collection efficiency due to sub-optimal

811 angles of the photon cones. All PMTs and optical couplings performed satisfactory.

812
813 The threshold for Cherenkov light production in the quartz bars for electrons, pions, kaons and protons is shown in Fig. fig:TBD. Beam data confirmed the expectation that the detection efficiency for low momentum protons, for example, will be smaller than that for pions or electrons simply due to the reduced number of Cherenkov photons that particles close to their firing threshold will produce. This is exemplified by Fig. 26, Fig. 27 and Fig. 28.

822 3.5. Drift Chambers

823 The SHMS horizontal drift chambers provide information to determine the trajectory of charged particles passing through the detector stack. The drift chamber package consists of two horizontal drift chambers separated by a distance of 1.1 m and oriented in the detector stack such that the sense wires planes are perpendicular to the central ray. Each chamber consists of a stack of six wire planes providing information on the track position along a single dimension in the plane of the wires and perpendicular to the wire orientations to better than $250\ \mu\text{m}$. The perpendicular distance of the track relative to the wire is determined from the time of the signal produced by the ionization electrons as they drift from their production point to the wire in an electric field of approximately 3700 V/cm.

838 The basic design and construction technique is based on that of previous successful chambers built for the Hall C 6 GeV program, which have been shown to reach the resolutions and particle rate specifications of the SHMS. The open layout design consists of a stack of alternating wire and cathode foil planes; each plane consisting of 1/8 inch thick printed circuit board (PCB). These are sandwiched between a pair of aluminum plates on the outside, which provide both the overall structural support and the precise alignment of each board via dowel pins at the corners. Just inside each plates is a fiberglass board with the central area cut out and covered with a vacuum stretched film of aluminumized Mylar, which provides the gas window. These are sealed to prevent gas leakage via an o-ring around the gas fitting through-hole on the inside of the plate.

854 Each chamber consists of two identical half chambers separated by a fiberglass mid-plane, which is utilized for mounting the amplifier discriminator cards required for the sense wire readout. To minimize the production costs, only two unique PCB types were designed: an X-plane with wires oriented horizontally (Left Panel of Figure 29), and a U-plane with wires oriented at +60 degrees relative the X-plane (Right Panel of Figure 29).

862 All other plane orientations are generated by rotations of these two basic board types. For instance, the boards are designed such that a rotation of 180 in-plane about an axis through the center of the board produces boards with wires of the same orientation, but shifted by 1/2 cell width, thus allowing the resolution of left/right ambiguities. Rotation of Figure 29 such that the top becomes the bottom produces the X' and U' orientations. The V and V' boards with wire orientation of -60 degrees relative to the X-plane are produced by a rotation of the U and U' boards of 180 degrees into the page about a vertical axis through the center of the board. Each half chamber has three planes with the first half consisting of (U, U', X) and the second half consisting of (X', V', V). The first chamber is oriented in the SHMS frame such that the board ordering as seen by particle traversing the spectrometer is (U, U', X, X', V', V), while for the second chamber the ordering is reversed (V, V', X', X, U', U). A drawing showing the chambers mounted in the frame is presented in Figure 30.

889 The drift gas (50/50 mixture of Ethane/Argon in production mode) flows across each board through holes in the cathode planes (k-planes) alternating from top to bottom. A technical drawing of a k-plane is presented in Figure 29. The overall dimensions of the wire chambers are driven by the desired active area for particles at the focal plane of the SHMS; this has been set at 80 cm x 80 cm. The active area of each wire plane consists of alternating $20\ \mu\text{m}$ diameter gold tungsten sense wires and $80\ \mu\text{m}$ diameter copper plated beryllium field wires separated by 0.5 cm. Each wire plane is sandwiched between a pair of cathode planes with the cathode surfaces consisting of 5 mil thick stretched foils of copper plated Kapton.

897 3.6. Heavy-Gas Cherenkov Counter

898 [Heavy-Gas Cherenkov Counter section.](#) [Author Organizer: G. Huber, w/R. Ambrose, with revisions by Stephen Kay and Vijay Kumar.](#)

901 3.6.1. Design

902 The SHMS Heavy-Gas Cherenkov detector (HGC) is a threshold-type Cherenkov detector, designed to separate charged π and K over most of the SHMS operating momentum range, 3–11 GeV/c. C_4F_{10} radiator gas at 1 atm, with an index of refraction of $n=1.00143$ at standard temperature [14], allow π^\pm to produce abundant Cherenkov light above 3 GeV/c momentum, while K^\pm remain below Cherenkov threshold until about 7 GeV/c. Optimal π/K separation at higher momenta require

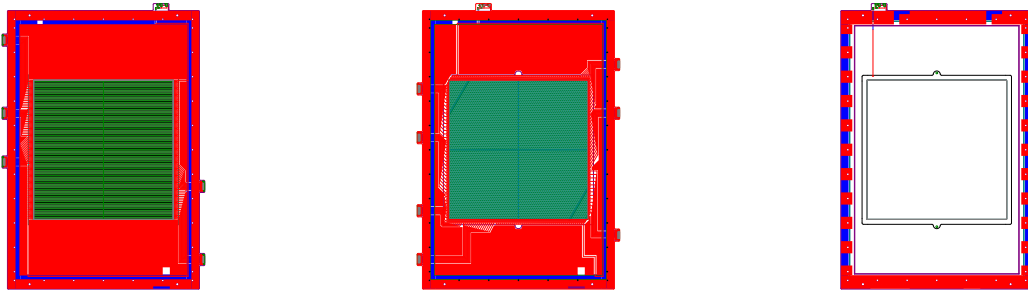


Figure 29: Technical drawings of the PCBs for the X-plane (Left), U-plane (Middle), and K-plan (Right).

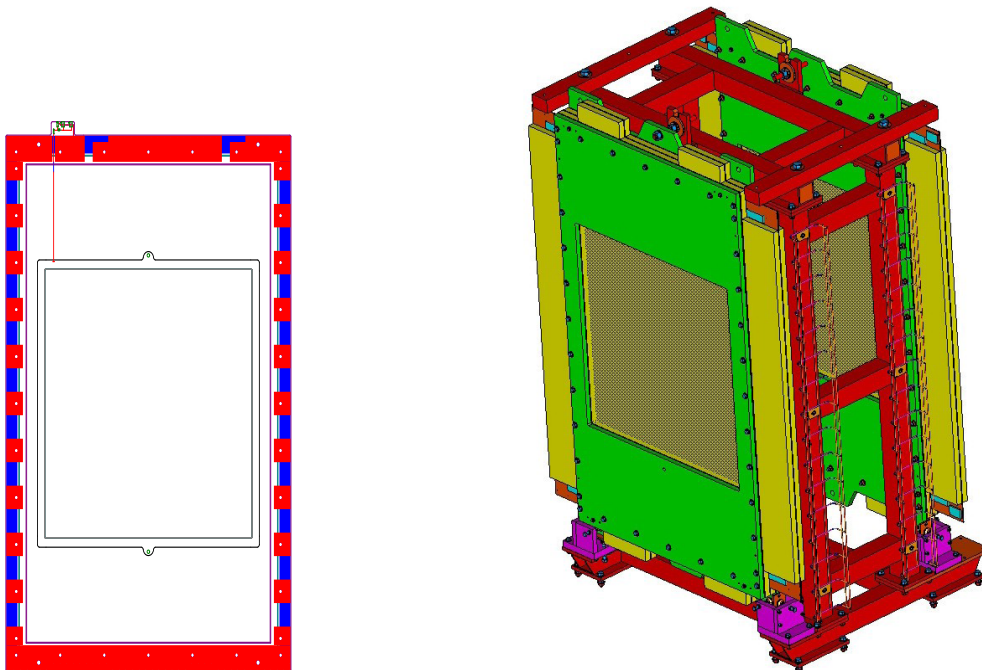


Figure 30: (Left) Technical drawing of cathode (k-plane) PCB. (Right) Technical drawing of the two drift chambers mounted in the Aluminum frame such that the scattered particles would enter the chamber from the left. The chambers are fixed to the frame by a bolt through the top tab on the chamber plate which allows for fine adjustments to the pitch. The downstream chamber (DC2) is mounted in the reverse orientation from the upstream chamber (DC1).

911 a reduction in the gas pressure, down to 0.3 atm at
 912 11 GeV/c.

913 A schematic view of the detector is shown in Fig. 31.
 914 The SHMS focal plane is subtended by four 55×60 cm
 915 0.3 cm thick glass mirrors, which reflect the Cherenkov
 916 radiation to four Hamamatsu R1584 12.5 cm photomul-
 917 tiplier tubes located above and below the particle en-
 918 velope. The mirrors and gas are enclosed in a cylind-
 919 rical aluminum tank of 164.9 cm inner diameter and
 920 113.5 cm length, with entrance and exit windows of
 921 0.102 cm thickness 2024 T-4 aluminum alloy [15]. The

922 vessel is sufficiently strong to be pumped to vacuum be-
 923 fore introducing the radiator gas, avoiding the need to
 924 purge when filling. A unique aspect of the detector is
 925 the placement of the photomultipliers outside the gas
 926 envelope, viewing the enclosure through 1.00 cm thick
 927 Corning 7980 quartz windows. This allows the gas en-
 928 closure to be smaller in diameter than otherwise, as the
 929 full length of the PMT and base no longer had to be
 930 fully within the diameter of the vessel. It also makes the
 931 PMTs available for servicing without venting the gas.

932 The mirrors are inexpensive, having been produced

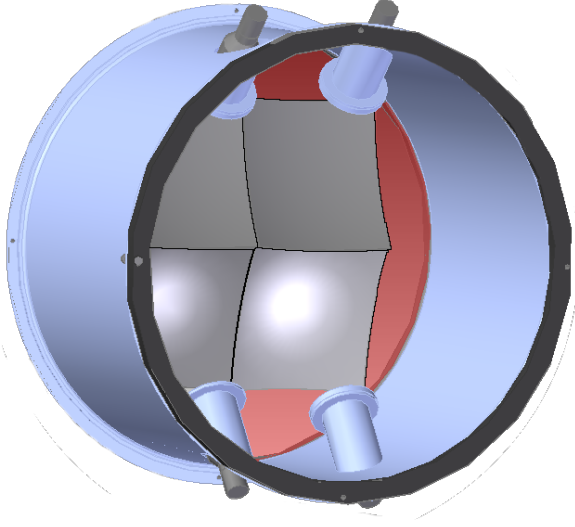


Figure 31: 3D-CAD rendering of the Heavy Gas Cherenkov Detector.

933 by the slumping process [16]. As a result, they deviate
 934 from the desired 110 cm radius of curvature with
 935 a slightly oblate shape [17]. However, the Cherenkov
 936 cone on the mirrors for 3-7 GeV/c π^\pm in C_4F_{10} is 7-
 937 10 cm in diameter, so optical quality mirrors are not
 938 required for this application. The UV wavelength char-
 939 acteristics of the respective optical components are rel-
 940 atively well matched. C_4F_{10} has good transmittance
 941 down to ~ 160 nm [14]. The quartz viewing windows
 942 provide $>88\%$ transmission down to 200 nm, including
 943 the $\sim 10\%$ loss due to surface reflection [18], and the op-
 944 tical glass face PMTs have 70% of their peak quantum
 945 efficiency at 200 nm (peak at 350 nm) [19]. Accord-
 946 ingly, the mirror reflectivity was optimized for $>90\%$ at
 947 270 nm, and 75% at 200 nm [20].

948 3.6.2. Calibration

949 The goal of the calibration procedure is to generate
 950 an accurate translation from raw FADC channels (or
 951 or charge in pC) to the number of photoelectrons (NPE),
 952 i.e. the number of electrons emitted from the cathode
 953 surface of the PMT. This is achieved by isolating the
 954 single photoelectron (SPE) peak, yielding a calibration,
 955 and then verified by examining the linear spacing of the
 956 first few photoelectrons.

957 To isolate the SPE peak, tracking cuts are applied
 958 to the data to analyze what each PMT detected from
 959 charged particles traversing each mirror quadrant. As a
 960 charged particle passes through a mirror quadrant, the
 961 produced Cherenkov cone allows some light to be inci-

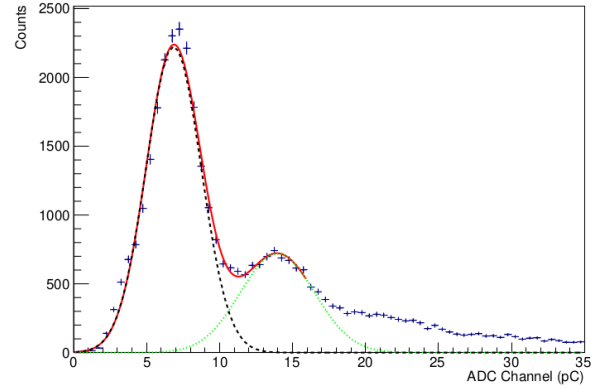


Figure 32: The isolated 1 (dashed black) and 2 (dotted green) photoelectron peaks for the lower right PMT #2, and their sum (solid red), obtained by selecting adjacent mirror light from the upper right quadrant #4. Three such adjacent mirror plots are obtained for each PMT. The light from the mirror closest to the PMT is far more intense, with too few SPE events available to yield a reliable calibration.

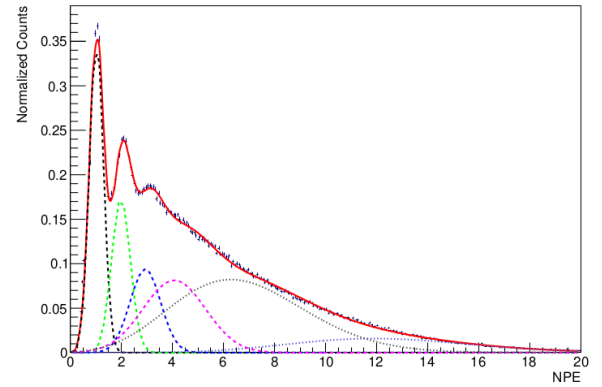


Figure 33: Results from a successful calibration of the HGC. Shown is the NPE distribution of the lower right PMT #2 obtained from all four mirrors. The 1, 2, 3 NPE peaks are shown, indicated by dashed Gaussian distributions. Two Poisson distributions (dotted lines) provide a good description of the nearest mirror events with large NPE, and a broad Gaussian near 4 NPE fills in the gap with the lower NPE peaks. The sum of all 6 distributions is shown as the solid red curve.

962 dent on adjacent mirrors. As each mirror is focused on
 963 a single PMT, one PMT will receive most of the pro-
 964 duced light while the other three receive much smaller
 965 amounts. This small signal allows the SPE peak to be
 966 measured, yielding a reliable calibration. To select this
 967 adjacent mirror light, cuts (based on the physical dimen-
 968 sions of the mirrors) are placed on the tracked coordi-
 969 nates of the charged particles, extrapolated to the HGC
 970 mirror plane,

$$x_{\text{HGC}} = x_{\text{Focal Plane}} + x'_{\text{Focal Plane}} \cdot z_{\text{HGC}} \quad (3)$$

$$y_{\text{HGC}} = y_{\text{Focal Plane}} + y'_{\text{Focal Plane}} \cdot z_{\text{HGC}}, \quad (4)$$

971 where $z_{\text{HGC}} = 156.27$ cm is the distance from the fo-
 972 cal plane to the HGC mirror plane. The coordinate axis
 973 for the HGC is the convention used in charged particle
 974 transport in dispersive magnetic systems. The x -axis is
 975 the direction of increasing particle momentum, the z -
 976 axis is the direction of particle travel through the spec-
 977 trometer, and the y -axis is deduced from $z \times x$. Addi-
 978 tionally, timing cuts are applied to the HGC data, col-
 979 lected using the high resolution pulse time setting in the
 980 FADC250's FPGA. The time measured corresponds to
 981 the time it takes a pulse to reach half of its maximum
 982 amplitude after passing a pedestal threshold of 5 mV.
 983 Lastly, a cut on particle velocity, β , is also applied, ob-
 984 tained from the tracking algorithm.

985 An example of a completed calibration is shown in
 986 Figs. 32, 33. For this run, the HGC was filled with 1022
 987 C_4F_{10} at 1 atm, and the SHMS central momentum 1023
 988 was 2.583 GeV/c, with polarity set to detect positively- 1024
 989 charged particles. Cherenkov radiation is produced by 1025
 990 π^+ traversing the HGC with momentum > 2.598 GeV/c. 1026
 991 This can occur only for $\delta > +0.5\%$, which corresponds 1027
 992 roughly to the bottom half of the HGC. Subthreshold π^+ 1028
 993 with $\delta < +0.5\%$, as well as K^+ and p , may produce low- 1029
 994 level light in the HGC via knock-on electron emission and 1030
 995 scintillation in the radiator gas. The adjacent mir- 1031
 996 ror cuts described above produce a clear SPE peak in 1032
 997 Fig. 32, which provides the main source of calibration 1033
 998 information. A histogram of light collected in one PMT 1034
 999 from all four mirrors is shown in Fig. 33, where the av- 1035
 1000 erage number of photo electrons detected per event is 1036
 1001 higher due to the more intense light from the closest 1037
 1002 mirror. In this figure, the spectrum is fit with a sum of 1038
 1003 four Gaussian and two Poisson distributions, shown by 1039
 1004 the solid red line. 1040

1005 An inherent systematic uncertainty is present in the 1038
 1006 HGC calibration due to statistical errors in determining 1039
 1007 the location of the SPE peak in the various mirror quad- 1040
 1008 rants. This uncertainty was quantified by recording the 1041
 1009 locations of the SPE across several runs, for the different 1042
 1010 adjacent mirror combinations for each PMT, as well as 1043
 1011 by varying the contribution of the higher PE tail extend- 1044
 1012 ing underneath the SPE peak, as in Figs. 32, 33. The
 1013 systematic uncertainty in the calibration is taken to be
 1014 the root mean square of this set of values, giving $\pm 1.5\%$.
 1015 It should be noted this uncertainty is somewhat larger
 1016 than the statistical uncertainty of the SPE peak, which
 1017 is typically 0.2 to 0.6%.

1018 3.6.3. Gain Matching

1019 To ensure each PMT has an identical response to inci-
 1020 dent light, the voltages of each PMT were adjusted
 1021 to obtain accurate gain matching. This can be seen

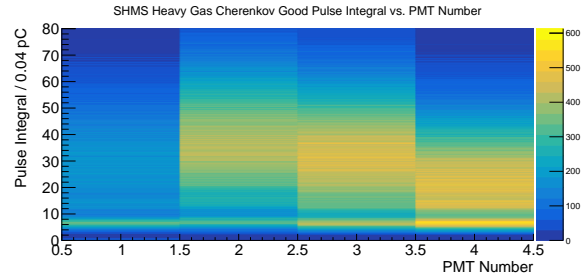


Figure 34: Demonstration of gain matching between PMTs by the alignment of the single photoelectron, indicated by the yellow band about 6.825 pC. The horizontal axis refers to PMT number, the vertical axis to Pulse Integral in bins of 0.04 pC. The color axis represents the number of events filling each bin.

in Figure 34 by the alignment of the SPE at approx-
 imately 6.825 pC, represented by the band across all
 four PMTs. Additionally, the gain of each PMT was
 tested by the manufacturer, Hamamatsu, and at Jeffer-
 son Lab. The results of each test are shown in Table 3.
 The Hamamatsu data were taken directly at 2000 V in
 a highly controlled environment, thus leading to small
 uncertainty in the gain which was not quoted. The Jef-
 ferson Lab measurement were also taken at 2000 V, but
 taken in an experimental environment. This gives rise
 to an uncertainty in the JLab gain data on the order of
 1%, larger than the Hamamatsu data.

3.7. Noble-Gas Cherenkov Counter

Noble-Gas Cherenkov Counter section. Author Or-
 ganizer: D. Day

3.7.1. Design

Analyzing momenta up to 11 GeV/c at scattering an-
 gles from 5.5 to 40.0 degrees, the SHMS will reach
 kinematic regions in which the pion background rate
 dominates the scattered electron rate by more than
 1000:1. The suppression of these anticipated pion
 backgrounds while maintaining efficient identification
 of electrons is therefore one of the main duties of the

PMT	JLab Gain	Hamamatsu Gain
PMT 1	$(2.79 \pm 0.01) \times 10^7$	0.969×10^7
PMT 2	$(6.55 \pm 0.04) \times 10^7$	3.60×10^7
PMT 3	$(7.12 \pm 0.05) \times 10^7$	5.79×10^7
PMT 4	$(5.35 \pm 0.04) \times 10^7$	3.20×10^7

Table 3: Gain characteristics for the PMTs in the HGC. Two measurements were performed, one at Jefferson Lab in an experimental setting, and one by the manufacturer Hamamatsu. The set voltage for the gain measurements is 2000 V for each PMT.

1045 SHMS detector elements and the SHMS Noble Gas
 1046 Cherenkov Detector shoulders a large portion of this
 1047 particle identification burden. The design of the noble
 1048 gas threshold Cherenkov detector is such that it will
 1049 meet these twin goals of suppression and identification.
 1050 The main goal of the detector is to distinguish between
 1051 electrons and pions with momenta between 6 GeV and
 1052 11 GeV/c. Operating at 1 ATM it will use a mixture
 1053 of Argon and Neon as the radiator: pure Argon with an
 1054 index of refraction $n=1.00028201$ at a SHMS momenta
 1055 of 6 GeV/c and pure Neon with an index of refraction
 1056 $n=1.000066102$ at 11 GeV/c and a mixture of Argon
 1057 and Neon at intermediate momenta.

1058 The SHMS NGC design was restricted by the avail-
 1059 able space and the need to have good discrimination at
 1060 the highest momenta. The number of photoelectrons is
 1061 maximized in this design by the use of quartz window
 1062 PMTs and mirrors with excellent reflectivity well into
 1063 the UV.

1064 The NGC consists of the XX main elements: 1) a
 1065 light tight box with thin entrance and exit windows de-
 1066 signed to operate at 1 Atm, 2) four spherical mirrors
 1067 held in a rigid frame, and 3) four 5 inch quartz window
 1068 photomultipliers (PMTs) and 5) the radiator gas.

1069 The tank was fabricated with an internal rigid alu-
 1070 minium t-slot frame and thin aluminum walls welded to-
 1071 gether and has an active length of 2m along the beam
 1072 direction and approximately 90 cm perpendicular to the
 1073 beam direction. The main access is provided through a
 1074 large 'door' and four small panels provide modest ac-
 1075 cess to the PMTs. The tank has feedthroughs for gas
 1076 management as well as for HV and signal cables. The
 1077 interior was painted with a black flat paint to prevent the
 1078 reflection of light from cosmic rays or hall background.
 1079 Thin entrance and exit window made of two layers of
 1080 2 mils of the Dupont product, Tedlar - $(\text{CH}_2\text{CHCl})_n$.
 1081 The PMTs were positioned outside the active area of the
 1082 scattered particles, achieved by a 15° tilt of the mirrors.

1083 Four spherical thin glass mirrors of radius 135
 1084 cm, square in shape with edges of 43 cm focus the
 1085 Cherenkov light onto to the PMTs. The glass blanks
 1086 were manufactured by Rayotek Scientific[24] of San
 1087 Diego from borosilicate glass of 3 mm thickness by
 1088 slumping over a polished steel mold and then cut to di-
 1089 mensions. As simulation showed a reduction of collec-
 1090 tion efficiency due to incoming photons losses at the ex-
 1091 posed edges of the mirror were beveled by away from
 1092 the active surface to minimize scattering from these
 1093 edges.

1094 The final batch of the glass blanks was shipped to
 1095 Apex Metrology Solutions of Fort Wayne for the CMM
 1096 shape scanning measurements. Apex's measurements

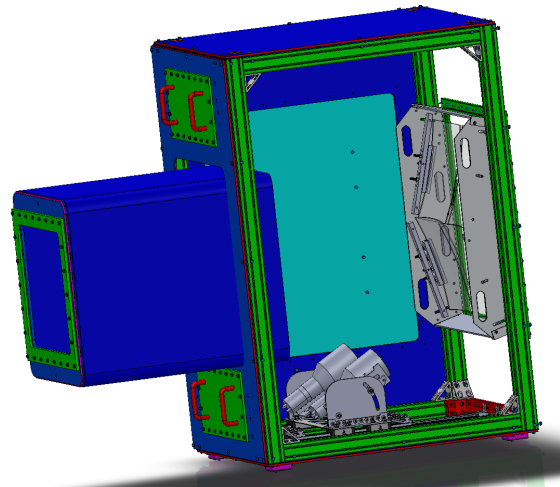


Figure 35: Sketch of the NGC tank. This view is possible as one panel is removed. Note the PMT mounting system is different than shown here.

were performed on the grid of 1806 points. The data were fitted with spherical, conical and elliptical fit functions for each mirror. Though the elliptical fit described the surface slightly better than the spherical fit the updated simulation with the real measured parameters showed almost no difference in the collection efficiency between the two. In addition the same fitting was performed for 5 selected locations on the mirror: entire mirror, the center, and 4 quadrants. Based on the spherical fit results "best" mirrors and "best" corners for each mirror were identified. The 4 mirrors come together and overlap at the center of the acceptance where a majority of the scattered electrons are focused. Care was then made to select among the best 4 glass pieces their best corners so as to be in the overlap region. The radii of the 4 best pieces of glass, from fitting, was found to never vary by more than 2 cm from the contracted value of 135 cm in fit areas described above.

Specially constructed packaging was constructed that made contact with the active surface all but impossible for shipment (and return) to CERN where they were coated by the Thin Film and Glass Service of the Detector Technologies Group at CERN[25]. The reflectivity was measured at CERN and found to be excellent well into the UV - See Figure 36

The four mirrors are arranged two above two arranged to overlap in the center, providing full coverage of the active area. In order to accomplish this the mirrors were order at slightly different z-positions (beam direction). The mirrors were mounted in a monolithic

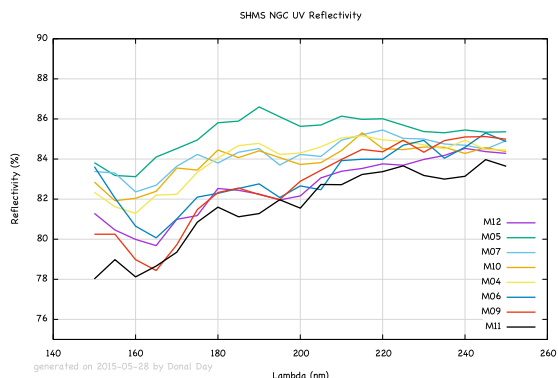


Figure 36: The UV measured reflectivity of the finished mirrors, coated at CERN which is no less than 78% at 150 nm. Between 250 nm and 600 nm the reflectivity rises to almost 90%.

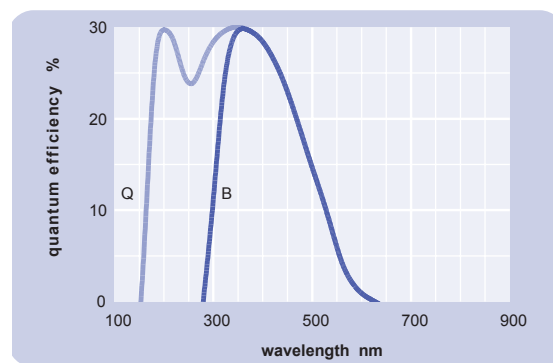


Figure 38: Quantum efficiency of Electron Tubes Enterprises model 9823QKB04 - light blue curve, labeled "Q".

1127 frame installed as single unit. See Figure 37 The mir-
 1128 rrors are tilted by 15° to allow the PMTs to be outside
 1129 the active area.



Figure 37: Frame with mirrors about to be moved into tank.

1130 The four PMTs are 14 stage 5 inch quartz win-
 1131 dows PMTs manufactured by Electron Tubes Enterprises
 1132 [26], model 9823QKB04. The tubes are surrounded by
 1133 a mu-metal shield and the HV is distributed to the stages
 1134 by a positive base. The 9823QKB04 has a quantum effi-
 1135 ciency above 5% at 150 nm and 30% at 350 nm as seen
 1136 in Figure 38.

1137 3.7.2. Optics Tuning

1138 3.7.3. Calibration

1139 3.7.4. Gain Matching

1140 3.7.5. Performance

1141 3.8. Aerogel Cherenkov Counter

1142 Aerogel Cherenkov Counter section. Author Orga-
 1143 nizer: T. Horn

1144 Comprehensive article published in NIM A842
 1145 (2017) 28-47. [13].

1146 3.8.1. General Design Overview

1147 The detector design is summarized in Fig. 39 which
 1148 shows a photograph of the aerogel counter installed
 1149 downstream of the cylindrical HGC in the SHMS de-
 1150 tector stack. The detector consists of two main com-
 1151 ponents: a tray which holds the aerogel material, and a
 1152 light diffusion box with photomultiplier tubes (PMTs)
 1153 for light readout. Four identical trays for aerogel of
 1154 nominal refractive indices of 1.030, 1.020, 1.015 and
 1155 1.011 were constructed. The design allows for easy de-
 1156 tector assembly and replacement of the aerogel trays.
 1157 Using up to 9 cm aerogel thickness in the trays, the total
 1158 depth of the detector is 24.5 cm along the optical axis of
 1159 the SHMS. A detailed discussion of the detector, char-
 1160 acterization of its components, and performance tests
 1161 can be found in Ref. [36].

1162 The diffusion box is made of the aluminum alloy
 1163 6061-T6. The side panels are constructed of ~2.5 cm
 1164 (1-inch) plates. The back cover is ~1.6 mm (1/16 inch)
 1165 thick. The inner dimensions of the box are ~ 103 ×
 1166 113 × 17.3 cm³ (40.5" × 44.5" × 6.82"). To optimize
 1167 light collection the inner surface of the diffusion box is
 1168 lined with either 3 mm (covering ~60% of the surface)
 1169 or 1 mm (remaining ~40% of the surface) thick GORE

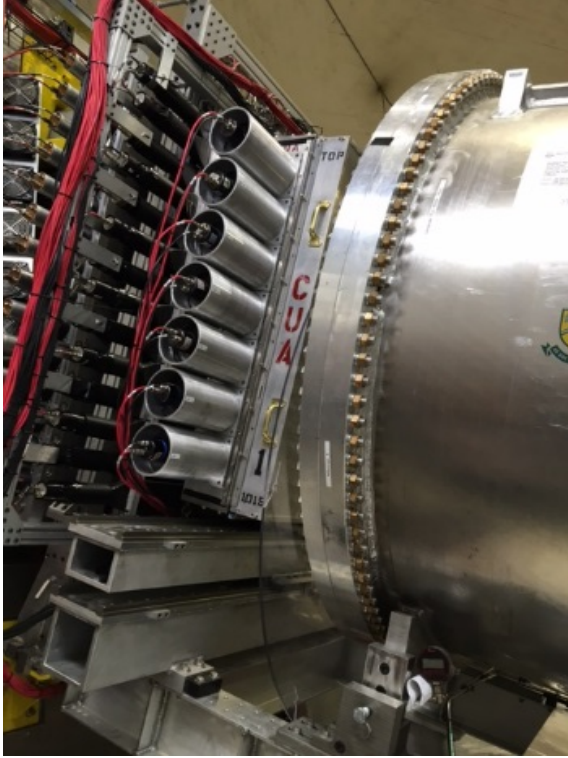


Figure 39: Photograph of the aerogel Cherenkov detector (“CUA” printed on the side of the radiator tray) installed in the SHMS detector stack. To its right is the Heavy Gas Cherenkov. On the left can be seen the edge of the S2XY hodoscope.

Table 4: Threshold momenta P_{Th} for Cherenkov radiation for charged muons, pions, kaons, and protons in aerogel of four refractive indices ranging from $n=1.011$ to 1.030 .

Particle	P_{Th} $n=1.030$	P_{Th} $n=1.020$	P_{Th} $n=1.015$	P_{Th} $n=1.011$
μ	0.428	0.526	0.608	0.711
π	0.565	0.692	0.803	0.935
K	2.000	2.453	2.840	3.315
p	3.802	4.667	5.379	6.307

the diffusion box but 11.3 cm (4.45”) deep. The front cover of the trays is made of a 5 mm thick honeycomb panel with effective Aluminum thickness to ~ 1.3 mm (0.050”). The inner surface of the SP-30 and SP-20 aerogel trays is covered with 0.45 μm thick Millipore paper Membrane GSWP-0010 (Millipore) of reflectivity of about 96% [38]. Though Millipore is difficult to handle, its chemical inertness makes it superior to reflective paints. For the two lower refractive index trays (SP-15 and SP-11), in order to optimize light collection, we used 1 mm thick Gore diffusive reflector material (DRP-1.0-12x30-PSA) with reflectivity of about 99%.

For the Cherenkov radiator high transparency aerogels were used. The higher two of the refractive indices (SP-30 and SP-20) were originally manufactured by Matsushita Electric Works, Ltd. The lower two indices (SP-15 and SP-11) were manufactured by Japanese Fine Ceramics Center. These tiles have dimensions of approximately 11 cm by 11 cm by 1 cm. They feature a waterproof coating that make them hydrophobic [39, 40]. This removes the need for baking (which in fact would destroy the coating). Detailed studies of the aerogel characteristics are presented in Ref. [36].

The trays were filled with aerogel tiles layer by layer. In each layer the tiles were laid down flat and arranged in a brick pattern to minimize holes in the radiator. To fill gaps of less than the size of a full tile at the edges of the tray the aerogel material was cut using a diamond coated saw or razor depending on the refractive index of the material. The aerogel radiator is on average ~ 9 cm thick (8 layers). The SP-30, SP-20 and SP-15 aerogel trays were filled over their entire 110 cm x 100 cm area. The SP-11 aerogel tray radiator covers only the active area of 90 cm x 60 cm required by the experiments [41, 42, 60, 43, 59]. An inner frame has been designed to arrange the aerogel tiles inside the active area of this tray. The sides of this inner frame are made of carbon fiber square tubes. This assembly allows future X-Y repositioning of the inner frame inside the tray.

To protect the aerogel radiator from severe damage

reflector material [37]. This material has a reflectivity of about 99% over the entire spectrum.

The light collection is handled by 5-inch diameter photomultiplier tubes (XP4500). The 5.56” (14.1 cm) diameter cylindrical housings holding the PMTs are mounted upon 14 waterjet cut circular openings on the left and right (long) sides of the diffusion box, with minimum spacing of 14.92 cm (5.875”) between the centers. The PMTs are sealed into their housing using a light-tight synthetic rubber material (Momentive RTV103 Black Silicone Sealant) and the whole assembly is sealed light-tight. The mechanical design includes six openings on the top of the diffusion box, presently covered with blanks, that can be used to increase the signal output from the detector by about 30%, if needed.

The magnetic shielding for the PMTs consists of 13.5 cm (5.316”) diameter μ -metal cylinders, which were constructed to end abreast with the PMT window. The construction also features bucking coils that can be installed on the PMTs, if excessive residual magnetic fields appear to be present in the SHMS hut.

The aerogel trays are of the same transverse size as

1232 in case of accidental flipping over of a tray during installation, a net of thin stainless steel wires is installed
1233 in close proximity to the aerogel surface. This is a technique
1234 previously tested in aerogel detectors at JLab [44].
1235 The wires form an interweaving grid by running between
1236 stainless steel screws on the sides of the box. Small
1237 springs attached to the ends of wires provide necessary
1238 tension.

1239 An aerogel tray attaches to the diffusion box by means
1240 of bolting through flanges surrounding both boxes. A
1241 round O-ring running in a shallow groove along the
1242 diffusion box sides ensures a light tight connection. The
1243 entire detector is designed so that it can be removed
1244 from the sliding detector stand that positions the
1245 detector into the SHMS detector stack.

1247 3.8.2. Performance aspects

1248 The light collection performance of the detector was
1249 tested with cosmic rays and electron beam. The detector
1250 signal shows good uniformity along the vertical (Y) coordinate
1251 of the detector surface, but has a significant dependence
1252 in the horizontal (X) direction. Possible optimization
1253 of this include a variable threshold and an optimized
1254 selection of the PMTs installed on the right and left
1255 side of the detector. The response of the detector to
1256 particles is shown in Fig. 40.

1257 The mean number of photo-electrons in saturation for
1258 the tray filled with $n=1.030$ ($n=1.020$) refractive index
1259 aerogel is ~ 10 (~ 8) which is close to expectation
1260 from Monte Carlo simulation. For the trays filled with
1261 $n=1.015$ and $n=1.011$ refractive index aerogel, high
1262 numbers of photoelectrons were obtained with the use
1263 of higher reflectivity Gore material to cover the tray,
1264 ~ 10 and ~ 5.5 respectively. This result could be fully
1265 reproduced by our Monte Carlo simulation by also assuming
1266 the aerogel absorption length on the order of 220 cm.

1268 3.8.3. Results from tests with beam

1269 The performance of the detector was tested with beam
1270 in Hall C. The detector signal showed good uniformity
1271 along the vertical direction, but significant dependence
1272 in the horizontal direction. Possible optimizations to
1273 address this are discussed below. The mean number
1274 of photoelectrons in saturation for a tray filled with
1275 $n=1.030$ refractive index aerogel is 12 photoelectrons
1276 and 10 for the tray filled with $n=1.015$ refractive
1277 index aerogel (see Fig. 40).

1278 3.8.4. Optimizations

1279 Possible optimizations include a variable threshold
1280 and optimized selection of PMTs. Lower refractive in-

1281 dex and highly transparent aerogel like that currently
1282 under investigation by Aspen Aerogel, Inc. may allow
1283 to provide kaon proton distinction at even higher particle
1284 momenta.

1285 3.9. Preshower and Shower Counters

1286 Shower/Preshower Counter section. Author Organizer:
1287 H. Mkrtchyan, V. Tadevosyan
1288 *DRAFT-VI*

1288 3.9.1. Preface

1289 In its basic configuration the SHMS detection stack
1290 includes a heavy gas Cherenkov for hadron selection,
1291 and a noble-gas Cherenkov and lead-glass electromagnetic
1292 calorimeter for electron/hadron separation. The detector
1293 stack is augmented by aerogel Cherenkov detectors,
1294 primarily for kaon identification. The approved
1295 experiments demand a suppression of pion background
1296 for electron/hadron separation of 1,000:1, with
1297 suppression in the electromagnetic calorimeter alone on
1298 the level of 100:1. An experiment to measure the pion
1299 form factor at the highest Q^2 accessible at JLab with
1300 11 GeV beam requires a strong suppression of electrons
1301 against negative pions of a few 1,000:1, with a
1302 requirement on the electromagnetic calorimeter of a
1303 200:1 suppression.

1304 Particle detection using electromagnetic calorimeters
1305 is based on the production of electromagnetic showers
1306 in a material. The total amount of the light radiated
1307 in this case is proportional to the energy deposited by
1308 the primary particle in the medium. Electrons (as well
1309 as positrons and photons), will deposit their entire
1310 energy in the calorimeter giving the ratio of energy
1311 detected in the calorimeter to particle energy (energy
1312 fraction) of one.

1313 Charged hadrons entering a calorimeter have a low
1314 probability to interact and produce a shower, and may
1315 pass through without interaction. In this case they
1316 will deposit a constant amount of energy in the
1317 calorimeter. However, they may undergo nuclear
1318 interactions in the radiator (in our case lead-glass)
1319 and produce particle showers similar to the electron
1320 and positron induced particle showers. Hadrons that
1321 interact inelastically near the front surface of the
1322 calorimeter and transfer a sufficiently large fraction
1323 of their energy to neutral pions will mimic electrons.
1324 The maximum attainable electron/hadron rejection
1325 factor is limited mainly by the cross section of such
1326 interactions.

1327 In this section we describe details of construction
1328 of the SHMS calorimeter. We present results of
1329 pre-assembly component checkout, and performance
1330 from experimental studies.

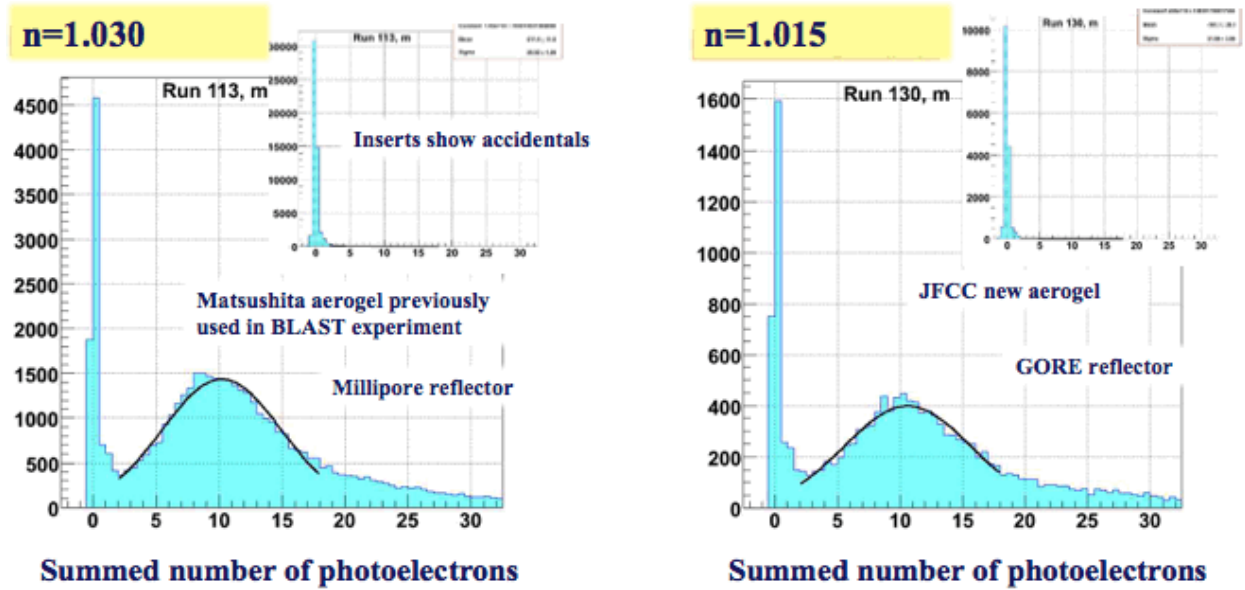


Figure 40: Numbers of photoelectrons observed in the Aerogel Cherenkov.

3.9.2. Construction

As a full absorption detector, the SHMS calorimeter is situated at the very end of detector stack of the spectrometer [45]. The relatively large beam envelope of the SHMS dictated a design of a wide acceptance coverage. The general requirements for the SHMS calorimeter were:

- Effective area: $\sim 120 \times 140 \text{ cm}^2$;
- Total thickness: $\sim 20 \text{ rad. length}$;
- Dynamic range: 1.0 - 11.0 GeV/c;
- Energy resolution: $\sim 6\% / \sqrt{E}$, E in GeV;
- Pion rejection: $\sim 100:1$ at $P \gtrsim 1.5\text{-}2.0 \text{ GeV}/c$;
- Electron detection efficiency: $> 98\%$.

A few different versions of calorimeter assembly for the SHMS spectrometer have been considered ([45]) before it was optimized for cost/performance.

A possible choice was a construction similar to the HMS calorimeter, with radiator from transversely oriented lead glass blocks and Cherenkov light detection from the sides of detector. An alternative was a calorimeter similar to HERMES [47] and Hall A [48] shower counters.

For each version the energy resolution, electron detection efficiency and pion/electron separation capabilities were determined by simulations.

Our studies allowed selection of the optimum calorimeter geometry while maintaining the good energy resolution and pion rejection capabilities. The SHMS calorimeter consists of two parts (see Fig. 41): the main part at the rear (Shower), and Preshower before

the Shower to augment PID capability of the detector.

An optimal and cost-effective choice was found by using available modules from HERMES calorimeter for Shower part, and modules from the Hall C decommissioned SOS calorimeter for Preshower. With this choice the Shower became 18.2 radiation length deep and almost entirely absorbs showers from $\sim 10 \text{ GeV}$ electromagnetic projectiles, and Preshower became 3.6 radiation length thick.

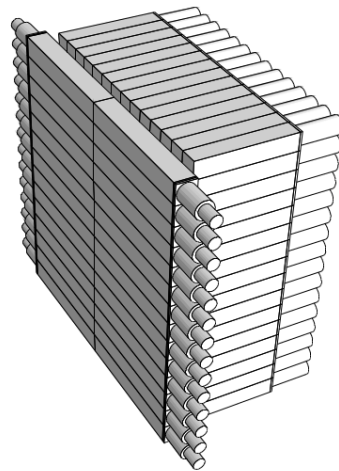


Figure 41: A sketch of SHMS calorimeter. Shown are Preshower (on the left) and Shower parts. Support structures are omitted.

The SHMS Preshower radiator consists of a layer of 28 TF-1 type lead glass blocks stacked in two columns

1370 in an aluminum enclosure (not shown in Fig. 41). 28
1371 PMT assemblies, one per block, are attached to the left 1422
1372 and right sides of the enclosure. The Shower part 1423
1373 consists of 224 F-101 type lead glass modules stacked in 1424
1374 a “fly eye” configuration of 14 columns and 16 rows. 1425
1375 All blocks of Preshower were produced in early 1985- 1426
1376 1990’s by a Russian factory in Lytkarino [49], whose 1427
1377 products of good optical quality were well known. \sim 1428
1378 $120 \times 130 \text{ cm}^2$ of effective area of detector covers the 1429
1379 beam envelope at the calorimeter. 1430

1380 The Preshower enclosure adds little to the material on 1431
1381 the pass of particles. On the front and back are 2” Hon- 1432
1382 eycomb plate and a 1 mm sheet of aluminum respec- 1433
1383 tively, which add up to 1.7% of radiation length only. 1434
1384 The optical insulation of the $10 \text{ cm} \times 10 \text{ cm} \times 70 \text{ cm}$ TF- 1435
1385 1 blocks in the Preshower is optimized to minimize the 1436
1386 dead material between them, without compromising the 1437
1387 light tightness. First, the blocks are loosely wrapped in a 1438
1388 single layer of $50 \mu\text{m}$ thick reflective aluminized Mylar 1439
1389 film, with Mylar layer facing the block surface. Then, 1440
1390 every other block is wrapped with a 10 cm wide strip 1441
1391 of $50 \mu\text{m}$ thick black Tedlar film, to cover its top, bot- 1442
1392 tom, left and right sides but the circular openings for the 1443
1393 PMT attachments. Looking at the face of detector, the 1444
1394 wrapped and unwrapped blocks are arranged in a chess 1445
1395 pattern. Insulation of the remaining front and back sides 1446
1396 of the blocks are provided by facing inner surfaces of the 1447
1397 front and rear plates of the enclosure, covered also with 1448
1398 Tedlar. In addition, a layer of Tedlar separates the left 1449
1399 and the right columns. 1450

1400 The PMT assembly tubes are screwed in $\varnothing 90 \text{ mm}$ cir- 1451
1401 cular openings on both sides of the enclosure. The spac- 1452
1402 ing of the openings matches the height of the blocks, 1453
1403 so that a PMT faces to each of the blocks. The 3” 1454
1404 XP3462B PMTs are optically coupled to the blocks us- 1455
1405 ing ND-703 type Bicon grease of refractive index 1.46. 1456

1406 The HERMES modules used in the Shower part are 1457
1407 similar in construction to the HMS but differ in details. 1458
1408 The radiator is an optically isolated $8.9 \times 8.9 \times 50 \text{ cm}^3$ 1459
1409 block of F-101 lead-glass, which is similar to TF-1 in 1460
1410 physical parameters. The typical density of F-101 type 1461
1411 lead-glass is 3.86 g/cm^3 , radiation length 2.78 cm, and 1462
1412 refraction index 1.65. 1463

1413 Results of TF-1 and F-101 type lead-glass blocks 1464
1414 transmittance measurements are presented in [45]. 1465

1415 Each F-101 block is coupled to a 3” XP3461 PMT 1466
1416 from Photonis, with green extended bialkali photocath- 1467
1417 ode, of the same sizes and internal structure as the 1468
1418 XP3462B in the Preshower. Typical quantum efficiency 1469
1419 of the photocathode is $\sim 30\%$ for $\lambda \sim 400 \text{ nm}$ light, and 1470
1420 the gain is $\sim 10^6$ at $\sim 1500 \text{ V}$. Silgard-184 silicone glue
1421 of refractive index 1.41 is used for optical coupling of

the PMTs to lead-glass blocks.

A μ -metal sheet of 1.5 mm thickness and two layers of Teflon foil are used for magnetic shielding and electrical insulation of the PMTs. The blocks are wrapped with $50 \mu\text{m}$ aluminized Mylar and $125 \mu\text{m}$ black Tedlar paper for optical insulation. A surrounding aluminum tube which houses the μ -metal, is fixed to a flange, which is glued to the surface of the lead-glass. The flange is made of titanium, which matches the thermal expansion coefficient of F-101 lead-glass [46].

Beyond simple repairs, no adjustment has been made to the original HERMES construction of the modules for re-use in the SHMS calorimeter.

As both the TF-1 and F-101 lead-glass blocks have been in use for more than 14 years under conditions of high luminosity, there was concern about possible radiation degradation of the blocks and the PMTs.

The changes in transparency of TF-1 and F-101 type lead-glass radiators have been studied. The estimated radiation dose for the used blocks was about 2 krad. For several samples of F-101 and TF-1 type blocks the light transmittance has been measured before and after 5 days of curing with UV light (of wavelength $\lambda=200\text{-}400 \text{ nm}$).

We did not find notable degradation in transmittance for the TF-1 type blocks taken from the SOS calorimeter and F-101 blocks taken from HERMES detector.

The gain and relative quantum efficiencies for randomly selected PMTs from the SOS calorimeter (XP3462B) and from the HERMES detector (XP3461) have been measured to check possible degradation effects in the PMTs. A $\sim 10\text{-}15\%$ systematic decrease in quantum efficiency was noticed.

3.9.3. Photomultiplier tube selection and studies

The SHMS Preshower inherited PMTs from the retired SOS calorimeter. The choice of XP3462B PMT for Hall C calorimeters was made in 1994 after studies of several other 3 inch and 3.5 inch photomultiplier tubes on the matter of having good linearity, photocathode uniformity, high quantum efficiency, and good timing properties. Gain variations with HV and dark currents also were measured [50]. For samples of PMTs the photocathode uniformity and effective diameter have been studied with a laser scanner. Following these tests, as a time and cost effective solution, a 3” diameter ($\approx 68 \text{ mm}$) semitransparent bi-alkaline photocathode, Photonis XP3462B PMTs were chosen for the equipment of the JLab Hall C calorimeters. These 8-stage PMTs have a linear focused cube dynode structure with a peak quantum efficiency (QE) of $\sim 29\%$ at 400 nm.

1471 *3.9.4. Studies on optical properties of TF-1 type lead* 1519
1472 *glass blocks* 1520

1473 With its index of refraction ~ 1.65 , radiation length 1521
1474 2.74 cm and density of 3.86 g/cm^3 TF-1 type lead glass 1522
1475 is well suited for serving as Cherenkov radiator in elec- 1523
1476 tromagnetic calorimeters. The fractional composition 1524
1477 consists primarily of PbO (51.2%), SiO₂ (41.3%), K₂O 1525
1478 (3.5%) and Na₂O (3.5%). 1526

1479 The light transmittance of TF-1 type lead-glass 1527
1480 blocks for the SHMS Preshower was checked in 2008 1528
1481 using a spectrophotometer from the JLab Detector 1529
1482 Group [51]. The wave-length was scanned from 200 nm 1530
1483 to 700 nm in steps of 10 nm. The blocks were oriented 1531
1484 transversely, and the light intensity passing through the 1532
1485 10 cm thickness was measured. The results were com- 1533
1486 pared with measurements from 1992, before assembling 1534
1487 of calorimeters for the Hall C HMS/SOS spectrometers. 1535
1488 Reliability of the measurements was checked by mea- 1536
1489 suring spared, unused blocks and comparing again with 1537
1490 1992 data. From comparison of 1992 and 2008 data, 1538
1491 signs of marginal degradation has been noticed. 1539

1492 *3.9.5. Choice and studies of PMT bases* 1542

1493 The Preshower PMT high voltage base design is opti- 1543
1494 mized for the requirements of good linearity (better than 1544
1495 1%), high rate capability and a weak variation of PMT 1545
1496 gain with anode current [50]. 1546

1497 A design, which is a purely resistive, high cur- 1547
1498 rent (2.3 mA at 1.5 kV), surface mounted divider 1548
1499 ($\sim 0.640 \text{ M}\Omega$), operating at negative HV is se- 1549
1500 lected. The relative fractions of the applied HV 1550
1501 between the dynodes (from cathode to anode) are: 1551
1502 3.12/1.50/1.25/1.25/1.50/1.75/2.00/2.75/2.75. The sup- 1552
1503 ply voltage for a gain of 10^6 is approximately 1750 V. 1553

1504 The PMT resistive base assembly is linear to within 1553
1505 $\sim 2\%$ up to the peak anode current of $120 \mu\text{A}$ ($\sim 5 \times 10^4$ 1554
1506 pe). The dark current is typically less than 3 nA. The 1555
1507 base has anode and dynode output signals. 1556

1508 *3.9.6. Monte Carlo simulations* 1558

1509 Prior to construction, the designed calorimeter setup 1560
1510 was computer simulated in order to possibly optimize 1561
1511 the setup and get predictions for key characteristics. 1562

1512 The simulations were based on the GEANT4 pack- 1563
1513 age [52], release 9.2. As in the simulations of the HMS 1564
1514 calorimeter (see [45]), the QGSP_BERT physics list was 1565
1515 chosen to model hadron interactions [53]. The code 1566
1516 closely followed the parameters of the detector compo- 1567
1517 nents. Other features are added into the model in order 1568
1518 to bring it closer to reality, such as: light attenuation 1569

length in the lead glasses and its block to block varia-
tion according to our measurements; PMT quantum ef-
ficiencies from the graphs provided by vendor, passive
material between the spectrometer focal plane and the
calorimeter; sampling of incoming particles at the focal
plane of the spectrometer. The Cherenkov light propa-
gation and detection was handled by a custom code,
in approximation of strict rectangular geometry of the
lead glass blocks with perfectly polished surfaces. Light
reflection and absorption by the Mylar wrapping was
modeled via Aluminum complex refractive index, with
Mylar support facing the block, and a thin air gap be-
tween the wrapping and the block. Both light passage
to the PMT photocathode through the optical grease
and the PMT window, and reflections from the block
sides were modeled in approximation of thin dielectric
layers ([54], p. 360). The electronic effects, such as
pedestal widths and channel to channel PMT gain vari-
ations were assumed as for the HMS calorimeter before
the 12 GeV modifications.

The simulations reveal no flaws in the design con-
struction of the SHMS calorimeter, and performance
similar to other lead glass based calorimeters. The stud-
ies indicated gain in pion suppression on the order of
several times from combining signal from Preshower
with total energy deposition in the calorimeter.

3.9.7. Cabling and electronics

The analog signals from the PMTs of the calorimeter
are digitized in the 16 channel JLab FADC250 modules,
located in the electronics hut adjacent to the SHMS de-
tector hut. The analog signals are transported to FADCs
via $\sim 30'$ long RG58 type cables laid down in a conduit
in the wall of the SHMS shield house. The digitized
signals are sent further to the Hall C counting house for
the input to the DAQ system via $??'$ long $??$ type multi-
fiber cables. The early digitization allows avoid noise
overlap during long distance signal transportation from
the experimental hall to the counting house.

During routine experimental data taking the FADCs
are operated in the Integral mode, when the pedestal
level is computed and subtracted from the pulse sig-
nal on event by event basis, and integrated in a pro-
grammable time window signal is provided. How-
ever, for the debugging purposes or for DAQ tuning the
FADCs can be operated in the Pulse mode. In this case
entire pulse samples are available for analysis.

Before being fed to FADCs, the analog signals from
the Preshower are split in 50:50 ratio for the purpose to
organize fractional sums of signals from the Preshower
modules for the trigger. The relatively short 30' cables
from the Preshower PMTs to the FADCs (compare to

1570 47' long cables from the hodoscope PMTs to the Hut
 1571 Patch Panel) allowed to compensate delay time when
 1572 forming the sums in the Linear FAN-IN/OUT Summing
 1573 Module. The SUM signals are set up as follows:

- 1574 1. Preshower Sum(1-4) = NEG(1-4) + POS(1-4)
- 1575 2. Preshower Sum(5-8) = NEG(5-8) + POS(5-8)
- 1576 3. Preshower Sum(9-12) = NEG(9-12) + POS(9-12)
- 1577 4. Preshower Sum(13-14) = NEG(13-14) + POS(13-
 1578 14)

1579 Here NEG and POS denote signals from right and left
 1580 sides of the Preshower. Combination of modules for
 1581 each sum can be changed if needed. These partial sum
 1582 signals are discriminated in a NIM discriminator and
 1583 sent to the Counting room via patch panel in the SHMS
 1584 hut and ~404' long (489.28 ns) RG8 type cables. In the
 1585 electronic room they are used to form Preshower Low
 1586 (PSh Lo) and Preshower High (PSh Hi) trigger signals.

1587 3.9.8. Calorimeter Gain Matching

1588 Gain matching of PMTs is important for uniformity
 1589 of performance of the calorimeter over the spectrome-
 1590 ter's acceptance. Minimum ionizing particles (m.i.p.'s)
 1591 were used for this purpose, for their signals from the
 1592 calorimeter nearly independent of particle's momentum.

1593 M.i.p. pion candidates for the Shower gain match-
 1594 ing were selected by requesting 4 PMT signals from the
 1595 Heavy Gas Cherenkov counter less than 2 p.e., and the
 1596 normalized deposited in the Preshower energies close to
 1597 the m.i.p. peak value, within range from 0.02 to 0.15.
 1598 In addition, the m.i.p. dominance in the Shower itself
 1599 was ensured by selecting single hit events, when only
 1600 one module was fired. The resultant m.i.p. peaks in
 1601 the ADC signal distributions were localized by Gaus-
 1602 sian fits (see Fig. 42).

1603 As gain matching had to be achieved by adjustment
 1604 of high voltages on the PMT bases, knowledge of gain
 1605 variations versus supplied HV's had been needed. That
 1606 was obtained by measuring signals from m.i.p. pions at
 1607 2 constant supply high voltages on all the Shower chan-
 1608 nels, at 1.4 kV and 1.5 kV (see Fig. 43). By assuming
 1609 gain dependence on supplied voltage in the form $\sim V^\alpha$
 1610 [19], the average exponent α was found to be $5.70 \pm$
 1611 0.01 for a set of ~100 channels.

1612 The gain matching was done in two ways. In the first
 1613 case, m.i.p. signals from pions were used. From the
 1614 reference run with supply voltages $A_{REF} = 1.4$ kV in
 1615 all the Shower channels, m.i.p. ADC signal amplitudes
 1616 $A_{REF}(i)$ were obtained as described above. For a desired
 1617 constant signal amplitude $A_{SET} = 1000$ ADC channels,
 1618 the set voltages $V_{SET}(i)$ were estimated via

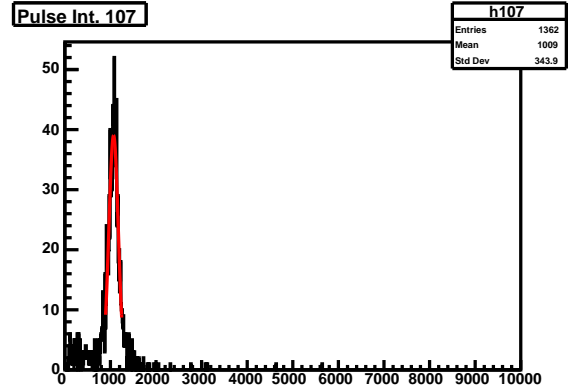


Figure 42: Distribution of ADC signals of a Shower module from minimum ionizing pions. The red line is a Gaussian fit to the m.i.p. peak.

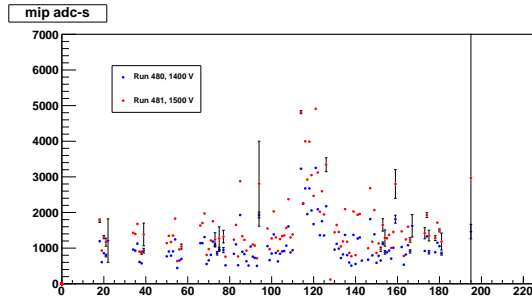


Figure 43: Amplitudes of ADC signals from m.i.p. pions in a set of Shower channels, for supply voltages of 1.4 kV and 1.5 kV.

$$1619 \quad V_{SET}(i) = V_{REF} \cdot \left(\frac{A_{SET}}{A_{REF}(i)} \right)^{1/\alpha} \quad (5)$$

1620 In the second case, data from run of electron detec-
 1621 tion in the SHMS were used. The SHMS optics was set
 1622 up at 3 GeV/c central momentum, in a defocused mode,
 1623 which allowed for hitting and calibration with electrons
 1624 of more than 150 Shower modules. For deposited en-
 1625 ergy E in a given module, signal amplitude A , PMT gain
 1626 g , calibration constant c the following holds: $A \sim g \cdot E$,
 1627 $E = c \cdot A$. Hence $g \sim V^\alpha \sim 1/c$, and for the chosen
 calibration constant c_{SET} one gets

$$1628 \quad V_{SET}(i) = V_{REF} \cdot \left(\frac{c_{SET}^{-1}}{c_{REF}^{-1}(i)} \right)^{1/\alpha} \quad (6)$$

The HV settings from the second method, for $c_{SET} =$
 35 MeV/ADC ch are within the range from 1.2 kV to
 1.6 kV and are grouped around 1.4 kV (Fig. 44). A few
 settings above hard limit of 1.7 kV were forced to the

1632 limit. The HV settings from the two methods are in correlation.
 1633
 1634 Note that out of acceptance hence not gain matched
 1635 channels were left at nominal 1.4 kV high voltages.
 1636 Note also that the chosen voltages are conservative, less
 1637 than HV settings at which modules had been operated
 1638 in the HERMES calorimeter.

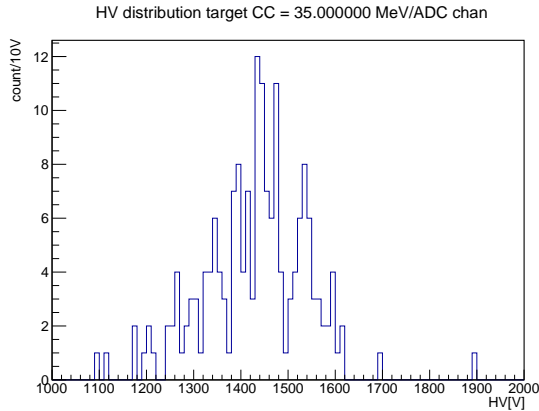


Figure 44: Gain matched high voltage settings for the Shower PMTs (see text for details).

1639 The amplitudes of ADC signals from m.i.p. pions after
 1640 the gain matching are shown in Fig. 45. The majority
 1641 of amplitudes are grouped between 20 and 30 ADC
 1642 channels. The spread in signals among hit channels is
 1643 much less than in the case of constant supply voltages
 1644 (compare with Fig. 43).

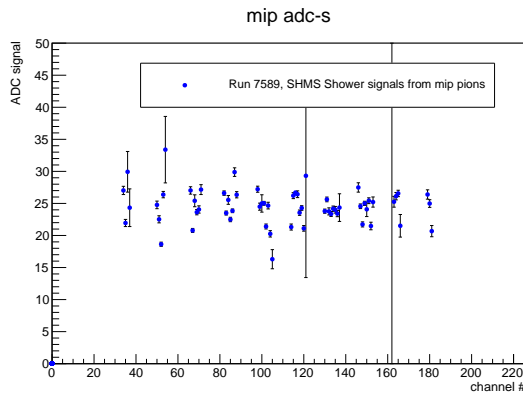


Figure 45: Amplitudes of ADC signals from m.i.p. pions in a set of Shower channels after gain matching.

1645 The Preshower detector was gain matched with cosmic
 1646 rays, prior to installation in the spectrometer. Coincidence
 1647 of signals from scintillator counters positioned above
 1648 and below the detector served as a trigger. The

1649 gain matching was adjusted after the installation, again
 1650 with cosmics but this time passing through the detector
 1651 stack. Muons were identified as events of single track
 1652 in the drift chambers and single hit module in the
 1653 Preshower. New set of voltages were calculated based
 1654 on m.i.p. peak positions and according to formula similar
 1655 to Eqns 5, 6. The voltages span range from 1.1 kV
 1656 to 1.7 kV. The quality of gain matching was insured by
 1657 taking cosmic data with the new HV settings (Fig. 46).

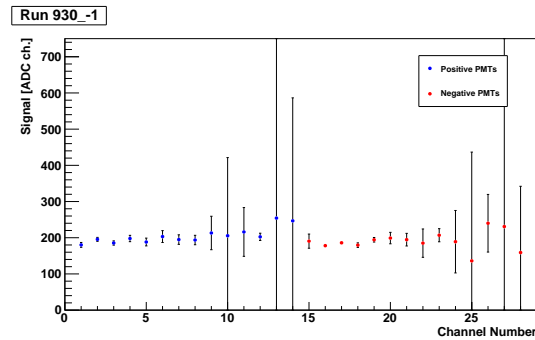


Figure 46: Amplitudes of ADC signals from cosmic muons in the Preshower channels after gain matching.

3.9.9. Calorimeter Calibration

To be updated. A representative plot from calibration to be added.

The ability of particle identification of a calorimeter is based on differences in the energy deposition from different types of projectiles. The deposited energy is obtained by converting the recorded ADC channel value of each module into equivalent energy.

The data analysis procedure corrects for the gain differences in the process of calorimeter calibration. Good electron events are selected by means of gas Cherenkov detector. The standard calibration algorithm [55] is based on minimization of the variance of the estimated energy with respect to the calibration constants, subject to the constraint that the estimate is unbiased (relative to the primary energy). The momentum of the primary electron is obtained from the tracking in the magnetic field of the spectrometer.

The deposited energy per channel is estimated by

$$e_i = c_i \times A_i, \quad (7)$$

where i is the channel number, c_i is the calibration constant, A_i is the FADC pulse integral signal. Note that the Preshower signals are corrected for the light attenuation dependence versus horizontal hit coordinate y .

In the calorimeter analysis code hits on adjacent blocks in the Preshower and in the Shower are grouped

1682 into clusters. For each cluster the deposited energy 1731
 1683 and center of gravity are calculated. These clusters 1732
 1684 are matched with tracks from the upstream detectors 1733
 1685 if the distance from the track to cluster is less than a 1734
 1686 predefined “slop” parameter (usually 7.5 cm). For the
 1687 Preshower the distance is calculated in the vertical direction.
 1688

1689 The calorimeter energy corresponding to a track is
 1690 divided by the track momentum and used for particle
 1691 identification. In the few GeV/c range pions and elec-
 1692 trons are well separated (see Fig. ??, **NEED FIGURE**),
 1693 a cut at 0.7 ensures an electron detection efficiency
 1694 ~99% and pion suppression of tens of times.

1695 3.9.10. Summary on the SHMS calorimeter

1696 Design, construction details and performance of the
 1697 electromagnetic calorimeter for the newly built SHMS
 1698 spectrometer in Hall C has been presented. From a few
 1699 considered versions, the Preshower+Shower configura-
 1700 tion was selected as most cost-effective. The Preshower
 1701 consists of a layer of 28 modules with TF-1 type lead
 1702 glass radiators, stacked back to back in two columns. 1735
 1703 The Shower part consists of 224 modules with F-101 1736
 1704 type lead glass radiators, stacked in a “fly eye” config- 1737
 1705 uration of 14 columns and 16 rows. $120 \times 130 \text{ cm}^2$ of 1738
 1706 active area covers beam envelope at the calorimeter. 1739

1707 The calorimeter was commissioned as part of the 1740
 1708 SHMS detector package in the fall of 2017, then used 1741
 1709 in the first 12 GeV Hall C experiments in 2018. The 1742
 1710 first calorimeter data show satisfactory performance of 1743
 1711 the detector. 1744

1712 4. Trigger and Data Acquisition

1713 [Trigger and DAQ section.](#) 1748
 1714 [Author/Organizer: B. Sawatzky](#) 1749

1715 The Hall C data acquisition (DAQ) system is de- 1750
 1716 signed to meet the needs of a high luminosity, dual 1751
 1717 spectrometer (SHMS + HMS) configuration, with the 1752
 1718 capability of extracting polarization-dependent absolute 1753
 1719 cross sections with precision at the 1% level or better. 1754
 1720 JLab’s CODA data acquisition software [65] provides 1755
 1721 a framework that ties together a distributed network of 1756
 1722 read-out controllers (ROCs) controlling multiple crates 1757
 1723 of digitization hardware, event builders to serialize the 1758
 1724 data, and event recorder processes to write the data to 1759
 1725 disk. It also provides a graphical control interface for 1760
 1726 the users. 1761

1727 The Hall C DAQ system can run in dual-arm trigger 1762
 1728 mode that requires a coincidence between both spec- 1763
 1729 trometers, or each arm’s DAQ may be run entirely inde- 1764
 1730 pendently of the other. Incorporating additional detector 1765

systems into the standard two-arm design is also straight
 forward. A high-level block diagram of trigger forma-
 tion and readout for each spectrometer arm (SHMS or
 HMS) is depicted in (Fig. 47).

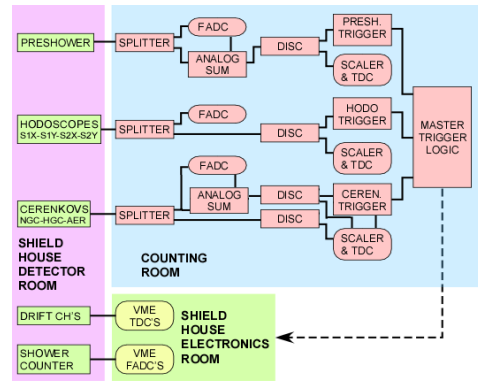


Figure 47: Block diagram of high-level trigger formation for SHMS (and HMS). See Section 4.1 for details.

The hardware DAQ and trigger designs were strongly influenced by the preceding 6 GeV HMS and SOS configurations. This choice was made to provide a careful and systematic migration from the very well understood systematics of the 6 GeV system while incorporating and characterizing a new generation of FPGA-based logic and readout electronics. To this end, the present system relies on a combination of *legacy* NIM and CAMAC discriminators and logic modules to form readout triggers, but utilizes a full set of modern high speed payload and front-end modules to allow a transition to a firmware based trigger and fully pipelined readout in the future.

In the present configuration, the DAQ has a nominal maximum trigger accept rate of 4 kHz with a dead-time of $\approx 20\%$. Dead times are measured using the Electronic Dead Time Measurement system outlined in Section 4.2. The underlying hardware supports running in a fully pipelined mode, and should be capable of running at trigger rates exceeding 20 kHz with minimal dead-time using firmware based triggers similar to those employed in Halls B and D. This capability was not part of the initial 12 GeV upgrade plan for Hall C, but may be pursued in the future (Sect. 4.5).

Signals from the scintillator planes, Cherenkov detectors, and Calorimeter detectors in the SHMS and HMS detector stacks are processed to form *pre-triggers*. Those pre-triggers can serve as *event triggers* themselves (that initiate a recorded event), or be combined to bias data collection towards particular particle types (*i.e.* electrons *vs.* pion) and suppress backgrounds. Each

1766 running DAQ can be fed up to six independent triggers 1815
 1767 simultaneously and the Experimenter can control what 1816
 1768 fraction of each is recorded to disk run-by-run through 1817
 1769 an integrated pre-scale feature. 1818

1770 4.1. Standard Triggers

1771 All trigger-related PMT signals from both the SHMS 1821
 1772 and HMS are routed out of the experimental Hall to a 1822
 1773 dedicated electronics room on the main level of the Hall 1823
 1774 C Counting House using low-loss RG-8 air-core signal 1824
 1775 cables. Those signals are then split with one copy run- 1825
 1776 ning into a JLab F250 flash analog to digital converter 1826
 1777 (FADC)[66], and the second copy is processed and dis-
 1778 criminated. All discriminated pulses are delivered to
 1779 scalers for rate information, TDCs for precision tim-
 1780 ing measurement, and to form pre-triggers as described
 1781 below. This design allows direct access to all raw sig-
 1782 nals that may participate in a trigger during beam oper-
 1783 ations and has proven invaluable during the debugging
 1784 and commissioning phases of Hall operations.

1785 Non-trigger related signals include wire-chamber 1827
 1786 readouts and the Shower (but not Pre-Shower) layer 1828
 1787 of the SHMS calorimeter. The readout electronics for 1829
 1788 those sub-detectors remain inside their respective de- 1830
 1789 tector huts within the experimental Hall. All SHMS 1831
 1790 Calorimeter PMT signals are fed into F250 FADCs con- 1832
 1791 figured to provide timing, integrated energy, pulse am- 1833
 1792 plitude, and (optionally) pulse profile data as desired. 1834
 1793 The wire-chamber signals are digitized using multi-hit 1835
 1794 CAEN v1190 modules [67]. 1836

1795 The CAEN v1190 payload module provide 128 inde- 1837
 1796 pendent multi-hit/multi-event TDC channels with a user 1838
 1797 configurable resolution ranging from $52\ \mu\text{s}$ — $100\ \text{ps}$ per 1839
 1798 bin. They provide a 32 kilo-word deep output buffer and 1840
 1799 can be readout asynchronously with respect to the event 1841
 1800 triggers. Typical Hall C operation has all units config- 1842
 1801 ured for 100 ps/bin. 1843

1802 4.1.1. JLab F250 Flash ADCs

1803 The JLab F250 flash ADC modules are an FPGA- 1839
 1804 based design developed by the Jefferson Lab Fast Elec- 1840
 1805 tronics group [66] and are used Lab wide. Each F250 1841
 1806 module provides 16 independent $50\ \Omega$ input channels. 1842
 1807 The voltage at each input channel is continuously dig- 1843
 1808 itized into an $8\ \mu\text{s}$ ring buffer at 250 MHz, with a res- 1844
 1809 olution of 12 bits, and a hardware adjustable full-scale 1845
 1810 range. When a modules receives a readout trigger, 1846
 1811 digitized sample data stored in the ring buffer is pro- 1847
 1812 cessed in a parallel process that does not incur front- 1848
 1813 end-deadtime. In typical operation each ‘hit’ over a 1849
 1814 pre-programmed threshold is assigned an interpolated 1850

leading-edge threshold time ($<1\ \text{ns}$ resolution), inte-
 grated energy (analogous to a charge-integrating ADC
 value), a peak-amplitude, and a measurement of any DC
 offset (pedestal) present on the channel prior to the de-
 tected pulse. Full pulse-profile data for each hit may
 also be stored if desired. However, that mode increases
 the data rate by several orders of magnitude, and is gen-
 erally used only for debugging or limited duration pulse
 characterization runs.

4.1.2. SHMS Triggers

The SHMS detector stack layout is described in Sec-
 tion 3.2. A representative detector layout is presented in
 Figure 48.

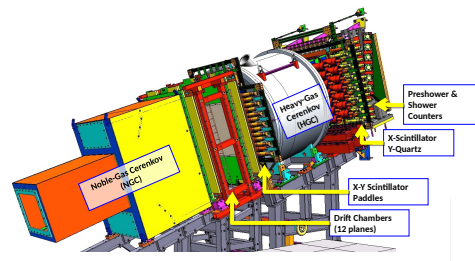


Figure 48: Typical detector layout for the SHMS.

Each hodoscope plane described in Sections 3.3 and
 3.4 is constructed from an array of horizontal (or verti-
 cal) bars with a PMT on each end. Signals from those
 PMTs are split and one analog copy is delivered to F250
 FADCs. The second analog copy is discriminated and
 sent to CAEN 1190 TDCs for precision timing infor-
 mation, to scalers for raw rate information, and to logic
 modules to provide the hodoscope pre-triggers plane by
 plane. A pre-trigger for each plane generated by OR’ing
 the discriminated signals from each side of a hodoscope
 plane together, then AND’ing the resulting two signals
 together. The pre-triggers are designated S1X, S1Y
 and S2X, S2Y; where 1(2) denote the up(down)stream
 plane, and X(Y) denote the horizontal(vertical) scintil-
 lator bar orientation (Fig. 49).

It should be noted an optimal design would generate
 an AND between the PMTs on each side of every bar
 first, and OR the resulting per-bar coincidences to form
 a pre-trigger for the plane. The compromise above was
 driven by constraints of the legacy LeCroy 4564 CA-
 MAC logic units held over from the 6 GeV era.

The SHMS detector stack includes a permanent
 Heavy Gas Cherenkov (HGC) (Sect. 3.6), but also in-

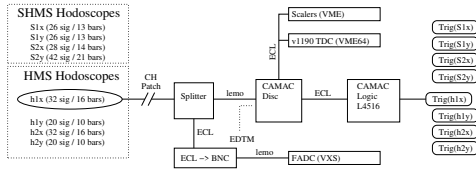


Figure 49: Block diagram for SHMS and HMS hodoscope pre-trigger formation.

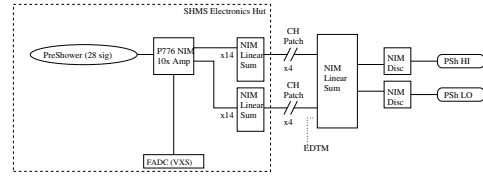


Figure 51: Block diagram for SHMS PreShower summing trigger.

1851 cludes space for a second *Noble Gas* Cherenkov (NGC) 1886
 1852 (Sect. 3.7). Each SHMS gas Cherenkov detector 1887
 1853 incorporates four PMTs, each detecting light from one of 1888
 1854 four mirrors inside their respective gas volumes. 1889
 1855 Analog signals from the PMTs are split (50:50) with one
 1856 path plugged into an FADC. The second copies from
 1857 each PMT are summed, and the summed output is dis- 1890
 1858 criminated to form a Cherenkov pre-trigger for that 1891
 1859 Cherenkov detector (HGC and NGC). The pre-triggers 1892
 1860 are also routed to scaler channels and a v1190 TDC. 1893
 1861 An optional SHMS Aerogel (Sect. 3.8) may also be 1895
 1862 installed. It employs seven PMTs on each side of its dif- 1896
 1863 fusion box. The signals from all 14 PMTs are handled 1897
 1864 analogously to the gas Cherenkov, with each analog signal 1898
 1865 being split and readout by an individual FADC channel, 1899
 1866 and second copies being summed and discriminated
 1867 to form an associated aerogel pre-trigger. The pre-trigger
 1868 is routed to a scaler and v1190 TDC as well.

1869 A block diagram for the Cherenkov pre-triggers is
 1870 presented in Figure 50.

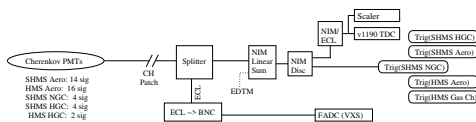


Figure 50: Block diagram for SHMS and HMS Cherenkov pre-trigger formation.

1871 The SHMS PreShower layer (Sect. 3.9) consists of
 1872 28 lead-glass blocks arranged 14 rows, with 2 blocks to
 1873 a row. Each block is coupled to a single PMT on the 1900
 1874 side facing the perimeter of the layer. Analog signals 1901
 1875 from the 28 PMTs are split and summed in 3 groups 1902
 1876 of 4 rows, and 1 group of 2 rows. Each of the 4 1903
 1877 group sums is readout by an FADC channel for cross 1904
 1878 checks. The 4 group sums are summed in turn to pro- 1905
 1879 vide a total PreShower sum which is then discriminated 1906
 1880 and provides the SHMS *PSH* pre-trigger. Provision is 1907
 1881 made to generate independent pre-triggers for both low- 1908
 1882 and high- energy depositions in the PreShower layer 1909
 1883 (*PSH.Lo* and *PSH.Hi*, respectively) (Fig. 51). 1910

1884 The aforementioned pre-triggers are then combined 1911
 1885 to form a set of triggers capable of initiating a DAQ 1912

event. These combination are often adjusted or opti-
 mized to serve the needs of particular experiments but a
 set of commonly available event triggers is outlined in
 Section 4.1.4.

4.1.3. HMS Triggers

The standard HMS detector stack [69] is the prede-
 cessor of the SHMS system and shares a nearly identi-
 cal design (Fig. 52). It consists of a pair of scintillator-
 based hodoscope planes in an X+Y configuration, a gas
 Cherenkov detector, a second pair of X+Y hodoscopes,
 and a Preshower + Shower Calorimeter. Provision is
 also made for an optional Aerogel Cherenkov to be in-
 serted into the detector stack just downstream of the
 drift chambers for supplemental particle identification
 (PID).

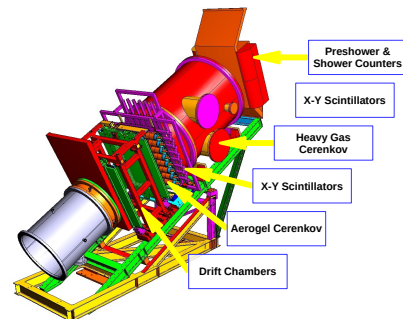


Figure 52: Typical detector layout for the HMS.

The trigger and readouts designs follow the patterns
 described in Section 4.1.2, with a modest difference as-
 sociated with the HMS Calorimeter.

Signals from the four HMS hodoscope planes, de-
 noted h1x, h1y, h2x, h2y, are split, discriminated, and
 recombined to form a *Scin* trigger following the same
 logic as the SHMS hodoscopes described previously.

The HMS gas Cherenkov detector incorporates two
 PMTs detecting light from two mirrors inside the HMS
 Cherenkov tank. Analog signals from the PMTs are
 split (50:50) with one path plugged into an FADC. The
 second copies from each PMT are summed, and the

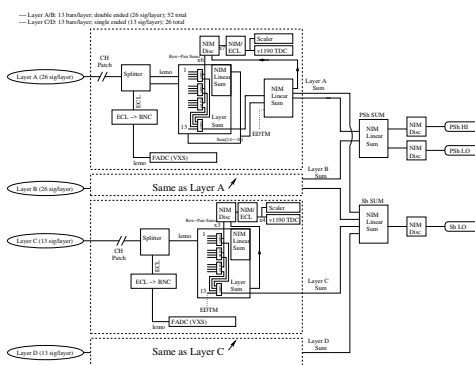
1913 summed output is discriminated to form the Cherenkov 1948
 1914 pre-trigger. That pre-trigger is also routed to a scaler 1949
 1915 and v1190 TDC. 1950

1916 The HMS Aerogel employs eight PMTs on each side 1951
 1917 of its diffusion box. The signals from all 16 PMTs are 1952
 1918 split and readout by an individual FADC channel, with 1953
 1919 the second copies being summed and discriminated to 1954
 1920 form the associated aerogel pre-trigger. The pre-trigger 1955
 1921 is routed to a scaler and v1190 TDC as well. 1956

1922 The HMS calorimeter is composed of four layers of 1957
 1923 lead glass blocks. Each layer has 13 lead-glass blocks 1958
 1924 arranged horizontally, and the layers are denoted A, B, 1959
 1925 C and D as seen by a particle passing through the de- 1960
 1926 tector stack. Layers A and B have PMTs bonded to 1961
 1927 each end of their blocks, while Layers C and D have 1962
 1928 a single PMT on one side only. Analog signals from the 1963
 1929 PMTs are split 50:50 with one copy being delivered to 1964
 1930 an FADC. The copies are formed into an analog sum for 1965
 1931 each side of each layer, denoted hA+, hA-, hB+, hB-, 1966
 1932 hC, and hD. Layer sums hA and HB are formed by sum- 1967
 1933 ming hA+ and hA-, and hB+ and hB-, respectively (hC 1968
 1934 and hD are already layer sums).

1935 One copy of each layer sum is sent to an FADC for 1969
 1936 monitoring and cross checks. A PreShower pre-trigger 1970
 1937 is formed by summing and discriminating Layers A + 1971
 1938 B, and a Shower Low pre-trigger is formed by sum- 1972
 1939 ming and discriminating Layers A+B+C+D. Copies of 1973
 1940 the PreShower and Shower sums are sent to FADCs and 1974
 1941 copies of the discriminated pre-trigger signals are sent 1975
 1942 to scalars and 1190 TDCs. 1976

1943 Figure 53 depicts a block diagram of the HMS 1977
 1944 Calorimeter pre-triggers. 1978



1979 Figure 53: Block diagram for HMS Shower and Preshower summing 1980
 1981 triggers. 1982

1945 4.1.4. Event Triggers

1946 The aforementioned pre-triggers are then combined 1995
 1947 to form a set of triggers capable of initiating a DAQ 1996

event. The ‘default’ single-arm trigger is formed by 3
 out of 4 hodoscope planes firing in coincidence. Often
 referred to as the *3 of 4* or *Scin* trigger, it provides a
 high-efficiency (> 99%) general-purpose charged particle
 trigger.

A second standard trigger is referred to as *EL_Clean*.
 It implements particle discrimination at the trigger level
 by forming a coincidence between the *Scin* pre-trigger,
 one (or more) Cherenkov pre-triggers, and (optionally)
 the pre-shower (*PSh*) and/or calorimeter total-sum
 (*ShTot*) pre-triggers.

4.2. Electronic Dead Time Measurement System (EDTM)

The DAQ and trigger system for each spectrometer
 also includes an Electronic Dead Time Measurement
 (EDTM) system. This is implemented by replicating
 a pulse from a pulse-generator circuit and feeding into
 every pre-trigger leg as close to the analog signals as
 possible. The timing of those duplicated pulses is ad-
 justed to match those generated by a real particle pass-
 ing through the detector stack. A copy of each synthetic
 EDTM trigger is counted in a deadtime free scaler and
 sent to a dedicated TDC channel in each arm. The pres-
 ence of an appropriately timed hit in that TDC channel
 tags an event as having been generated by an EDTM
 trigger.

During beam operations, this allows a direct measure-
 ment of the fraction of triggers that are lost due to some
 component of the DAQ being busy. This is known as
 the system *deadtime*. By inducing synthetic signals as
 early in the trigger electronics as possible, this system
 is sensitive to high-rate signal pile-up in the full front-
 end trigger logic chain, as well as digitization and read
 out related deadtimes implicit in the non-pipelined DAQ
 operation presently in use in Hall C.

In addition to the above function, the system has
 proved useful for pre-beam trigger verification and end
 to end checkout of the DAQ system.

- It allows rough timing on all trigger legs to be verified without beam.
- It allows coincidence timing between the SHMS and HMS arms to be roughed in and tested without beam.
- It allows the entire DAQ system to be stress tested under controlled conditions without beam.

4.3. Auxiliary Data Collection

The standard method for slow controls data logging is
 through the Experimental Physics and Industrial Control
 System (EPICS)[64]. EPICS is a system of open

1997 source software tools and applications used to pro- 2046
1998 vide control user interfaces and data logging for sys- 2047
1999 tems such as high- and low-voltage detector power sup- 2048
2000 plies, target systems, spectrometer magnets, vacuum, 2049
2001 and cryogenic systems, etc. 2050

2002 Long-term, persistent storage of EPICS based slow 2051
2003 controls data is provided through an independent archiv- 2052
2004 ing system managed by the Accelerator Division's MYA 2053
2005 archiving system. A experimentally relevant subset of 2054
2006 EPICS data (beam and target characteristics; magnet, 2055
2007 spectrometer and detector settings, etc.) are also stored 2056
2008 in the experimental data files at regular intervals when- 2057
2009 ever the DAQ is running. 2058

2010 4.4. Online Hall C Computing Environment 2059

2011 Hall C employs a dedicated stand-alone computing 2060
2012 cluster with redundant multi-core servers focused on 2061
2013 prompt online analysis, high volume local data stor- 2062
2014 age, and 1–10 Gb ethernet interconnects. There are 2063
2015 dedicated hosts for each independent DAQ system (*ex.* 2064
2016 SHMS and HMS), and auxiliary machines for polarime- 2065
2017 try, target controls, spectrometer slow controls, etc. 2066

2018 Experimental control and operational feedback is 2067
2019 provided to users in the Hall C Counting house through 2068
2020 a set of five multi-screen computer workstations and a 2069
2021 set of large wall-mounted displays for critical data. 2070

2022 All systems have direct access to the JLab centrally 2071
2023 managed Scientific Computing resources. This includes 2072
2024 multi-petabyte tape storage and online disk facilities, as 2073
2025 well as a several thousand core compute farm for simu- 2074
2026 lation and offline data analysis[68]. 2075

2027 4.5. Future Plans / Pipeline trigger 2076

2028 During the early stages of the 12 GeV Hall C upgrade 2078
2029 plan it was concluded that the risks of moving to a fully 2079
2030 pipelined DAQ system with a firmware driven trigger 2080
2031 were not justified by the needs of the initial experimen- 2081
2032 tal program. In general, those experiments did not im- 2082
2033 pose a too heavy burden on the DAQ, and the more con- 2083
2034 ventional trigger design with its well understood char- 2084
2035 acteristics was preferred. 2085

2036 However, provision was made to design and build the 2086
2037 low-level DAQ system with an upgrade path in mind. 2087
2038 To that end, a full compliment of trigger and payload 2088
2039 modules compatible with the pipelined systems being 2089
2040 implemented for Halls B and D was selected. 2090

2041 A phased transition from the NIM/CAMAC trigger 2091
2042 system to a fully pipelined approach would involve im- 2092
2043 plementing the present trigger logic within the existing 2093
2044 JLab FADC and VXS Trigger Processor (VTP) boards, 2094
2045 and a thorough validation of the firmware based trigger 2095

decisions against the well understood conventional trig-
ger. Once the firmware is fully debugged/characterized,
the DAQ could transition to pipelined mode and take ad-
vantage of significant boost in trigger accept rates into
the 10's of kHz range with minimal deadtime. At that
point the next DAQ bottleneck would likely be rate lim-
itations in the detector systems themselves (signal pile-
up in the front-end, track reconstruction limitations,
etc.)

2059 5. Software

Hall C Data is analyzed by the Hall C analysis pack-
age *hcana*. This package does full event reconstruc-
tion for the SHMS used alone or in coincidence with
other detectors. *hcana* is based on the modular Hall A
analyzer [62] ROOT [63] based C++ analysis frame-
work. This framework provides for run time user con-
figuration of histograms, ROOT tree contents, cuts, pa-
rameters and detector layout.

hcana includes C++ classes for detectors, spec-
trometers, and physics analyses. Instantiation of these
classes as objects is configured at run-time through a
ROOT script which also sets up the configuration of
analysis replay. Due to the similarity of the SHMS
and HMS spectrometers and their detector packages,
the same spectrometer and detector classes are used for both
spectrometers. For example, the drift chamber package
class is instantiated for both spectrometers with each ob-
ject configured by its specific parameters and geometry.
Additional modules such as new front end decoders, de-
tectors, or physics analysis modules can easily be added
to *hcana*. These modules can either be compiled into
the analyzer or be compiled separately and dynamically
loaded at run time.

Event analysis is segmented into 3 steps of spectrom-
eter and detector specific analysis.

1. Decoding: Detector requests from the low level decoder a list of hits sorted detector by plane and counter number. A minimal amount of processing is done to make data available for low level histograms.
2. Coarse Processing: Tracks are found in the drift chambers. Hits and clusters in the hodoscope, shower counter and other detectors are matched to the tracks to determine time-of flight. The various detectors provide information for particle identification.
3. Fine processing: Particle identification information is refined, tracks in the focal plane are traced back to the target coordinate system and particle momentum is determined.

2096 Each step of these steps is completed for all detectors
 2097 before proceeding to the next step. Some limited infor-
 2098 mation is passed between detectors at each step. For ex-
 2099 ample, timing information from the hodoscopes is used
 2100 to obtain the start time for the the drift chambers in the
 2101 decoding step and tracks obtained from the drift cham-
 2102 bers are associated with shower counter hit clusters in
 2103 the fine processing step.
 2104 After these steps single arm and coincidence physics
 2105 quantities are calculated using various physics analysis
 2106 classes that are configured at run-time.

2107 5.1. Online Monitoring

2108 After each data taking run (typically an hour or less)
 2109 is started, a subset of the data is analyzed with hcana.
 2110 An easily configurable histogram display GUI is used to
 2111 view diagnostic histograms and compare them to refer-
 2112 ence histograms. The EPICS [64] control system alarm
 2113 handler is used to monitor experiment settings and beam
 2114 conditions. This includes spectrometer magnet settings,
 2115 detector high voltages, drift chamber gas, cryogenic
 2116 systems and spectrometer vacuum.

2117 6. SHMS Performance: Operating Experience and 2118 Commissioning Results

2119 *System Performance section. Organizer: Editors –*
 2120 *with input from all authors.*

2121 Each subsection author (above) is asked to provide
 2122 suggestions, figures, and text snippets or complete sub-
 2123 sections that can be put together to create this section
 2124 of the paper. The purpose of this section is to present
 2125 the demonstrated capabilities of the SHMS – at least in
 2126 comparison to its design specifications.

2127 6.1. Acceptance

- 2128 1. vs. delta
- 2129 2. vs. theta, phi
- 2130 3. vs. $x_{targ}, y_{targ}, z_{targ}$

2131 6.2. Rates and Livetime

1. Deadtime Measurement by Electronic Pulse Gen-
erator

The computer live time efficiency of the DAQ is defined as,

$$\epsilon_{CLT} = \frac{N_{(phy+edtm),TDC} - N_{(edtm),TDC}}{N_{(phy+edtm),SCL} - N_{(edtm),SCL}} \quad (8)$$

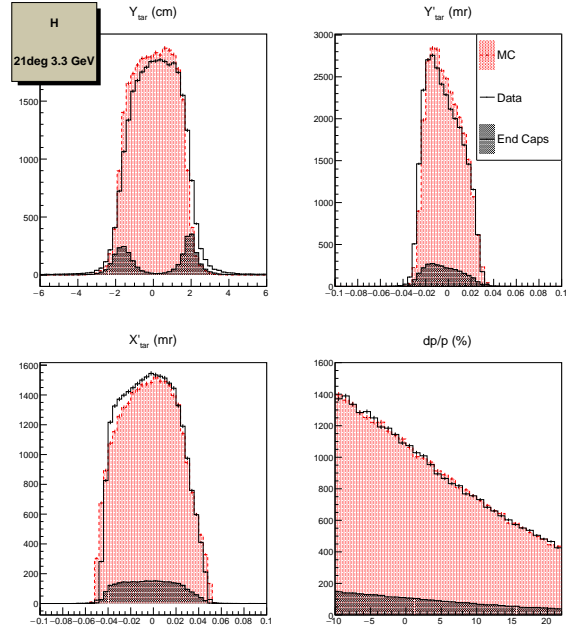


Figure 54: SHMS acceptance at 21° and $P_{central} = 3.3 \text{ GeV}/c$.

where the numerator is the total number of EDTM-subtracted TDC counts (total accepted physics triggers) and the denominator is the total number of EDTM-subtracted scaler counts (total physics pre-triggers). The EDTM introduces a bias in the computer live time calculation and must therefore be subtracted from the physics trigger. The bias comes from the fact that the EDTM is a clock and cannot be blocked by another EDTM signal, thereby having no contribution to the deadtime of the system. An additional bias arises during beam-off time periods, where only EDTM triggers are counted. To remove this bias, a beam current cut was required in the live time calculation.

The computer live time data shown in Figure 56 is plotted against the un-prescaled input trigger rates (top x-axis) and the first plane (S1X) of the SHMS Hodoscopes (bottom-axis). The data were obtained from the SHMS luminosity scans and the Kaon LT experimental data taken on Fall 2018. The Spring 2018 scans (blue squares) were taken with DAQ in buffer level 1 (unbuffered mode) and the Kaon LT data (green triangles) and Fall 2018 scans (red circles) were with DAQ in buffer level 10 (buffered mode). The advantage of buffered mode (technical definition should be described in another section) is that the DAQ is capable of accepting higher trigger rates while keeping the com-

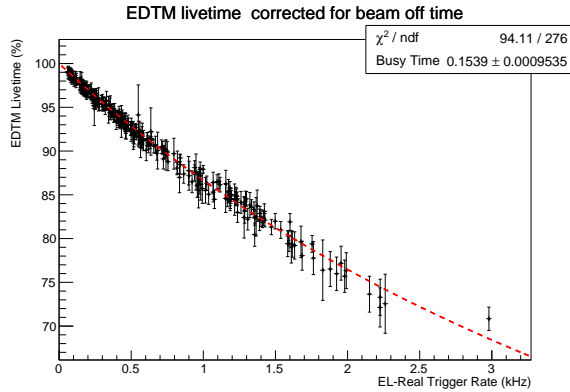


Figure 55: Total livetimes from E12-10-002 as measured by the EDMT system. Corrections have been applied for the time the beam current was below $5 \mu\text{A}$

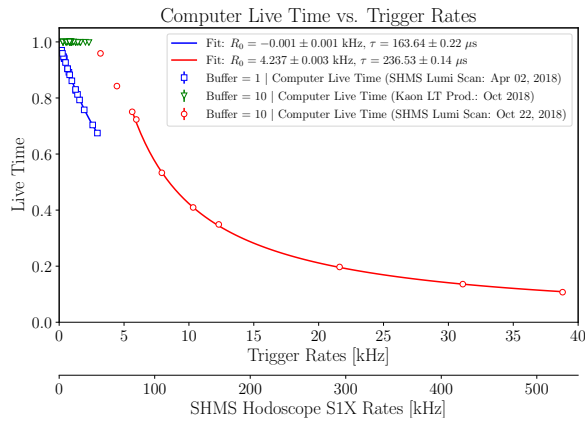


Figure 56: Computer live time vs. trigger rates (top x-axis) and SHMS hodoscope SIX plane rates (bottom x-axis) for DAQ buffer levels 1 and 10.

puter live time efficiency $\sim 100\%$. Both buffered and unbuffered modes exhibit a characteristic fall-off of the live time as a function of the trigger rate which has been modeled using the fit function,

$$f_{\text{CLT}}(R) \equiv \frac{1}{1 + (R - R_0)\tau}, \quad (9)$$

where R is the input trigger rate, R_0 describes a horizontal offset between the unbuffered and buffered modes and τ represents the averaged data readout time (deadtime) before the DAQ is ready to accept another pre-trigger. The fit function, however, is unable to describe the “flat” region where the live time is nearly 100%. From the fit parameters, the fall-off behavior of buffered mode starts at trigger rates, $R \sim 1/\tau$, which corresponds to a numerical values of ~ 4.2 kHz before a significant drop in the

live time is observed.

As of Fall 2018, the DAQ has been operated in buffered mode which has proved to be more feasible for current and future high-rate experiments at Hall C.

2. Trigger rate vs. beam current
3. Event rate vs. beam current
4. Data rate vs. beam current
5. Consistency of livetime determination

6.3. Measurement Precision

1. Momentum
2. Angle
3. Timing
4. Recoil mass spectrum
5. Missing mass from $H(e e')p$
6. Magnitude and Impact of Multiple Scattering. Removal of NGC to improve low-energy precision.

6.4. System Efficiency

(as opposed to individual detector efficiency which should go in the detector subsection above.

1. Track finding and fitting

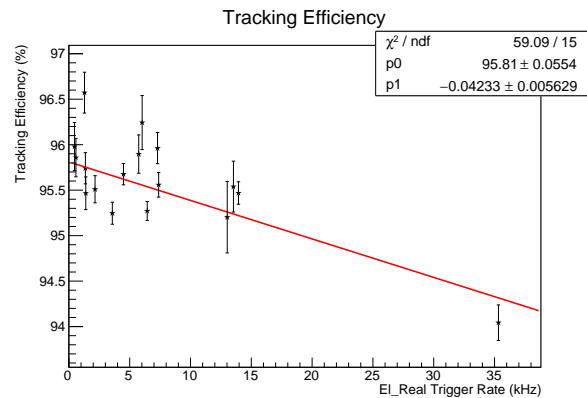


Figure 57: Tracking efficiency as a function of trigger rate. (E12-10-002)

2. Particle ID / Rejection
3. Energy Resolution and Stability
4. Background Rejection / Accidentals rate / Amount and Impact of delta-ray production

6.4.1. HGC Performance

The performance of the HGC is determined by the capacity to separate particle species on the basis of produced NPE. In particular, the HGC is a threshold Cherenkov detector and thus identifies species based on whether or not a signal greater than 1.5 NPE was generated or not. The first metrics of performance to be discussed are the detector efficiency and contamination.

Efficiency in this context refers to the ratio of events selected as a particular particle species by all detectors in the SHMS, including the HGC, over the number of events selected as that same species without any information from the HGC. This is illustrated by the equation

$$\eta_{HGC} = \frac{\pi^+ \text{ detected with HGC signal}}{\pi^+ \text{ detected without HGC signal}}, \quad (10)$$

where η_{HGC} represents the detector efficiency of the HGC and π^+ particle type is used as an example. The selection criteria includes cuts on the timing information, reconstructed β , calorimeter, aerogel and HGC information, and a single reconstructed track. Contamination refers to the number of events identified as a sub-threshold particle by the calorimeter and aerogel Cherenkov, but produced more than 1.5 NPE in the HGC. For example, if the HGC is configured for π^+/K^+ separation, the K^+ contamination is defined as the number of events identified as a K^+ by all detectors, except the HGC, which identified a π^+ .

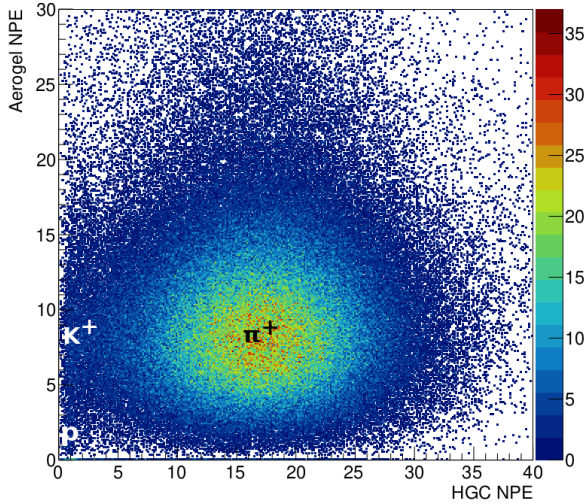


Figure 58: Demonstration of the particle identification capability of the Heavy Gas Cherenkov. Pictured is the separation between π^+ , K^+ and proton at the 8.186 GeV beam energy and 6.053 GeV/c SHMS central momentum. The refractive indexes of HGC and aerogel Cherenkov detectors are 1.00143 and 1.011, respectively.

Two runs are chosen to show HGC efficiency and contamination, one where the HGC separated between e^-/π and the other π/K . The former featured the HGC filled with CO_2 at 1 atm and a SHMS central momentum of $-3.0 \text{ GeV}/c^2$. Particle identification was established by a cut on the normalized calorimeter energy. The latter had the HGC filled with C_4F_{10} at 1 atm, giving a π momentum threshold of $2.8 \text{ GeV}/c^2$ and a K momentum threshold of $9.4 \text{ GeV}/c^2$, at a SHMS central momentum of $+5.05 \text{ GeV}/c^2$. Particle identification was performed by a cut on the aerogel Cherenkov detector and the normalized calorimeter energy. The spectrum obtained for the π/K separation is shown in Figure 58. This figure illustrates the broad distribution of NPE produced by π , fit with the red curve, which are above their momentum threshold. At the lower end of the NPE axis, there is a very large number of events producing no light, or just the SPE. These events correspond to K since they are below the momentum threshold to produce Cherenkov light. The presence of the SPE is likely due to δ -rays, or knock-on e^- , a phenomenon where K can ionize the Cherenkov media and produce e^- which produce Cherenkov radiation. The vertical blue line indicates the NPE threshold, above which events are identified as π , below which are K . The summary of the particle identification efficiency and contamination is shown in Table 5.

Lastly, measurements of the π efficiency across a variety of momentum settings can be used to verify the index of refraction of the Cherenkov media. The relationship between π efficiency and momentum is fit with the equation [21]

$$\eta_{HGC} = 1 - e^{-(p-p_o)/\Gamma}, \quad (11)$$

where η_{HGC} is the detector efficiency, p is the momentum of the π , and p_o and Γ are free parameters. Data taken in the range of 2.53 GeV/c to 5.05 GeV/c with the HGC filled with C_4F_{10} yields an index of refraction of $n = 1.001 \pm 0.002$. This is in agreement with the accepted value of $n = 1.00143$ [22].

PID Configuration	Efficiency	Contamination
e^-/π^-	95.99%	10000 : 1
π^+/K^+	98.22%	1000 : 1

Table 5: Summary of the Heavy Gas Cherenkov performance in separating between particle species. Efficiency is based on a photoelectron cut greater than 1.5.

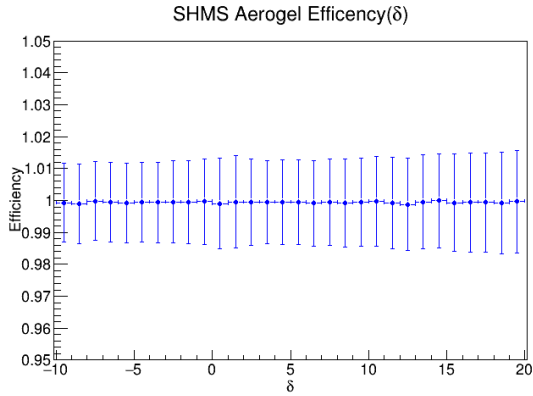


Figure 59: The efficiency of the aerogel is plotted over a range of δ . This efficiency is taken at a beam energy of 6.2 GeV for an SHMS central momentum of 3.486 GeV/c. The refractive index of the aerogel detector is 1.015.

PID Configuration	Efficiency	Contamination
K^+/p	99.94%	1000 : 1

Table 6: Aerogel performance for kaon-proton separation with efficiency based off of cut greater than 1.5 photoelectrons.

6.4.2. SHMS Aerogel Performance

The primary use of the aerogel Cherenkov detector in the SHMS is to distinguish between kaon and protons. A variety of aerogel tile refractive indices are used to reach a range of momenta. A cut greater than 1.5 photoelectron (NPE) cut is used to properly identify the particles. Figure 58 shows the particle identification of the Heavy Gas Cherenkov as well as the aerogel Cherenkov detector. This figure shows the importance of having both the Heavy Gass and the aerogel Cherenkov detectors as the kaon and proton would be indistinguishable without the aerogel.

In order for clean samples of the kaon, a high detector efficiency in the aerogel is required. The efficiency is determined by

$$\eta_{\text{aero}} = \frac{K^+ \text{ detected with aerogel signal}}{K^+ \text{ detected without aerogel signal}}, \quad (12)$$

where the detector efficiency is represented by η_{aero} . The efficiency of the aerogel detector can be seen in table 6. It is clear that the aerogel has a very high efficiency as required but this efficiency also runs over the full range of δ as seen in figure 59. This, plus the ability to change refractive indices, allows for terrific kaon identification over a wide range of kinematics.

6.4.3. Performance of SHMS calorimeter

Material on the gain stability/consistency to be added (resolution versus run number for a time period, or mip peak position versus run number).

The performance of the SHMS calorimeter under the beam conditions was tested first time during 12 GeV Hall C Key Performance Parameter Run in spring of 2017. As part of the SHMS detector package the calorimeter was commissioned in the Hall C fall run period of the same year. The first experimental data with use of the calorimeter is being collected for series of the first 12 GeV Hall C experiments: E12-10-002 (F_2 structure function at large x) [56], E12-06-107 (Search for Color Transparency) [59], E12-10-008 (EMC effect) [57], E12-10-003 (Deuteron Electro-Disintegration) [58], E12-09-017 (P_T dependence of SIDIS cross section) [60], E12-09-002 (Precise π^+/π^- ratios in SIDIS) [61] and E12-09-011 (L/T separated $p(e, e'K)$ factorization test) [42]. The early analyses of the calorimeter data demonstrate satisfactory performance of the detector in terms of resolution and PID capabilities (fig. 60).

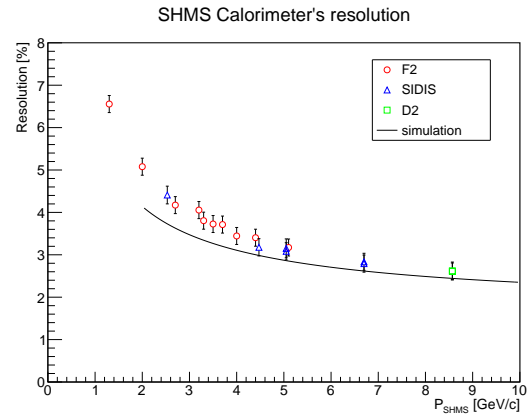


Figure 60: Resolution of the SHMS calorimeter from calibrations of runs from the Spring 18 run period. The solid line is result from the early simulations. **[This figure is not final.]**

6.5. Stability and Reproducibility

1. Trigger rate
2. Trigger efficiency
3. Kinematic quantities

7. Conclusion

Conclusion section. Author Organizer: H. Fenker

- We wanted to build it

2268 • We built it 2329

2269 • It works 2330

2270 • We're using it to do physics 2331

2271 [1] Hall-C Collaboration, JLab Internal Document - (2002). 2332

2272 [2] Physics & Instrumentation with 6-12 GeV Beams, a Thomas 2333

2273 Jefferson National Accelerator Facility report, S. Dytman, H. 2334

2274 Fenker and P. Roos, eds., June 1998. 2335

2275 [3] **References to SHMS magnet conference papers and/or publica-** 2336

2276 **tions or tech-notes.** 2337

2277 [4] I. Niculescu et al., Phys. Rev. Lett. 85 (2000) 1186; 2338

2278 [5] T. Kitagaki, et al., Phys. Rev. D 42 (1990) 1331; A. Bergier, et 2339

2279 al., Z. Phys. C 5 (1980) (265), and references therein. 2340

2280 [6] J. R. Dunning et al., Phys. Rev. 141 (1966) 1286; R. Bilger, et 2341

2281 al., Nucl. Inst. and Meth. A 457 (2001) 64; I. Lehmann, et al., 2342

2282 Nucl. Instr. and Meth. A 530 (2004) 275; A. Klimenko, et al., 2343

2283 Phys. Rev. C 73 (2006) 035212. 2344

2284 [7] The ALICE Transition Radiation Detector: Construction, oper- 2345

2285 ation, and performance, ALICE Collaboration, Nucl. Inst. and 2346

2286 Meth. A 888 (2018) 88-127; 2347

2287 [8] The G0 Experiment, D. Androic, et al., Nucl. Inst. and Meth. A 2348

2288 646 (2011) 59-86; 2349

2289 [9] The HERMES Spectrometer, K. Ackerstaff, et al., Nucl. Inst. 2350

2290 and Meth. A 417 (1998) 230-265; 2351

2291 [10] A forward magnetic spectrometer system for high-energy 2352

2292 heavy-ion experiments, K. Shigaki, et al., Nucl. Inst. and Meth. 2353

2293 A 438 (1999) 282-301; 2354

2294 [11] CLAS, B. Mecking, et al., Nucl. Inst. and Meth. A 503 (2003) 2355

2295 513-553; 2356

2296 [12] The aerogel threshold Cherenkov detector for the High Momen- 2357

2297 tum Spectrometer in Hall C at Jefferson Lab, R. Asaturyan, et 2358

2298 al., Nucl. Inst. and Meth. A 548 (2005) 364-374; 2359

2299 [13] The Aerogel Čerenkov counter for the SHMS magnetic spec- 2360

2300 trometer in Hall C at Jefferson Lab, T. Horn, et al., Nucl. Inst. 2361

2301 and Meth. A 842 (2017) 28-47; 2362

2302 [14] T. Skwarnicki, NIM A553 (2005) 339-344; M. Artuso et al., 2363

2303 NIM A558 (2006) 373-387. 2364

2304 [15] ASM Aerospace Specification Metals, 14112 Pontiatov Ave., 2365

2305 Santa Fe Springs, CA. 2366

2306 [16] Sinclair Glass, 105 N. Wabash Ave., Hartford City, IN. 2367

2307 [17] W. Li, M.Sc. thesis, University of Regina, 2012. 2368

2308 [18] Corning International, 1 Riverfront Plaza, Corning, NY. 2369

2309 [19] Hamamatsu Photonics K.K., Electron Tube Division, 314-5 2370

2310 Shimokanzo, Iwata City, Ahizuoka Pref., Japan 2371

2311 [20] Evaporated Coatings Inc., 2365 Maryland Rd., Willow Grove, 2372

2312 PA. 2373

2313 [21] E.J Brash et al, NIM A487 (2002) 346-352 2374

2314 [22] Ruggero Turra, CERN, (2009). 2375

2315 [23] Vijay Kumar, *Updated SHMS HGC Calibration Code*, JLab 2376

2316 Hall C Document Database 1098-v1 (27 Oct 2020) 2377

2317 [24] Rayotek Scientific (<https://rayotek.com/>). 2378

2318 [25] Detector Technologies Group (CERN) ([https://ep-dep-dt.](https://ep-dep-dt.web.cern.ch/) 2379

2319 [web.cern.ch/](https://ep-dep-dt.web.cern.ch/)). 2380

2320 [26] ET Enterprises (<http://et-enterprises.com/>). 2381

2321 [27] T. Horn, *SHMS Shielding Design*, JLab Hall C Document 2382

2322 Database 392-v1 (19 Nov 2008); *Final SHMS Shielding Design*, 2383

2323 JLab Hall C Document Database 595-v1 (24 Sept 2009) 2384

2324 [28] P. J. Griffin *et al.*, *The role of thermal and fission neutrons in* 2385

2325 *reactor neutron-induced upsets in commercial SRAMs*, IEEE 2386

2326 NS Vol. 44, No. 6, Dec. 1997. 2387

2327 [29] C. I. Underwood, *The Single-Event-Effect Behaviour of* 2388

2328 *Commercial-Off-The-Shelf Memory Devices - A Decade in the* 2389

Low-Earth orbit, IEEE Transactions on Nuclear Science Vol. 45, No. 3, June 1998.

[30] W. R. Leo, *Techniques for Nuclear and Particle Physics Experi-* 2390

ments, second edition, Springer Verlag Berlin, Heidelberg 1987, 2391

1994 2392

[31] J. F. Briesmeister (ed.), MCNP - A General Monte Carlo N- 2393

particle Transport Code Version A, LA-12625-M, Los Alamos 2394

National Laboratory, Los Alamos, New Mexico (1993). 2395

[32] S. Wood, private communication (2008). 2396

[33] M. Jones *et al.*, private communication (2008). 2397

[34] Birenbaum *et al.*, Phys. Rev. **C51**, (1995) 3496 2398

[35] D. Marsh , *Particle Practice Concrete Products* **Vol. 117**, no. 2 2399

(2014) 40. 2400

[36] T. Horn, et al., The Aerogel Čerenkov detector for the SHMS 2401

magnetic spectrometer in Hall C at Jefferson Lab, Nucl. Instrum. 2402

Meth. A842 (2017) 28–47. [arXiv:1607.05264](https://arxiv.org/abs/1607.05264), [doi:10.1016/j.nima.2016.10.039](https://doi.org/10.1016/j.nima.2016.10.039). 2403

[37] Gore, W. L. & Associates INC., "", <http://www.gore.com>. 2404

[38] Millipore Corporation, 80 Ashly Road, Bedford, MA 01730, "", 2405

<http://www.millipore.com/>. 2406

[39] I. Adachi, et al., Study of highly transparent silica aerogel as 2407

a RICH radiator, Nucl. Instrum. Meth. A553 (2005) 146–151. 2408

[doi:10.1016/j.nima.2005.08.022](https://doi.org/10.1016/j.nima.2005.08.022). 2409

[40] E. Aschenauer, et al., Optical characterization of n = 1.03 2410

silica aerogel used as radiator in the RICH of HERMES, 2411

Nucl. Instrum. Meth. A440 (2000) 338–347. [doi:10.1016/S0168-9002\(99\)00923-7](https://doi.org/10.1016/S0168-9002(99)00923-7). 2412

[41] Horn T., Huber G.M., and others, "scaling study of the l-t sepa- 2413

rated pion electroproduction cross section at 11 gev", approved 2414

Jefferson Lab 12 GeV Experiment (2007). 2415

[42] T. Horn, G. M. Huber, P. Markowitz, et al., Spokespersons, 2416

Studies of the L-T Separated Kaon Electroproduction Cross 2417

Section from 5-11 GeV. JLab proposal E12-09-011. . 2418

[43] Bosted P., Ent R., Kinney E., Mkrtychyan, H., and others, "Mea- 2419

surement of the Ratio $r = \sigma_l/\sigma_t$ in Semi-Inclusive Deep- 2420

Inelastic Regimes", approved Jefferson Lab 12 GeV Experiment 2421

(2006). 2422

[44] R. Asaturyan, et al., The aerogel threshold Cherenkov detector 2423

for the high momentum spectrometer in Hall C at Jefferson Lab, 2424

Nucl. Instrum. Meth. A548 (2005) 364–374. [arXiv:physics/0411147](https://arxiv.org/abs/physics/0411147), [doi:10.1016/j.nima.2005.04.058](https://doi.org/10.1016/j.nima.2005.04.058). 2425

[45] H. Mkrtychyan *et al.*, Nucl. Instrum. Meth. A **719** (2013) 85-100. 2426

[46] H. Avakian *et al.*, Nucl. Instrum. Meth. A **378** (1996) 155-161. 2427

[47] H. Avakian *et al.*, Nucl. Instrum. Meth. A **417** (1998) 69-78. 2428

[48] J. Alcorn *et al.*, Nucl. Instrum. Meth. A **522** (2004) 294. 2429

[49] Lytkarino factory of optical glasses, 140061, Lytkarino, 2430

Moskow region, Russia. 2431

[50] T. Amatuni, G. Kazaryan, H. Mkrtychyan, V. Tadevosyan and W. 2432

Vulcan, Nucl. Instr. Meth. A **374**, 39-47 (1996). 2433

[51] C. Zorn, private communication. 2434

[52] S. Agostinelli *et al.*, GEANT4—a simulation toolkit. Nucl. Instrum. 2435

Meth. A **506** (2003) 250-303; J. Allison *et al.*, IEEE 2436

Transactions on Nuclear Science **53**, No.1, (2006) 270-278. 2437

[53] John Apostolakis *et al.*, Progress in hadronic physics model- 2438

ing in GEANT4. XIII Int. Conf. on Calorimetry in High Energy 2439

Physics. (CALO2008); J. of Phys. Conf. Series **160** (2009) 2440

012073; J. Apostolakis *et al.*, Hadronic Shower Shape Studies 2441

in GEANT4, CERN-LCGAPP-2007-02. 2442

[54] M. Born, E. Wolf. Principles of Optics. Pergamon Press, 1965. 2443

[55] Ts. Amatuni, On the calibration of segmented full absorption 2444

calorimeters. Unpublished. 2445

[56] Precision measurements of the F_2 structure function at large x 2446

in the resonance region and beyond, JLab Proposal E12-10-002, 2447

S. Malace, M. Christy, C. Keppel, M. Niculeclu spokespersons. 2448

[57] Detailed studies of the nuclear dependence of F_2 in light nuclei, 2449

2394 Jlab Proposal E12-10-008, D. Gaskell, J. Arrington, A. Daniel, 2449
2395 N. Fomin spokespersons.

2396 [58] Deuteron Electro-Disintegration at Very High Missing Mo-
2397 mentum, JLab Proposal E12-10-108, W. Boeglin, M. Jones
2398 spokespersons.

2399 [59] D. Dutta, R. Ent., et al. Spokespersons, "The Search for Color
2400 Transparency at 12 GeV", approved Jefferson Lab 12 GeV Ex-
2401 periment (2006).

2402 [60] R. Ent, P. Bosted, E. Kenney, H. Mktrchyan spokesper-
2403 sons, "Transverse Momentum Dependence of Semi-Inclusive
2404 Pion Production", approved Jefferson Lab 12 GeV Experiment
2405 (2009).

2406 [61] Precise Measurement of π^+/π^- Ratios in Semi-inclusive Deep
2407 Inelastic Scattering Part I: Charge Symmetry violating Quark
2408 Distributions, JLab Proposal E12-09-002, K. Hafidi, D. Dutta,
2409 D. Gaskell spokespersons.

2410 [62] *Hall A Analyzer*, <https://hallaweb.jlab.org/podd/>.

2411 [63] Rene Brun and Fons Rademakers, *ROOT - An Object Oriented*
2412 *Data Analysis Framework*, Proceedings AIHENP'96 Workshop,
2413 Lausanne, Sep. 1996, Nucl. Instrum. Meth. A **389** (1997) 81-86.
2414 See also <http://root.cern.ch/>.

2415 [64] Experimental Physics and Industrial Control System (EPICS),
2416 <https://epics-controls.org/>.

2417 [65] CEBAF Online Data Acquisition System (CODA), [https://](https://coda.jlab.org/)
2418 coda.jlab.org/.

2419 [66] Jefferson Lab F250 Flash ADC module, [https://coda.jlab.](https://coda.jlab.org/)
2420 [org/](https://coda.jlab.org/).

2421 [67] CAEN v1190 Time to Digital Converter, [https://www.caen.](https://www.caen.it/products/v1190a-2esst/)
2422 [it/products/v1190a-2esst/](https://www.caen.it/products/v1190a-2esst/).

2423 [68] Jefferson Lab Scientific Computing, [https://scicomp.](https://scicomp.jlab.org/)
2424 [jlab.org](https://scicomp.jlab.org/).

2425 [69] FIXME: Hall C HMS reference?.

2426 [70] V. Tvaskis, M. Christy, *et al.*, Phys. Rev. Lett. **98**, 142301 (2007)
2427 doi:10.1103/PhysRevLett.98.142301 [arXiv:nucl-ex/0611023
2428 [nucl-ex]].

2429 [71] J. Volmer *et al.* [Jefferson Lab F(pi)], Phys. Rev. Lett. **86**, 1713-
2430 1716 (2001) doi:10.1103/PhysRevLett.86.1713 [arXiv:nucl-
2431 ex/0010009 [nucl-ex]].

2432 [72] T. Horn *et al.* [Jefferson Lab F(pi)-2], Phys. Rev. Lett.
2433 **97**, 192001 (2006) doi:10.1103/PhysRevLett.97.192001
2434 [arXiv:nucl-ex/0607005 [nucl-ex]].

2435 [73] T. Navasardyan, *et al.* Phys. Rev. Lett. **98**, 022001 (2007)
2436 doi:10.1103/PhysRevLett.98.022001 [arXiv:hep-ph/0608214
2437 [hep-ph]].

2438 [74] D. Abbott, *et al.*, Phys. Rev. Lett. **80**, 5072-5076 (1998)
2439 doi:10.1103/PhysRevLett.80.5072.

2440 [75] K. Garrow, *et al.*, Phys. Rev. C **66**, 044613 (2002)
2441 doi:10.1103/PhysRevC.66.044613 [arXiv:hep-ex/0109027
2442 [hep-ex]].

2443 [76] N. Fomin, *et al.*, Phys. Rev. Lett. **105**, 212502 (2010)
2444 doi:10.1103/PhysRevLett.105.212502 [arXiv:1008.2713 [nucl-
2445 ex]].

2446 [77] N. Fomin, *et al.*, Phys. Rev. Lett. **108**, 092502 (2012)
2447 doi:10.1103/PhysRevLett.108.092502 [arXiv:1107.3583 [nucl-
2448 ex]].

2450 *Notes for All Authors.*

2451
2452 **Nuclear Instruments and Methods Format:** NIM-
2453 A is a two-column journal, but they require that papers
2454 be submitted in their single-column preprint style, with
2455 line numbers.

2456 At submission time, Elsevier will want the image files
2457 and references to be named sequentially. Elsevier wants
2458 a lot of stuff done their way. I'll take care of that. I just
2459 ask that you send me the bare .tex of your subsection,
2460 along with pdf image files, so that it will compile when
2461 it gets pulled-in by the \input statement in my top-level
2462 shmsNIM.tex file.

2463 **AGAIN:** Please do not waste time by creating your
2464 own stand-alone .tex document. The L^AT_EX styles,
2465 macros, etc. that are used **must be those provided by**
2466 **the publisher.** To check your .tex, put it in the skeleton
2467 file that I provided to you – the one that resides inside
2468 the directory that I created for your **subsection.** Then,
2469 from within the nimtex directory, run 'make' on the file
2470 shmsNIM.tex. This will compile all of the .tex files
2471 for the whole article, including your own file, and it
2472 will allow you to verify that the .tex you have written
2473 is compatible with the overall document and with the
2474 publisher's stylesheet.

2475 Normally you would only modify files that are
2476 within your subdirectory. The one exception is the file
2477 bib_items.tex – you can add entries to that file if you
2478 surround what you add with a pair of comment lines
2479 giving your name and the date you added the content.
2480 Send author/affiliation information to me and I will add
2481 it to the front matter.

2482 I (hcf) have included references to several archival
2483 NIM articles [7, 8, 9, 10] to see how other authors have
2484 documented their detector systems. Some of them de-
2485 scribe hardware at Jefferson Lab [11, 12].

2486 One can see in Fig. 61, below, how to include a
2487 pdf image file for use as a single-column-width figure
2488 within this document. Fig. 73 shows the same image
2489 included as a full-page-width figure. Also included is
2490 an example of making a table. See Table 7.

2491 **File Organization:** Under the top-level directory
2492 *nimtex* I have created a subdirectory for each section or
2493 subsection of the paper. In each of those you'll find a
2494 .tex file ready for authors to begin writing. To keep us
2495 from clobbering each other by accidentally duplicating
2496 a file name, I suggest that you put your .pdf graphic
2497 files (yes: please supply **pdf** files for all graphics) and
2498 any other content files inside the subdirectory contain-
2499 ing your .tex file. Since the *make* will be run from
2500 the top-level directory, remember to reference the sub-
2501 directory path to the graphic (or other) file when you

2502 \include it from the .tex file. Please examine THIS file
2503 ("Instructions_For_Authors.tex") to see how the
2504 figures herein are referenced.

Sending New Material: When you want to submit
new or revised material for inclusion in the overall NIM
article, all you have to do is email the .tex and .pdf
files in your subsection directory to Roger Carlini (car-
lini@jlab.org). Alternatively, you may create a tarball
or a compressed archive file of your subsection direc-
tory and email that to me. It's your choice. Send me
your bib_items.tex file if you added references to it.

Update 31-Jul-2018: Immediately below, I have in-
serted a few drawings and photographs from my own
collection. Feel free to include them in your section if
they are useful. I will remove this entire preamble, in-
cluding unused images, when the paper nears comple-
tion.

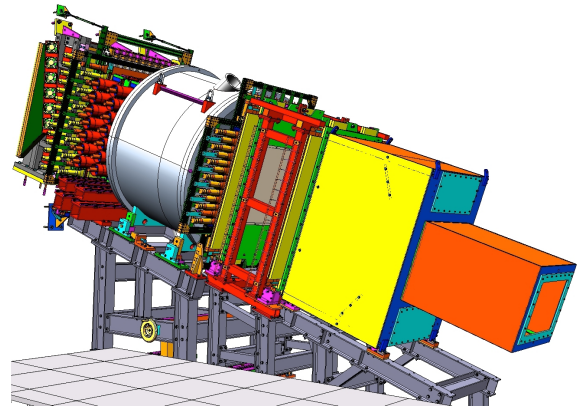


Figure 61: CAD Rendering of SHMS Detector Stack



Figure 62: Photo of the SHMS Detectors in the Shield House

Table 7: An old table of power supply settings used as an example of creating a table.

Detector Element	Heavily Ionizing Tracks		Minimum Ionizing Tracks	
	Left Half	Right Half	Left Half	Right Half
HVPS-C	4550	4350	4950	4750
HVPS-G	3050	2850	3450	3250
Window	0	0	0	0
Cathode	4532	4329	4931	4729
GEM-1i	2869	2656	3242	3026
GEM-1o	2579	2374	2915	2705
GEM-2i	2087	1918	2359	2185
GEM-2o	1798	1642	2031	1871
GEM-3i	1143	1040	1292	1185
GEM-3o	845	764	955	871
Padboard	0	0	0	0

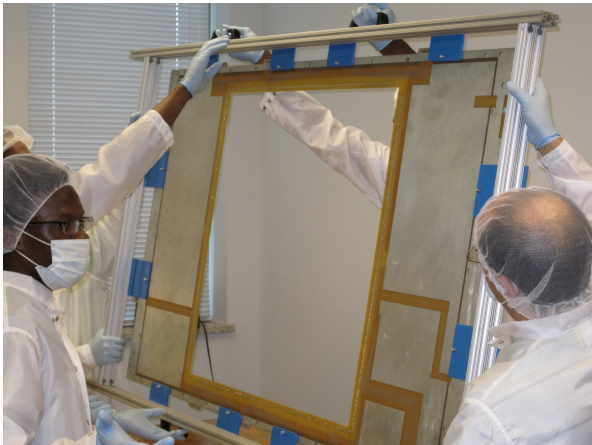


Figure 63: One of the SHMS Drift Chamber Cathode Planes being handled during construction

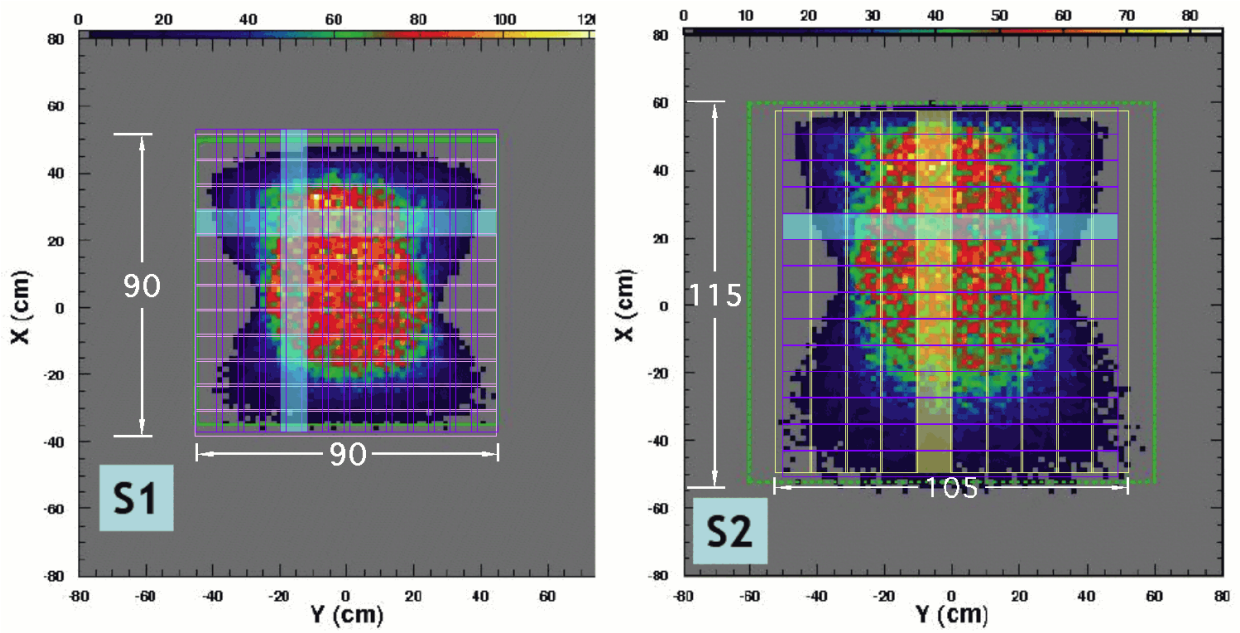


Figure 64: Monte Carlo projection of the particle distribution at two locations in the SHMS detector stack. Studies like this one were used to determine the required sensitive areas of each detector.

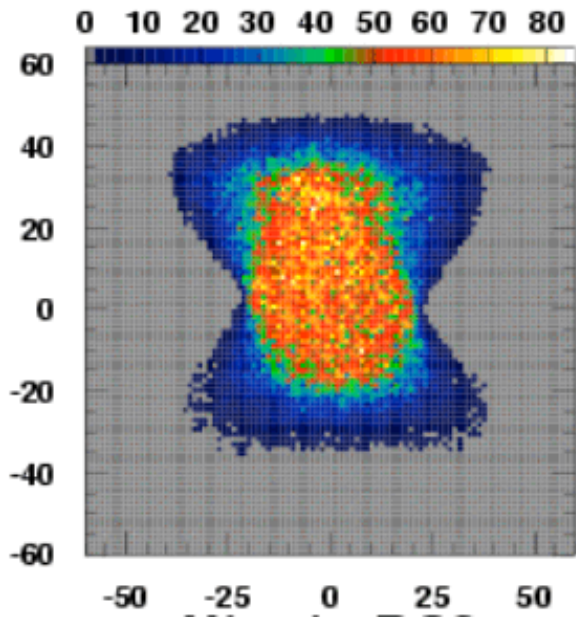


Figure 65: Monte Carlo projection of the particle distribution at the second Drift Chamber. Studies like this one were used to determine the required sensitive areas of each detector.



Figure 66: Photo showing a cross section of the Shield House Wall highlighting the layers of custom materials used.

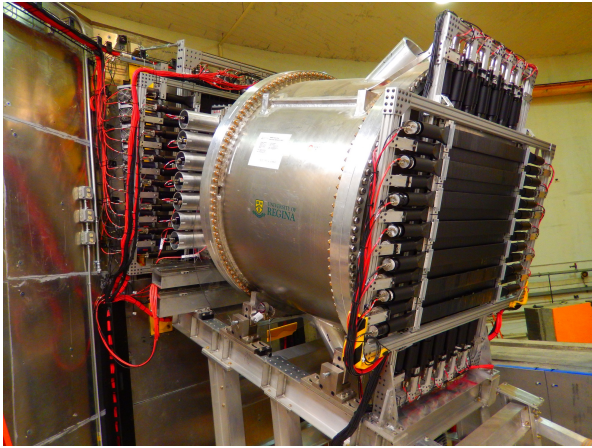


Figure 67: Photo of the SHMS Detectors starting with S1XY

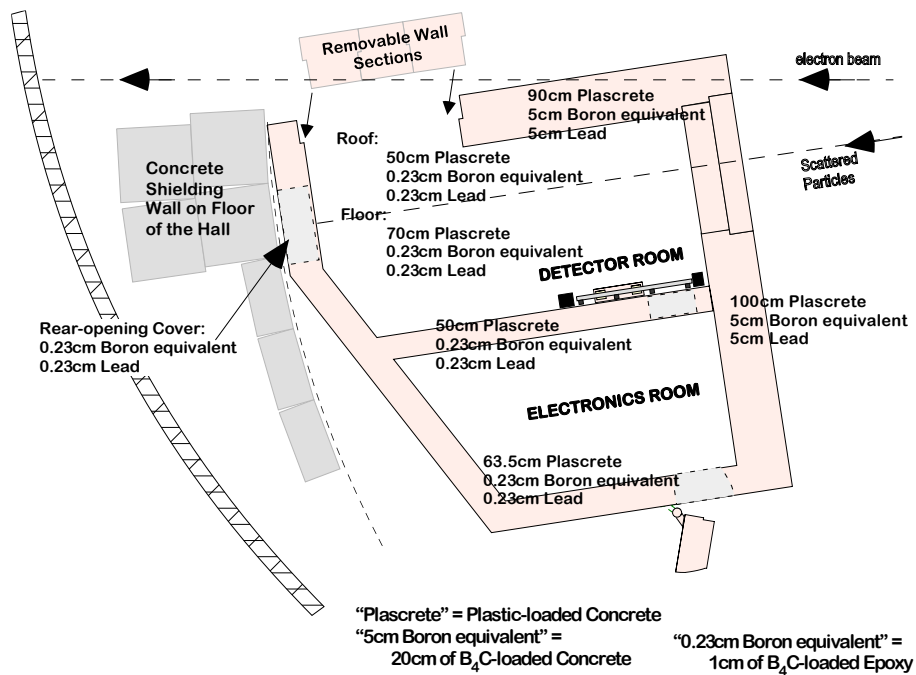


Figure 68: Shielding Arrangement for the SHMS

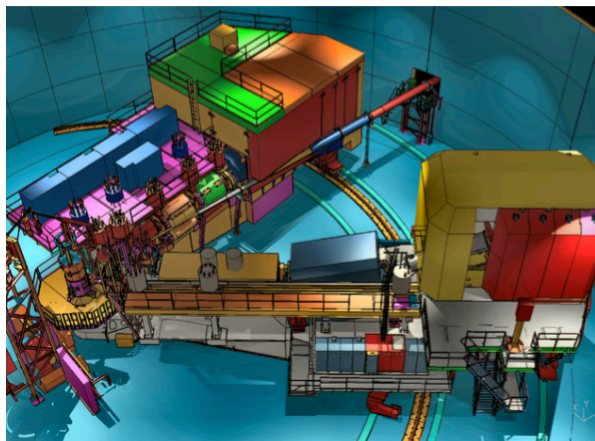


Figure 69: CAD Rendering of the SHMS and the HMS in Hall C

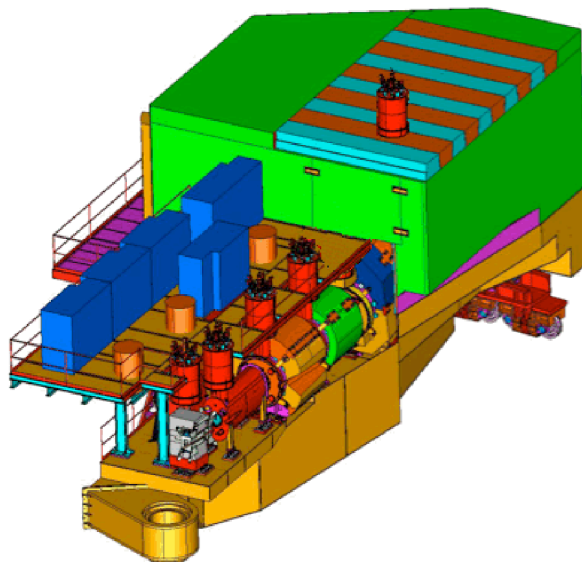


Figure 70: CAD Rendering of the SHMS

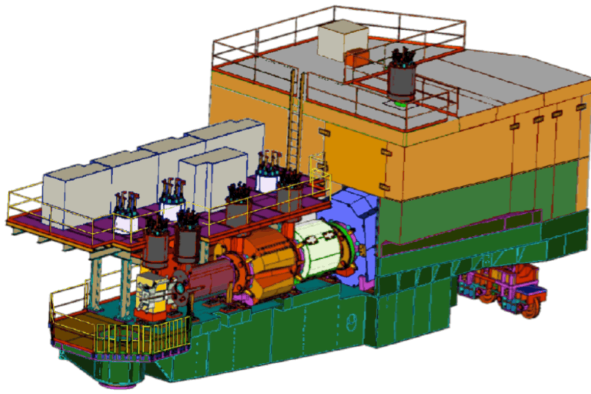


Figure 71: CAD Rendering of the SHMS in colors approximating those actually used.

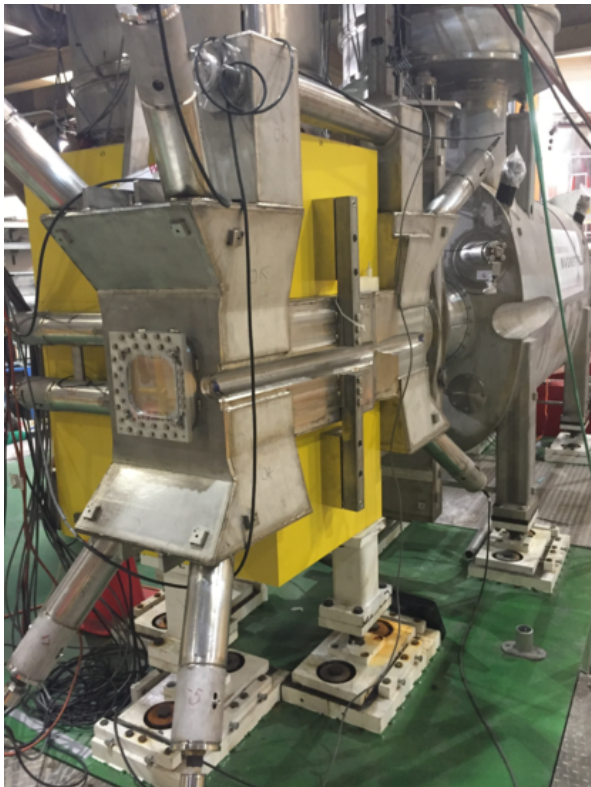


Figure 72: The Horizontal-Bend Magnet, which acts as a septum to bend scattered particles 3° away from the electron beam. The square flange on the front of the magnet surrounds the entrance vacuum window, while the slot along the near side allows the beamline vacuum pipe to come within 5.5° of the magnet axis.

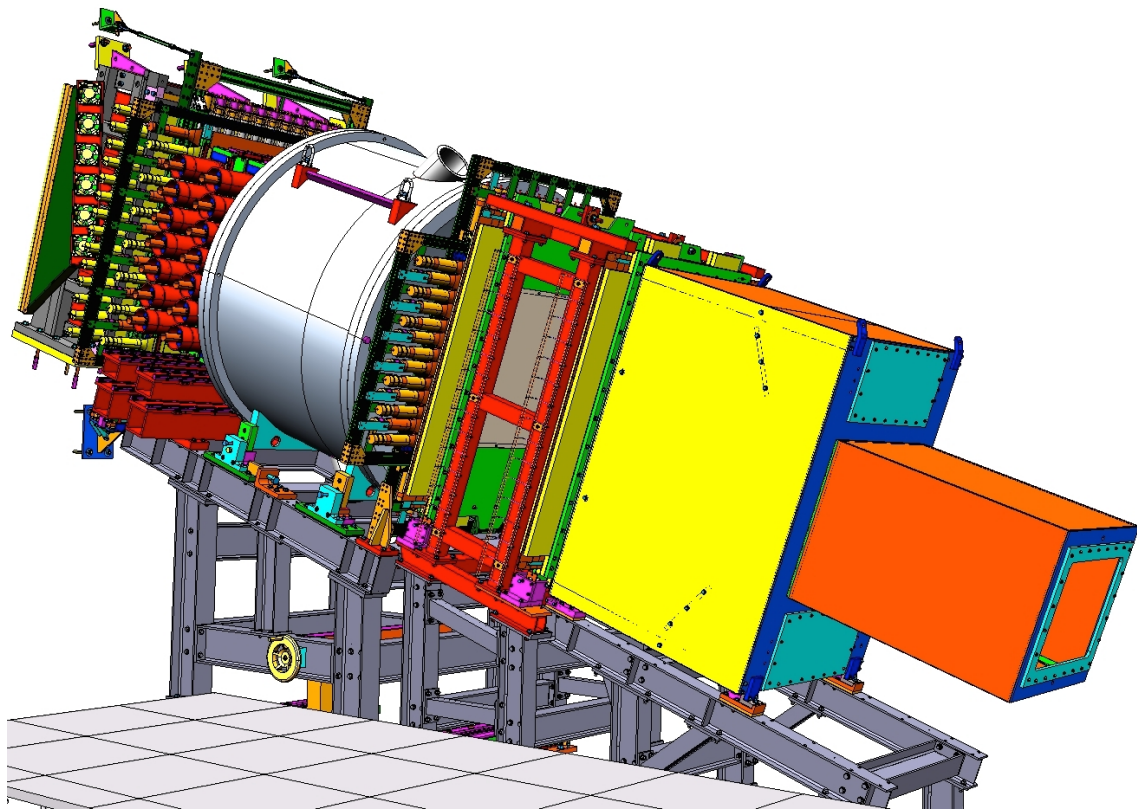


Figure 73: CAD Rendering of SHMS Detector Stack